NTNU
Norwegian University of
Science and Technology

Antideuterons as Signature for Dark Matter

Lars Andreas Dal

Physics
Submission date: May 2011
Supervisor: Michael Kachelriess, IFY

Norwegian University of Science and Technology
Department of Physics

Norwegian University of
Science and Technology

Faculty of Natural Sciences
and Technology

Department of Physics

Master's thesis

Antideuterons as Signature for Dark Matter

Author:
Lars Andreas Dal

Supervisor:
Michael Kachelrieß

Trondheim, May 15, 2011

Front page image credit:
X-ray: NASA/CXC/CfA/ M.Markevitch et al.;
Lensing Map: NASA/STScI; ESO WFI; Magellan/U.Arizona/ D.Clowe et al.
Optical: NASA/STScI; Magellan/U.Arizona/D.Clowe et al.

Problem description

The nature of dark matter (DM) is one of the largest unresolved problems in physics today. According to cosmological studies, more than 80% of the matter content of the Universe is of an invisible, unknown substance, and hypothetical Weakly Interacting Massive Particles (WIMPs) are pointed out as possible dark matter candidates. In this project, the cosmic ray antideuteron flux from annihilations of such particles will be examined.

The so-called coalescence model is commonly used to describe the production mechanism of antideuterons. This model can be implemented directly within a Monte Carlo simulation, or approximations can be made, allowing the coalescence model to be applied to the produced nucleon energy spectra after the simulations are done. The latter option is the one commonly used today, and was used in a previous calculation of antideuteron spectra from DM annihilations in an article by Bräuninger et. al. The results from this article show a peak in the antideuteron spectrum from annihilations into quarks that is orders of magnitude higher than the peak from annihilations into gauge bosons. There is no obvious reason for this large difference, and the primary goal of this project is to investigate if this difference is related to the approximations which were made in the energy spectrum application of the coalescence model.

The antideuteron spectra from different annihilation channels will in this project be calculated and compared between the two implementations of the coalescence model. The propagation of antideuterons in the Galaxy will then be examined, in order to find the corresponding antideuteron fluxes near Earth.

Abstract

In this thesis, we examine the antideuteron spectra from annihilations of dark matter in the form of Weakly Interacting Massive Particles (WIMPs). The so-called coalescence model is commonly used to describe the production of antideuterons. This model can be applied directly within a Monte Carlo simulation, but traditionally, approximations have been made that allow the model to be applied to the produced nucleon energy spectra after the simulation is done. The traditional approach is based on the assumption that the nucleons produced have isotropically distributed momenta, and is still commonly used today.

We find that the assumption of isotropy does not hold; the final state particles from WIMP annihilations are confined in jets, something which increases the antideuteron yield. This effect is missed by the traditional approach, and using the direct implementation of the coalescence model leads to an order of magnitude enhancement of the antideuteron yield. Furthermore, we find that incorrect treatment of input gauge bosons as on-shell particles in Monte Carlo generators lead to underestimates of the antideuteron flux from WIMP annihilations into gauge bosons. This effect is particularly important when using the traditional application of the coalescence model.

We also consider the contributions to the antideuteron spectrum from higher order annihilation processes, and find that for the lightest MSSM neutralino as WIMP candidate, these contributions are likely to become important for neutralino masses in the TeV range.

Acknowledgments

The author would like to thank his supervisor, Michael Kachelrieß, for invaluable help and guidance throughout the work on this project. The author would also like to thank his family for all the moral support during this time.

Contents

Introduction

In this thesis, we examine the antideuteron spectrum from annihilations of hypothetical Weakly Interacting Massive Particles (WIMPs) within our galaxy.

The main goal of this thesis is to investigate the large difference in magnitude between the antideuteron spectra from WIMP annihilations into quarks and gauge bosons found by Bräuninger et. al in [14]. The so-called coalescence model is commonly used to handle the production of antideuterons, and we will investigate if the difference in magnitude is related to a commonly used approximation of this model which assumes isotropically distributed nucleon momenta.

The thesis is divided into three chapters. In the first chapter, we present some of the evidence for the existence of dark matter, as well as some of the proposed dark matter candidates. We then discuss some of the means of detecting WIMP dark matter, as well as the current status of the field. In the second chapter, we discuss the practical and theoretical details related to the work behind the thesis. We then present and discuss the results from our calculations. The third chapter is dedicated to summary and conclusions. We also include an appendix, in which we list and describe some equations from special relativity which are needed in this thesis.

We note that we will be using natural units,

$$c = \hbar = k_B = 1,$$

and these constants will generally be left out from our equations.

Chapter I

General introduction to dark matter

1 Dark matter in galaxies

1.1 Rotation curves

One of the most important pieces of evidence for dark matter is found by studying the so-called rotation curves of (spiral) galaxies. The rotation curve can either be defined as the orbital speed $v(r)$ at a distance r from the galactic center, or as the corresponding angular speed $\Omega(r) = v(r)/r$. Knowing the rotation curve of a galaxy, we can calculate the corresponding mass distribution $M(r)$, and compare it to the distribution of observed matter.

From observations, we know that the visible matter in spiral galaxies follow roughly circular orbits. We will use this in deriving the relation between the rotation curve and the mass distribution of a galaxy. For an object at distance r from the galactic center, the radial acceleration, a_r, is given by Newton's law of gravity,

$$a_r(r) = \frac{GM(r)}{r^2}. \tag{1.1}$$

$M(r)$ is here the mass of the matter contained within the sphere of radius r, and G is the gravitational constant. For circular orbits, the relation between orbital speed and radial acceleration is given by

$$a_r(r) = \frac{v^2(r)}{r}. \tag{1.2}$$

Combining these equations and solving for $M(r)$, we obtain the galactic mass distribution,

$$M(r) = \frac{v^2(r)r}{G}, \tag{1.3}$$

or solving for the rotation curve:

$$v(r) = \sqrt{\frac{GM(r)}{r}}. \tag{1.4}$$

We can make an estimate for expected rotation curve of a galaxy by considering typical galactic luminosity distributions. For a spiral galaxy, the luminosity generally falls off exponentially with the distance from the galactic center [36]:

$$L(r) = L(0)e^{-r/D}, \tag{1.5}$$

where $L(0)$ and D are parameters which need to be fitted to the individual galaxies. Typically, $D \sim 5\,\mathrm{kpc}$. Let us now assume that the mass distribution of the galaxies roughly follow the luminosity, i.e. $M(r) \propto \int_0^r L(r')dr'$. Since $L(r)$ decreases exponentially with increasing r, we would correspondingly expect $M(r)$ to become roughly constant for large r. Inserting this in (1.4), this gives us an expected rotation curve

$$v(r) \propto \frac{1}{\sqrt{r}} \tag{1.6}$$

for large r.

The actual rotation curves can be found by studying the Doppler shift of spectral lines from gas and stars at various distances from the center of the subject galaxy. Studies have been conducted on a large number of spiral galaxies, and the general result does not agree with the above expectation. Instead of falling off as $r^{-1/2}$, the orbital speeds in the outer regions are typically roughly constant with increasing r. The galaxy NGC6503 is a perfect example of this behaviour, as can be seen in figure 1.1.

Keeping in mind equation (1.4) and (1.5), it appears that the total mass distribution in spiral galaxies must be falling off much more slowly than the distribution of gas and luminous matter. In other words: There must be a significant amount of unseen matter - dark matter. As a numerical example, consider the galaxy NGC3198. From the rotation curve, the mass-to-light ratio, $\Upsilon \equiv M/L$, of this galaxy is found to be $\Upsilon > 30h\Upsilon_\odot$, where $h \approx 0.7$, and $\Upsilon_\odot$ is the mass-to-light ratio of the Sun [31]. Using the mass-to-light ratio of the Solar neighbourhood, $\Upsilon \approx 5\Upsilon_\odot$, as an estimate for the mass-to-light ratio of the luminous matter, we see that more than roughly 80% of the mass of NGC3198 appears to be contributed by dark matter.

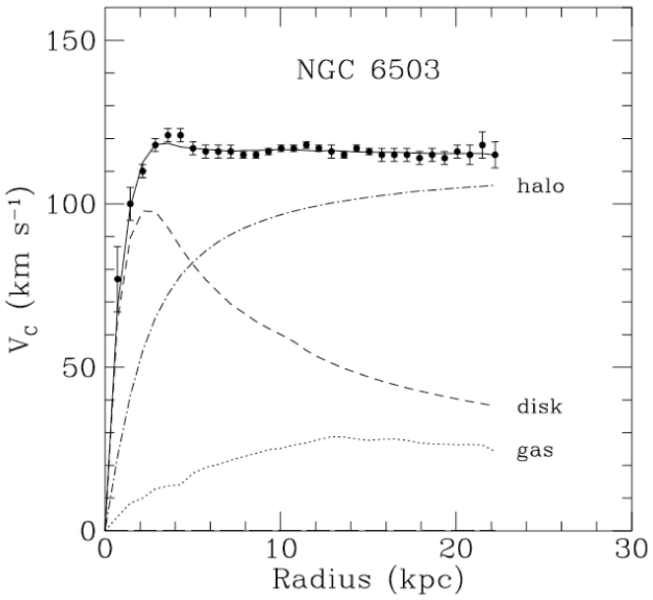

Figure 1.1: Rotation curve of the spiral galaxy NGC6503. The data points show the observed rotation curve, while the dashed and dotted lines show the contributions from the disk and intragalactic gas, respectively. The dot-dashed line shows the contribution from some other source (dark matter halo) required for the total orbital speed (solid line) to fit the observational data. Figure borrowed from [31].

1.2 Density profiles

The main focus of this thesis is to study cosmic rays from dark matter annihilations in our galaxy. In order to perform simulations on this, it is essential to have a model of how the dark matter is distributed in the Galaxy. Theoretical models show that having all the dark matter located in the disk would make it unstable, and that the disk would eventually be gathered into a bar [36]. It is therefore more likely that the dark matter has a more stable spherically symmetric distribution. A wide range of proposed dark matter density profiles exist, and we will examine some of them. We will first make a simple model from the observed galaxy rotation curves, and afterwards discuss a couple of the commonly used profiles.

1.2.1 A simple model

Using the observed constant orbital speeds, and assuming a spherically symmetric mass density $\rho(r, \theta, \phi) = \rho(r)$, we can derive a simple model that describes the dark matter density in the outer regions of the Galaxy. The mass enclosed by a sphere of

radius R is given by

$$M(r) = \int_0^r dr' \int_0^\pi d\theta \int_0^{2\pi} d\phi \, \rho(r') \, r'^2 \sin(\theta) = 4\pi \int_0^r dr \rho(r') r'^2. \tag{1.7}$$

Inserting the relation between the mass distribution and the rotation curve, as given by equation (1.3), and using a constant orbital speed, v, we obtain

$$\frac{v^2 r}{G} = 4\pi \int_0^r dr' \rho(r') r'^2. \tag{1.8}$$

Taking the derivative with respect to r on both sides gives

$$\frac{v^2}{G} = 4\pi \rho(r) r^2. \tag{1.9}$$

Solving with respect to $\rho(r)$, we then obtain our simple density profile,

$$\rho(r) = \frac{v^2}{4\pi G r^2}. \tag{1.10}$$

As we can see, the mass density has to fall off as $\propto r^{-2}$ in order to describe the observed Galactic rotation curves in the outer regions. This is far slower than the exponential falloff we assumed for the luminous matter.

Equation (1.10) is actually just a special case of the so-called singular isothermal sphere (SIS) profile,

$$\rho(r) = \frac{\sigma_v^2}{2\pi G r^2}, \tag{1.11}$$

which can be derived from a self-gravitating isothermal sphere in hydrostatic equilibrium. σ_v is here the velocity dispersion, which is related to the orbital speed in circular orbits by $\sigma_v = v/\sqrt{2}$ [49].

This profile is only suitable for describing the region of constant orbital speed. It produces a constant orbital speed for all r, something which requires a very high density for low r, and a singularity at $r = 0$. The annihilation rate of dark matter is proportional to the density squared[1], and the extreme behaviour for low r in this profile could therefore be problematic. Moreover, the observed drop in orbital speeds with decreasing r (like that seen in figure 1.1) also suggests that the true density will not be this extreme at small r. Due to these considerations, profiles with less extreme behaviours for small r are generally preferred.

[1] Annihilation requires two dark matter particles. If we interpret the density as the probability of finding a particle within a unit volume, the (uncorrelated) probability of finding two particles within this volume will be proportional to the density squared.

1.2.2 The isothermal profile

The SIS profile can be mended by introducing a finite core radius a, such that $\rho = \text{const.}$ for $r \ll a$, while the behaviour remains unchanged for large r:

$$\rho_{\text{iso}}(r) = \frac{\rho_0}{a^2 + r^2}. \tag{1.12}$$

This profile is generally referred to as the isothermal profile. We see that we can obtain the SIS profile by setting $a = 0$. Since $a = 0$ is not a favoured case, it is common to re-define ρ_0, and express the profile as

$$\rho_{\text{iso}}(r) = \frac{\rho_0}{1 + (r/a)^2}. \tag{1.13}$$

This profile can be fitted to the Milky Way, yielding the parameters $\rho_0 = 1.16\,\text{GeV/cm}^3$, $a = 5\,\text{kpc}$ (using the definition of ρ_0 from eq. (1.13)).

1.2.3 The NFW profile

The perhaps best known and widely used density profile is the Navarro-Frenk-White (NFW) profile [42]. This profile was made to fit the data from numerical simulations of the dark matter halo formation on several size and mass scales; from dwarf galaxies to rich galaxy clusters. The density distribution in this profile given by

$$\rho_{\text{NFW}}(r) = \frac{\rho_0}{(r/a)(1 + r/a)^2}, \tag{1.14}$$

where ρ_0 and a are free parameters which are used to fit the observational data from individual systems to the profile.

As this profile was found through simulations at several scales, it is a universal profile, which can be applied to a range of different systems. We note that this profile does not fall off as r^{-2}, but rather as r^{-1} for small r, and as r^{-3} for large r. Nevertheless, it has been found to be compatible with the Milky Way density profile [34]. The best fit parameters for the Milky Way are $\rho_0 = 0.26\,\text{GeV/cm}^3$, $a = 20\,\text{kpc}$.

1.2.4 Other profiles

All of the above profiles can be expressed as parameterizations of a more general density profile,

$$\rho(r) = \frac{\rho_0}{(r/a)^\gamma \left[1 + (r/a)^\alpha\right]^{(\beta-\gamma)/\alpha}}, \tag{1.15}$$

where α, β, and γ are free parameters. We obtain the NFW profile for $\alpha = 1$, $\beta = 3$, $\gamma = 1$, and the isothermal profile for $\alpha = 2$, $\beta = 2$, $\gamma = 0$. It is common to fit the results from N-body simulations to this profile, and a range of possible profiles exist.

We will, however, not consider any other parameterizations than those mentioned so far.

We will, on the other hand, consider a profile which is not a parametrization of eq. (1.15), namely the Einasto profile,

$$\rho_{\text{Einasto}} = \rho_0 \exp\left[-\frac{2}{\alpha}\left(\left(\frac{r}{a}\right)^{\alpha} - 1\right)\right], \quad \alpha = 0.17. \tag{1.16}$$

This profile is often considered when looking for signals from annihilations of dark matter within our galaxy, and the parameters for the Milky Way are in this profile $\rho_0 = 0.06\,\text{GeV/cm}^3$, $a = 20\,\text{kpc}$.

2 Dark matter in clusters of galaxies

Indications of dark matter exist on several different size scales, and are not restricted to the internal dynamics of galaxies. What is considered to be the first real evidence of dark matter was found by Fritz Zwicky in 1933 by applying the virial theorem to the Coma galaxy cluster. This procedure will be discussed in some detail below, and we will have a look at the result from applying it to the Coma cluster. In section 2.3, we will also have a look at the special evidence for dark matter found in the Bullet cluster.

2.1 The virial theorem

The virial theorem is a relation between the potential energy and the dynamics of an N-body system. In astrophysics, this usually refers to the relation between the potential energy and the kinetic energy in a gravitationally bound, dynamically relaxed system. In the following discussion, the term 'virial theorem' will refer to this astrophysical relation. By dynamically relaxed, we mean that the dynamics (e.g. the velocity distributions) of the system change little over time. The virial theorem is a general relation, and can be applied to a wide range of different systems, as long as the constituent objects are gravitationally bound and dynamically relaxed. A full derivation of the virial theorem will not be given here; we will only go through what is needed to estimate the mass of a galaxy cluster.

As stated above, we assume that we are dealing with an N-body system of gravitationally bound objects. The kinetic energy of object i is

$$T_i = \frac{1}{2} m_i v_i^2, \tag{2.1}$$

where m_i is the mass of the object, and v_i is its speed. The total kinetic energy of the

system is correspondingly

$$T = \frac{1}{2}\sum_i m_i v_i^2 = \frac{1}{2} M \left\langle v^2 \right\rangle, \tag{2.2}$$

where $M \equiv \sum_i m_i$ and $\langle v^2 \rangle = \frac{1}{M}\sum_i m_i v_i^2$.

The gravitational potential energy, U, of the system is given by Newton's law of gravity,

$$U = \frac{1}{2}\sum_i \sum_{\substack{j \\ i \neq j}} G \frac{m_i m_j}{|\vec{r_j} - \vec{r_i}|}, \tag{2.3}$$

where the factor 1/2 prevents double counting. This energy will, of course, depend on the spatial distribution of the objects; i.e. the mass distribution of the system. Since the astrophysical systems we want to study consist of a large number of objects, we can describe the mass distribution by a density profile. For the case of a sphere of uniform density and a radius R, one finds that the gravitational potential energy is given by

$$U = -\frac{3}{5}\frac{GM^2}{R}, \tag{2.4}$$

where M is the total mass of the system. The expression for a system with a more general shape and density profile can according to [47] be described by

$$U = -\alpha \frac{GM^2}{r_h}, \tag{2.5}$$

where r_h is the half-mass radius (the radius of a sphere centered in the system's center of mass that would enclose half of the total mass of the system), and α is a constant of order unity that characterizes the density profile. For galaxy clusters, $\alpha \approx 0.4$ provides a good fit to observations [47].

The mass distribution of a system is not needed in order to derive the virial theorem, but it is needed when it comes to making calculations on a system. The theorem itself can be derived from (2.2) and (2.3) (see for example [47], [17] or [36] for a full derivation), and is given by

$$2\langle T \rangle + \langle U \rangle = 0, \tag{2.6}$$

where the brackets indicate time averages, and are often dropped.

Inserting (2.2) and (2.5) in the virial theorem gives us a relation between the total mass of the system and observable quantities:

$$M = \frac{\langle v^2 \rangle \, r_h}{\alpha G}. \tag{2.7}$$

This mass, inferred by the virial theorem, is often referred to as the virial mass of the system.

2.2 The Coma cluster

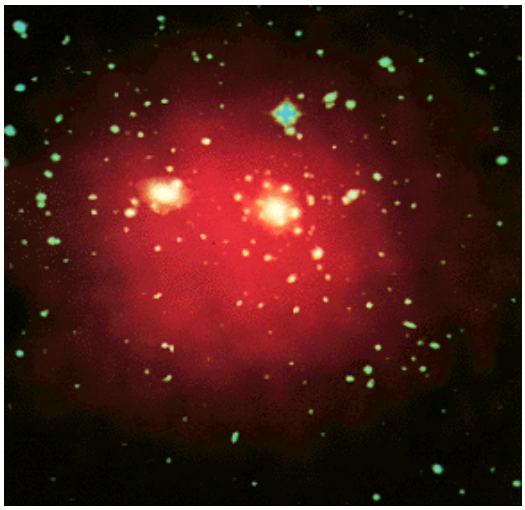

Figure 2.1: Composite image of the Coma galaxy cluster. Blue indicates optical light, and shows an image by the Palomar Sky Survey. The optical image shows mainly the galaxies within the cluster. Red shows X-ray emissions, mainly from hot intracluster gas, and was measured by the Einstein satellite. Image borrowed from the NASA home page.

As a concrete example, we consider the Coma cluster; the same as Zwicky studied in the 30's. The observational data presented below is taken from [47]. For the virial theorem, we can extract the following data:

- Measurements of the redshift of galaxies in the cluster give us the velocity dispersion along the line of sight. If the velocity dispersion in the cluster is assumed to be isotropic, these measurements yield $\langle v^2 \rangle = 2.32 \times 10^{12}\,\mathrm{m^2 s^{-2}}$.
- If the mass-to-light ratio is assumed to be constant (the mass distribution roughly follows the luminosity distribution), and the cluster is assumed to be spherical, the half-mass radius can be estimated to be $r_h \approx 1.5\,\mathrm{Mpc}$.

Inserting this along with $\alpha \approx 0.4$ in (2.7), we obtain

$$M_{\mathrm{virial}} \approx 4 \times 10^{45}\,\mathrm{kg} \approx 2 \times 10^{15} M_\odot, \tag{2.8}$$

where $M_\odot$ is the Solar mass (the mass of our sun). By comparison, the mass of the stars in the cluster is only estimated to be

$$M_{\mathrm{stars}} \approx 3 \times 10^{13} M_\odot, \tag{2.9}$$

which is only roughly 2% of the virial mass. As seen in figure 2.1, the cluster also contains a large amount of hot intracluster gas. The mass of this gas is estimated to be

$$M_{\text{gas}} \approx 2 \times 10^{14} M_{\odot}, \tag{2.10}$$

which is roughly 10% of the virial mass. Even with the large amount of intracluster gas taken into account, almost 90% of the predicted mass of the cluster is unaccounted for. This mass is presumably contributed by a substantial amount of dark matter.

In order to make sure that the predicted mass is not due to incorrect assumptions or unforeseen phenomena, the mass of the cluster can also be estimated in other ways. One way is to calculate the mass that is required for containing the hot intracluster gas. Another is measuring the gravitational lensing effect of the cluster. Mass estimates using these methods are found to be consistent with the estimate from the virial theorem [47][35].

2.3 The Bullet cluster

A different, more unique evidence for dark matter can be found in the Bullet cluster. The Bullet cluster is a special case of two clusters of galaxies that have "recently" collided. In this collision, the majority of the galaxies in both the clusters have just passed through the other cluster without colliding with anything. The intracluster gas of the two clusters, on the other hand, has collided and slowed down, and thus been "left behind" as the galaxies moved on. Due to this, there is a significant spatial separation between the galaxies and the intracluster gas.

As in the case of the Coma cluster, the mass of the gas in the cluster is found to be be higher than the mass of the galaxies. Gravitational lensing measurements, however, show that the mass distribution of the cluster follows the galaxies in the cluster, rather than the gas. This is shown in figure 2.2, and is considered strong evidence for the presence of cold dark matter (see section 3.6 for definition). Cold dark matter interacts very little with both itself and ordinary matter. The dark matter distributions of the two colliding clusters would therefore be expected to go through each other without much interaction. The dark matter distributions should, in other words, follow the movement of the galaxies, something which gives rise to an offset between the mass and gas distributions like that which is currently being observed.

3 Cosmology

The study of dark matter takes place on several different scales, even the biggest. The presence and properties of dark matter has a profound impact on the properties of the Universe at large, and cosmological studies can impose constraints on the possible dark matter candidates. A brief discussion of cosmology is therefore in place.

Figure 2.2: Composite image of the Bullet cluster. The red area shows X-ray emissions from hot intracluster gas. The blue color shows the mass distribution of the cluster, as calculated from gravitational lensing effects. Image borrowed from the NASA home page.

3.1 Fundamental principles

One of the most central concepts when it comes to making theoretical models in cosmology is the so-called cosmological principle. The cosmological principle is the assumption that the Universe is homogeneous and isotropic on the largest scales; in other words that at any given time, general properties such as density and content should be the same anywhere, and from a given point, the Universe should appear the same in all directions. This, of course does not hold on small scales, but observations of the cosmic microwave background (CMB) show that this holds remarkably well at large scales. The CMB will be discussed in more detail in section 3.5.2.

One may be tempted to expand this principle to include time as well, implying that the Universe should remain the same at all times. Theories that incorporate this assumption are known as steady-state theories. While these theories may be philosophically compelling (an unchanging universe with no beginning and no end), they are not supported by observational evidence. Steady-state theories for example have difficulties explaining the relative abundances of hydrogen and helium in the Universe, something which is very well explained by the nucleosynthesis mechanisms of evolving theories.

3.2 The expanding Universe

The dominant view today is that the Universe has a finite age, and was created in an event we call the Big Bang. The question of finiteness in size depends, as we shall

see, on cosmological parameters. The idea that the Universe has a finite age was well motivated by the discovery that the Universe is expanding. It was V. M. Slipher who in 1914 discovered the first signs that the Universe is expanding. When observing the spectral lines of a series of galaxies, he found that the spectral lines most of the galaxies appeared to be redshifted. Using the Doppler formula for small velocities ($v \ll c \equiv 1$),

$$v = \Delta\lambda/\lambda \equiv z, \tag{3.1}$$

the redshift, z, in the spectral lines can be attributed to a recessional velocity, v; the galaxies are moving away from us. λ is here the wavelength of the light in the rest frame of the source, and $\Delta\lambda$ is difference in the observed wavelength between the source and the observer.

Using Slipher's results, combined with his own results from studies of Cepheids in other galaxies, Edwin Hubble found that the recessional velocity of a galaxy is proportional to its distance from us. This relation is today known as Hubble's law:

$$v = H_0 d. \tag{3.2}$$

H_0 is here the Hubble constant, and d is the coordinate distance to the object being observed. The interpretation of Hubble's law is that the Universe is expanding, and that H_0 describes describes the expansion rate of the Universe. The Hubble constant, H_0, has a unit of inverse time, and the Hubble time, $t_H \equiv 1/H_0 \sim 1.4 \times 10^{10}\,\mathrm{yr}$, is interpreted as a characteristic time scale for the age of the Universe. It was Lemaître who first suggested that the Universe is expanding, and through his work, he derived Hubble's law before Hubble did. The significance of Lemaître's work was, however, not recognized at the time.

There has historically been a large uncertainty in the value of H_0. It has therefore been common to define it in terms of a dimensionless parameter, h,

$$H_0 = 100h\,\mathrm{km\ s^{-1}\ Mpc^{-1}}, \tag{3.3}$$

with a value measured by the WMAP satellite to be $h = 0.735 \pm 0.032$ [51]. Quantities depending on H_0 are often expressed in terms of this parameter, separating the uncertainty in H_0 from other uncertainties in the calculations. In principle, the expansion rate of the Universe does not have to be a constant, H_0, but could rather be a function of time, $H(t)$. Modern cosmological models do, indeed, generally operate with a time dependent expansion rate.

We note that the interpretation of the Hubble parameter, $H(t)$, as the expansion rate of the Universe implies that it can be expressed as the ratio of the scale factor of the Universe, $a(t)$, and its time derivative, $\dot{a}(t)$:

$$H(t) = \frac{\dot{a}(t)}{a(t)}. \tag{3.4}$$

The scale factor, $a(t)$, describes the size of the universe, and is commonly normalized such that $a(t_0) = 1$, where t_0 is the present time.

3.3 The geometry of space

The geometry of a homogeneous and isotropic universe with a time dependent scale factor can be represented by the maximally symmetric Friedmann-Robertson-Walker (FRW) metric in comoving coordinates,

$$ds^2 = dt^2 - a^2(t)\left[\left(\frac{dr}{\sqrt{1-kr^2}}\right)^2 + r^2 d\Omega^2\right], \tag{3.5}$$

where

$$d\Omega^2 = d\theta^2 + \sin^2\theta\, d\phi^2, \tag{3.6}$$

and ds is the line element, which describes spacetime separation. The line element is related to the metric, $g_{\alpha\beta}(x)$, through

$$ds^2 = g_{\alpha\beta}(x) dx^\alpha dx^\beta. \tag{3.7}$$

Some further clarification is also in place: The comoving coordinate system is such that the spatial coordinates (r, θ, ϕ) of a "stationary" object are constant in time, even though the Universe expands. By "stationary" we here mean an object that follows the average motion of the galaxies; an object that perceives the Universe as isotropic. Maximally symmetric refers to a universe with a constant and uniform curvature, which in equation (3.5) is described by the constant parameter k:

- $k = +1$: This is called a closed universe, and has a spherical geometry with finite size.
- $k = 0$: This is a flat universe. The (3-dimensional) space is Euclidean, and has infinite size.
- $k = -1$: This is called an open universe. The geometry is hyperbolic, and of infinite size.

Equation (3.5) describes the geometry of a universe that obeys the cosmological principle, and depends on a general time dependent scale factor $a(t)$. In order to obtain information of how this scale factor is connected to observable quantities in our universe, we need the Einstein equation,

$$G_{\alpha\beta} = 8\pi G T_{\alpha\beta} + \Lambda g_{\alpha\beta}. \tag{3.8}$$

G is the Newtonian gravitational constant, while $G_{\alpha\beta}$ is the Einstein curvature tensor, and describes the curvature of the Universe. $T_{\alpha\beta}$ is the energy-momentum stress tensor. For comoving coordinates in the FRW case, this tensor has the form $T_{\alpha\beta} = \mathrm{diag}(\rho, p, p, p)$, where ρ is the energy density of the Universe, and p is the

(isotropic) pressure. The off-diagonal terms describe energy/momentum flux, momentum density, and stress. In a homogeneous and isotropic universe, there should be no large scale fluxes or stress forces, and these terms are thus zero.

Λ is a possible cosmological constant, and corresponds to a non-zero vacuum energy, which, depending on its sign, contributes to expand or contract the Universe. This energy is often referred to as 'dark energy'. The cosmological constant was originally introduced by Einstein in order to obtain a stationary solution for the Universe, but with the discovery that the Universe is expanding, he abandoned it, dubbing it "the biggest blunder in my life". More recent observations, however, indicate that such a constant must be present after all, and it is now a crucial part of many cosmological models.

From the Einstein equation, we understand that the geometry of the Universe is determined by its energy content. A relation between the scale factor of the Universe and observable quantities, such as the matter density, can be found by solving the Einstein equation for the FRW metric, (3.5). It is the $\alpha = \beta = 0$ component that is of interest here, and the solution for this component is the Friedmann equation,

$$H^2 \equiv \left(\frac{\dot{a}}{a}\right)^2 = \frac{8\pi G}{3}\rho - \frac{k}{a^2} + \frac{\Lambda}{3}. \tag{3.9}$$

It is useful to include the cosmological constant in the energy density, ρ, by defining

$$\rho_\Lambda \equiv \frac{\Lambda}{8\pi G}. \tag{3.10}$$

If we now solve the Friedmann equation for ρ, and set $k = 0$, we obtain the critical density; the energy density required for a flat universe:

$$\rho_c \equiv \rho(k = 0) = \frac{3H^2}{8\pi G}. \tag{3.11}$$

It is common to express the abundance of different energy types in the Universe through the density parameter,

$$\Omega_i \equiv \frac{\rho_i}{\rho_c} = \frac{8\pi G\rho_i}{3H^2}, \tag{3.12}$$

where i denotes the "energy species". We further define

$$\Omega \equiv \Omega_{\text{tot}} \equiv \sum_i \Omega_i, \tag{3.13}$$

so that $\Omega = 1$ now corresponds to a flat universe, while $\Omega < 1$ and $\Omega > 1$ correspond to open and closed universes, respectively.

3.4 The constituents of the Universe

The scale dependence of different energy forms can be found using the first law of thermodynamics for an adiabatically evolving system,

$$dE = -p\ dV. \tag{3.14}$$

We assume that the energy forms have an equation of state $p = w\rho$, where w is a constant which characterizes the specific energy form. For (non-relativistic, pressureless) matter, $w = 0$, for radiation, $w = 1/3$, and for the cosmological constant, $w = -1$. Using $E = \rho V$ and $V \propto a^3$, we obtain

$$d(\rho a^3) = -3pa^2\ da = -3w\rho a^2\ da \tag{3.15}$$

$$\frac{d\rho}{\rho} = -3(1+w)\frac{da}{a}. \tag{3.16}$$

Integration then gives

$$\rho \propto a^{-3(1+w)} = \begin{cases} a^{-3} & \text{matter} \\ a^{-4} & \text{radiation} \\ \text{const.} & \text{cosmological constant} \end{cases}, \tag{3.17}$$

or more explicitly

$$\rho(t) = \rho(t_0)\left(\frac{a(t)}{a(t_0)}\right)^{-3(1+w)}, \tag{3.18}$$

where t_0 is generally chosen to be the present time.

The different scale dependencies of the different energy types imply that there should be eras in the lifetime of the Universe, in which different energy forms would dominate. Let us consider an expanding universe that started with a Big Bang, where all 3 terms are present. In this case, radiation would dominate the early Universe. The energy density of radiation drops faster than that of matter as the Universe expands, and after a given time, matter would dominate over the radiation. The energy densities of both matter and radiation drop in time, and the cosmological constant would at some point become the dominant term. Depending on the balance of the different terms, matter may or may not dominate in a period before the cosmological constant takes over. There is, of course, an infinite number of possible density combinations, and we must look to observations in order to find the correct parameters for our universe.

There is, unfortunately, no way that we can directly measure the vacuum energy density that would be connected to a cosmological constant. As we will discuss in more detail later, it can, however, be found using methods of indirect observation. We could, of course, try to make naive estimates for the vacuum energy density using

quantum field theory, but these estimates turn out to yield values that are off from observations by a whopping 120 orders of magnitude!

While the contribution from the cosmological constant can only be found through indirect measurements, the contribution from radiation can be found in a more direct manner. The main contribution of radiation comes from the cosmic microwave background, which will be discussed in more detail in section 3.5.2. The CMB has a black body spectrum with a temperature of $T = 2.725\,\mathrm{K} \pm 0.002\,\mathrm{K}$ [38]. The energy density of a photon gas is related to the temperature through

$$\rho_r = g\frac{\pi^2}{30}T^4, \tag{3.19}$$

where g is the number of degrees of freedom. For photons, the number is 2, corresponding to the possible polarization directions[2]. This yields

$$\Omega_r \sim \Omega_{\mathrm{CMB}} = 2.5 \times 10^{-5} h^{-2} \approx 5 \times 10^{-5}. \tag{3.20}$$

Other contributions to the radiation energy density may also be included, but the difference will not be of orders of magnitude.

Information on the baryon abundance can be calculated from Big Bang nucleosynthesis (BBN). BBN is the process in which the lightest elements were created a few minutes after the Big Bang, and the calculations yield connections between the total baryon abundance and the fractions of the abundances of different elements. The estimated baryon abundance from BBN calculations is [21]

$$\Omega_b h^2 = 0.0224 \pm 0.0009 \tag{3.21}$$

$$\Omega_b \approx 0.04. \tag{3.22}$$

Observations indicate that the Universe should be nearly flat, but the baryonic matter and radiation only seem to amount to a fraction of the energy required for a flat universe. It is therefore clear that a substantial amount of non-baryonic matter and/or a large cosmological constant is needed if our universe is to be flat.

3.5 Finding the cosmological parameters

As mentioned before, indirect observations are necessary in order to find the energy contributions from matter and a cosmological constant to the Universe. There are several observations we can use, for example redshift-magnitude relations for standard candles, as well as measurements of the cosmic microwave background.

[2]If we were to include contributions from relativistic particles (e.g. neutrinos) as well, an approximate solution could be found by replacing $g = 2$ with an effective number of degrees of freedom.

3.5.1 Redshift-magnitude relation

A standard candle is an astrophysical object whose luminosity is known, and as the Universe expands, the light from these objects is redshifted. For the large distance scales needed to observe the geometry of the Universe, type I supernovae are frequently used. Supernovae have a high luminosity, and can be observed at large distances, where other standard candles, such as Cepheid stars can not. For a given cosmological model, one can find a relation between the observed flux, f, the luminosity, L, and the redshift, z. As an example, the redshift-magnitude relation for a flat, matter dominated ($\Omega_m = 1$) FRW model is given by [28]

$$\frac{f}{L} = \frac{H_0^2}{16\pi} \frac{1}{(1+z)(\sqrt{1+z}-1)^2}. \tag{3.23}$$

Inserting the measured flux and the expected luminosity on the left-hand side, and the Hubble constant and measured redshift on the right-hand side, shows us how well this model fits. If both sides of the equation are equal, the model (in this case, a flat, matter dominated FRW model) successfully describes the observations. A significant discrepancy between the two sides implies that the model is off, and that a different model may be more suitable. By applying the redshift-magnitude relations for different cosmological models to supernova data, one can find out which models best describe these observations.

3.5.2 The cosmic microwave background

The cosmic microwave background is, as the name suggests, background radiation in the microwave range. In accordance with the cosmological principle, this background radiation is highly isotropic, and as mentioned in section 3.4, it is a blackbody spectrum with a temperature $T = 2.725\,\mathrm{K}$. While the CMB does not contribute much to the energy density of the Universe, it holds precious information on the contributions from other constituents. Extracting this information is somewhat involved, and we will only present the details required to get an overview of this process. The information in this section was found in [47], and we refer to this book for a more detailed description.

The cosmic microwave background is remnant radiation from the time after the Big Bang. In the time leading up to approximately 0.24 Myr after the Big Bang, the Universe was hot enough that baryonic matter had the form of ionized plasma, and the radiation density was significant. Any atomic states would quickly be ionized in interactions with high energy photons. Since the matter was ionized, a significant amount of free charged particles were around, on which photons would scatter (most importantly free electrons). Due to the frequent scattering through these processes, the Universe was effectively opaque to radiation.

As the Universe expanded, the temperature went down, and so did the interaction rates. Around 0.24 Myr after the Big Bang, at a temperature of roughly 3700 K, the

Universe was cold enough for the ions and electrons to form neutral atomic states. This is a period referred to as recombination. With the charged particles more or less out of the way, the Universe became transparent, and the photons could move freely[3]. This radiation is still observable today as the cosmic microwave background, and is an image of the last scattering surface; an image of the Universe at the time when the photons decoupled.

While highly isotropic, the cosmic microwave background has some minor fluctuations of order $\delta T/T \sim 10^{-5} - 10^{-4}$. These anisotropies have been measured by several experiments, such as WMAP, and can be seen in figure 3.1. The temperature fluctuations in the CMB arose from density fluctuations in the matter of the early Universe. Their angular scales are connected to their spatial size as the Universe became transparent, as well as the evolution of the Universe after this time.

Since the fluctuations are distributed on a spherical surface, it is convenient to express them in terms of spherical harmonics:

$$\frac{\delta T}{T}(\theta, \phi) = \sum_{l=0}^{\infty} \sum_{m=-l}^{l} a_{lm} Y_{lm}(\theta, \phi). \tag{3.24}$$

To study the spatial scales of the anisotropies, it is common to use the two-point correlation function

$$C(\theta) = \left\langle \frac{\delta T}{T}(\hat{n}_1) \frac{\delta T}{T}(\hat{n}_2) \right\rangle_{\hat{n}_1 \cdot \hat{n}_2 = \cos(\theta)}, \tag{3.25}$$

which is defined as the average product of the temperature fluctuations in two points on the celestial sphere, separated by an angle θ. In terms of the spherical harmonics, the correlation function can be written as

$$C(\theta) = \frac{1}{4\pi} \sum_{l=0}^{\infty} (2l+1) C_l P_l(\cos(\theta)), \tag{3.26}$$

where P_l are the Legendre polynomials. The terms C_l can be interpreted as measures of the temperature fluctuations at the angular scales $\theta \sim \pi/l$. The multipoles, l, thus correspond to the angular scales of the fluctuations.

We note that many papers use δT, rather than $\delta T/T$ in the spherical harmonic expansion and correlation function. This is the case in figure 3.2, which shows the power spectrum of the CMB, as measured by the WMAP satellite. C_l^{TT} in this figure corresponds to $C_l T^2$ in our definition. The quantity of the vertical axis is a commonly used measure for the contribution to the temperature fluctuation from a given multipole l.

[3]Strictly speaking, recombination is often defined as the time when the number densities of charged and neutral particles were equal. The time at which photons decoupled (stopped frequently interacting with the matter) came somewhat later.

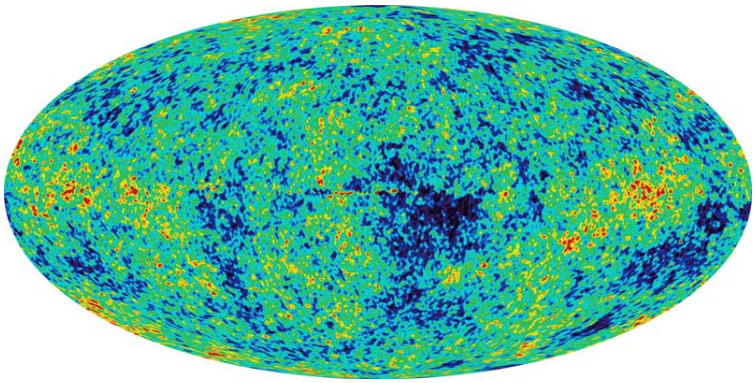

Figure 3.1: Image of the CMB temperature anisotropies across the sky, as observed by the WMAP satellite. The temperature range is $\pm 200\,\mu$K from the average temperature, where dark blue is colder, and red is hotter. Image credit: NASA/WMAP Science Team.

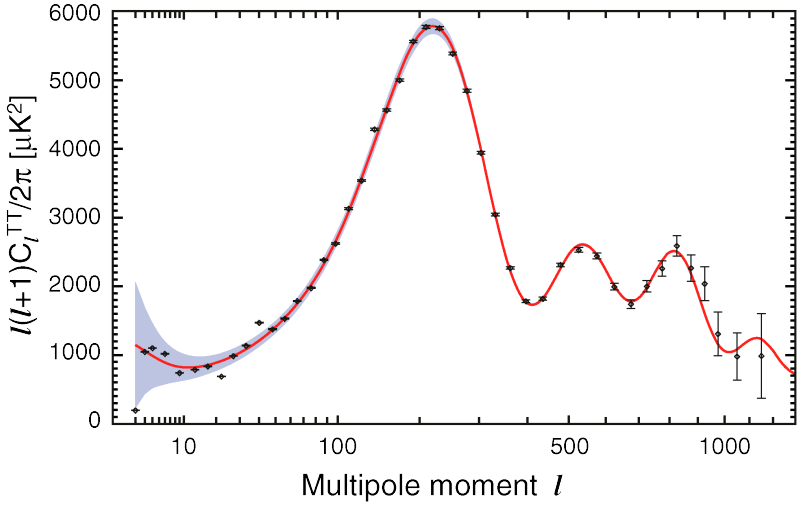

Figure 3.2: Angular power spectrum of the cosmic microwave background, as measured by the WMAP satellite. Image credit: NASA/WMAP Science Team.

The first peak in the power spectrum is of particular importance to cosmology, as its position (in terms of l) holds information the geometry of the Universe. The observed angular scale of an object is smaller in a negatively curved universe ($k = -1$) than in a flat universe ($k = 0$). Correspondingly, the angular scale would be larger in a positively curved universe ($k = +1$). For the power spectrum, this means that the first peak would be further to the left for a positively curved universe, and further to the right for a negatively curved universe[4]. From the position of this peak, the first year WMAP result [11] gave a value

$$\Omega_{\text{tot}} = 1.02 \pm 0.02, \tag{3.27}$$

which is consistent with a flat universe.

In the time leading up to recombination, cold dark matter had already been decoupled from baryonic matter and radiation for a long time (see section 3.6). As long as the Universe was radiation dominated, free streaming (particles moving in random directions at relativistic velocities) prevented structures from being formed. When the Universe had cooled enough to reach matter-radiation equality ($\rho_m = \rho_r$), however, free streaming diminished. Fluctuations in the dark matter density now lead to gravitational wells, into which the baryonic matter accumulated, thus creating regions of higher density[5]. Without the presence of cold dark matter, such density anisotropies would in the time before recombination largely be erased by interactions with the photons. We note that hot dark matter, i.e. dark matter particles moving at relativistic velocities at this time, would contribute to the creation of large scale structures, but also tend to erase small scale structures.

Gravitational wells due to dark matter, as well as a multitude of other effects related to the constituents of the Universe at this time, all have characteristic impacts on the CMB temperature power spectrum. By taking all these effects into account, and fitting different cosmological models to the observed power spectrum, we can find which model best describes the observations. The best fit model to the CMB observations is currently the ΛCDM-model, which depicts a flat universe that is dominated mainly by a cosmological constant (Λ) and cold dark matter (CDM). The most recent results from fits to this model are [30]:

$$\Omega_\Lambda = 0.728^{+0.015}_{-0.016} \tag{3.28}$$

$$\Omega_m h^2 = 0.1334^{+0.0056}_{-0.0055} \tag{3.29}$$

$$\Omega_b h^2 = 0.02260 \pm 0.00053. \tag{3.30}$$

[4]We note that since the observed angular scales of the CMB anisotropies also depend on the "distance" to the last scattering surface, the position of the peak also depends on the value of the Hubble constant, H_0.

[5]Other effects, such as standing pressure waves in the infalling baryonic matter, are related to such gravitational wells.

Ω_Λ, Ω_m, and Ω_b are the density parameters for the cosmological constant, total matter abundance, and baryons, respectively. $h \approx 0.7$ is, as always, the parameter containing the uncertainty in the Hubble constant, as defined by eq. (3.3). We note that the baryonic contribution, (3.30), is quite consistent with the estimate from Big Bang nucleosynthesis, (3.21). By inserting for h, we also see that the contributions from baryonic matter and the cosmological constant are not sufficient to ensure a flat universe. For this, a substantial amount of dark matter is required, as seen in the discrepancy between Ω_m and Ω_b.

To sum it up, we find that the Universe is (very close to) flat, and that the energy content is made up of approximately 73% dark energy, 23% dark matter, 4% baryonic matter, and $\sim 10^{-5}$ radiation. The required amount of dark matter and restrictions on baryonic matter from these cosmological studies add to the evidence for dark matter that we have already shown from galaxies and clusters. The fact that evidence can be found on so many different scales makes it all the more compelling.

3.6 Freezeout of dark matter

The early Universe was very hot and dense; hot enough for heavy hypothetical particles to be created through various interactions. It is common to divide proposed dark matter candidates into two groups, according to their behaviour in this early Universe: Thermal dark matter, and non-thermal dark matter.

Thermal dark matter consists of particles that were once in thermal equilibrium with the radiation and the ordinary matter in the Universe. This means that dark matter particles could be created or destroyed through reactions like[6]

$$\chi\chi \longleftrightarrow \nu\bar{\nu}, \tag{3.31}$$

and exchange energy with ordinary matter through reactions like

$$\chi\nu \longleftrightarrow \chi\nu. \tag{3.32}$$

In thermal equilibrium, dark matter would be created and destroyed at equal rates, and reactions like (3.32) would keep the temperature of the dark matter equal to that of the matter and radiation in the Universe[7]. We can, in other words, obtain information on the abundance and clustering properties[8] of thermal dark matter today

[6]We assume that the dark matter particles are Majorana particles; particles that are their own antiparticles: $\chi = \bar{\chi}$.

[7]Dark matter cannot interact directly with photons (radiation), but most of the ordinary matter can. The ordinary matter would thus be in equilibrium with the radiation, and if the dark matter was in equilibrium with the ordinary matter, it would be so with the radiation as well.

[8]The clustering properties of dark matter are directly related to its velocity distribution at freezeout.

through knowledge of its interactions with ordinary matter and the conditions in the early Universe. This will be discussed in more detail below.

In contrast to thermal dark matter, non-thermal dark matter was never in thermal equilibrium. This implies that this type of dark matter must mainly have been produced through different non-thermal mechanisms. Its temperature and abundance is mainly determined by these mechanisms, and must be be found in different ways than for thermal dark matter. In some cases, the temperature and abundance of such dark matter may have been affected by interactions with ordinary matter in the early Universe, but not enough to reach thermal equilibrium.

In this thesis, we study Weakly Interacting Massive Particles (WIMPs) as dark matter, which (in most models) means that we are dealing with thermal dark matter. Following [27] and [31], we will go through some of the steps in estimating the current abundance of a WIMP dark matter particle.

As already mentioned, a dark matter particle in thermal equilibrium could interact with ordinary matter through interactions like (3.32) and (3.31). We want to find the abundance of dark matter, and are only interested in interactions like (3.31), as these are the only ones that change the total number of dark matter particles. The interaction rate (annihilation rate) per particle[9], Γ, of these interactions is given by

$$\Gamma = \langle \sigma_{\text{ann}} v \rangle \, n, \tag{3.33}$$

where $\langle \sigma_{\text{ann}} v \rangle$ is the thermally averaged annihilation cross section times relative velocity of the annihilating particles, and n is the number density of the dark matter. In thermal equilibrium, detailed balance dictates that the production and annihilation rates should be equal.

The number density of massive, non-relativistic particles in thermal equilibrium can be described by the Maxwell-Boltzmann distribution

$$n_{eq} = \left(\frac{mT}{2\pi} \right)^{3/2} e^{-m/T}. \tag{3.34}$$

m is here the mass of the particles, and T is the temperature. We understand that if a dark matter particle was to stay in equilibrium, its abundance would be exponentially suppressed. In order to have a significant abundance today, the particles must at some point have gone out of equilibrium.

As the Universe expanded, the temperature went down, and as long as the dark matter stayed in thermal equilibrium, the number density of dark matter particles went down as well. The annihilation cross section, $\langle \sigma_{\text{ann}} v \rangle$, also decreases with decreasing temperatures, thus implying that the interaction rate of the dark matter creation and annihilation processes like (3.31) went down as the Universe expanded. At some point, the density of dark matter particles became too low for annihilations to be effective.

[9]The average rate at which each dark matter particle interacts.

At the same time, the number of ordinary particles with sufficient energy to produce dark matter became too low for creation of dark matter to be effective. When this happened, the total number of dark matter particles became effectively frozen in time, and we refer to this event as chemical freezeout. Chemical freezeout occurred around the time when the interaction rate fell below the expansion rate of the Universe,

$$\Gamma = \langle \sigma_{\text{ann}} v \rangle \, n \sim H. \tag{3.35}$$

At some later point, energy exchanging processes like (3.32) also became ineffective, and the temperature of dark matter decoupled from the temperature of the other constituents. This event is referred to as kinetic freezeout.

It is common to distinguish between hot and cold dark matter by whether or not the particles were relativistic at the time of chemical freezeout. WIMPs are typically cold dark matter, and have non-relativistic velocities at freezeout. Their number density in equilibrium can thus be described by (3.34). Hot dark matter particles are typically very light, and are relativistic at freezeout. An example of a hot dark matter particle is the neutrino. The relativistic velocities of hot dark matter make it difficult for it to clump together via gravitational interactions. Due to this, HDM alone does a poor job explaining the structure formation in the early Universe [31], and cosmological models based mainly on cold dark matter are generally favored.

In order to find the abundance of our WIMP dark matter candidate today, we need an equation that describes the time evolution of the number density. Such an equation can be derived from the Boltzmann equation [52], or simply written down 'by hand':

$$\frac{dn}{dt} = -3Hn - \langle \sigma_{\text{ann}} v \rangle \left(n^2 - n_{\text{eq}}^2 \right). \tag{3.36}$$

The first term on the right hand side comes from $dn/dt = d/dt\,(N/V)$, using $V \propto a^3$ and $H = \dot{a}/a$, and describes the change in density due to the expansion of the Universe. As for the second term, we first note that while eq. (3.33) describes the interaction rate per particle, the total interaction rate is proportional to $\langle \sigma_{\text{ann}} v \rangle \, n^2$. We thus understand that this term describes the net production or destruction rate of dark matter particles due to a difference between the actual number density and the equilibrium number density.

It is common to assume that the entropy, S, of the Universe is constant. We can then find an expression for the time evolution of the entropy density $s = S/V \propto a^{-3}$ in the expanding Universe as well:

$$\frac{ds}{dt} = \underbrace{\frac{ds}{da}}_{-3s/a} \underbrace{\frac{da}{dt}}_{Ha} = -3Hs. \tag{3.37}$$

Assuming that the Universe was radiation dominated at the time of freezeout[10],

[10]This assumption should be checked for the dark matter candidate being considered.

we can make the approximation $\rho_{\text{tot}} = \rho_r$. Since the curvature term in the Friedmann equation, (3.9), is proportional to a^{-3}, while the (radiation dominated) density term is proportional to a^{-4}, the curvature term can be neglected in the early Universe. Thus

$$H^2 = \left(\frac{\dot{a}}{a}\right)^2 = \frac{8\pi G}{3}\rho \equiv \frac{8\pi}{3M_{\text{Pl}}^2}\rho, \tag{3.38}$$

where $M_{\text{Pl}} \approx 1.22 \times 10^{19}\,\text{GeV}$ is the Planck mass. Inserting the relation $\rho_r \propto a^{-4}$ in (3.38), and solving the resulting differential equation, we find that in the early Universe,

$$H(t) = 1/(2t). \tag{3.39}$$

We now introduce the new variables $Y \equiv n/s$ and $x \equiv m/T$, where m is the mass of our dark matter particle. Using $t^{-2} \propto H^2 \propto \rho_r \propto T^4 \propto x^{-4}$, we find that $t = 1/(2H) = t_* x^2$ for some constant t_*. Using this relation, along with our newly defined variables, we combine eq. (3.36) and eq. (3.37), and obtain

$$\frac{dY}{dx} = -\frac{sx}{H}\left\langle \sigma_{\text{ann}} v \right\rangle \left(Y^2 - Y_{\text{eq}}^2\right). \tag{3.40}$$

This relation describes the evolution of Y as the temperature decreases. The abundance of dark matter today can be found by solving this equation numerically, and some possible results are illustrated in figure 3.3. The expression can also be written out further by making assumptions on the expression for the annihilation cross section. We will do neither. Instead, we will rather find an approximate expression for the abundance using the simple freezeout criterion described by eq. (3.35). In order to do so, however, we will need expressions for the temperature dependence of the Hubble parameter and the entropy density. These would also be needed in finding a numerical solution of eq. (3.40).

The energy density for radiation, ρ_r, is given by eq. (3.19), but in order to include contributions from relativistic particles, the number of degrees of freedom for photons, $g = 2$, is replaced by an effective number g_*. Combining eq. (3.38) and eq. (3.19), we obtain a relation between the Hubble parameter, H, and the temperature of the Universe, T,

$$H(T) \approx 1.66\sqrt{g_*}\frac{T^2}{M_{\text{Pl}}}. \tag{3.41}$$

The entropy density of the Universe can be approximated by

$$s(T) = \frac{2\pi^2}{45}g_* T^3 \approx 0.4 g_* T^3, \tag{3.42}$$

where we again can obtain the expression for a pure photon gas by setting $g_* = g = 2$.

We make the assumption that $Y_0 = Y_f$, where f indicates the value at freezeout, and 0 indicates the value today. Combining the equations (3.42) and (3.41) with our

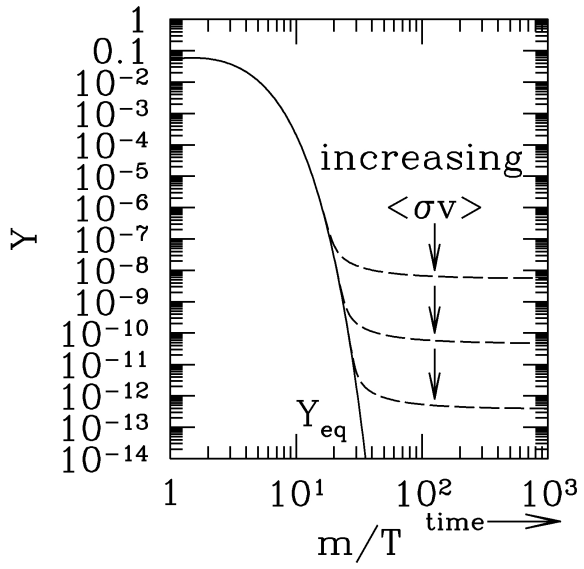

Figure 3.3: The figure shows $Y = n/s$ as a function of $x = m/T$, and describes the evolution of the number density of dark matter for decreasing temperatures. The solid line shows the evolution for a dark matter particle that stays in thermal equilibrium, while the dashed lines show the freezeout of dark matter particles with different annihilation cross sections. Figure borrowed from [27].

freezeout criterion, (3.35), this yields

$$\left(\frac{n}{s}\right)_0 = \left(\frac{n}{s}\right)_f = \frac{4.15}{\sqrt{g_*} M_{\rm Pl} \langle \sigma_{\rm ann} v \rangle T_f}. \tag{3.43}$$

The freezeout temperature, T_f, depends on the annihilation cross section of our dark matter particle. For a known annihilation cross section with a known temperature dependence, this temperature can be found numerically by inserting eq. (3.34) and eq. (3.41) in the freezeout criterion (3.35), and solving for T. For the annihilation cross section of a typical WIMP candidate, one finds [31]

$$T_f \simeq \frac{m}{20}. \tag{3.44}$$

g_* is actually a slowly increasing function of T, and is plotted in figure 3 in [31]. From this figure, we found that for the freezeout temperature of a WIMP with a mass $m = 100\,\text{GeV} - 1\,\text{TeV}$, a value of $g_* \simeq 90$ is appropriate.

Using the above expressions, along with the current entropy density, $s \simeq 4000\,\text{cm}^{-3}$, and critical energy density, $\rho_c \simeq 10^{-5} h^2\,\text{GeVcm}^{-3}$, we can now find the approximate expression for the current WIMP abundance:

$$\Omega_{\rm WIMP} h^2 = \frac{\rho_{DM,0} h^2}{\rho_c} = \frac{m n_0 h^2}{\rho_c} \simeq \left(\frac{3 \times 10^{-27}\,\text{cm}^3\text{s}^{-1}}{\langle \sigma_{\rm ann} v \rangle}\right). \tag{3.45}$$

Incidentally, inserting the annihilation cross section for a typical WIMP candidate with a mass in the weak scale range (few $\times$ 100 GeV) yields the very dark matter abundance required by CMB observations [31]. This is considered a strong piece of evidence for WIMP dark matter, and is rather remarkable, as the derivation of the WIMP abundance from the freezeout condition has nothing to do with weak scale physics. The coincidence that the WIMP abundance predicted by the freezeout condition so well matches the abundance required by observations is often referred to as the 'WIMP Miracle'.

One thing one should keep in mind here, is that the cross section, σ_{ann}, involved in the thermally averaged cross section, $\langle \sigma_{\text{ann}} v \rangle$, depends on the relative velocity, v. It is common to expand the thermally averaged cross section in v^2, such that

$$\langle \sigma_{\text{ann}} v \rangle = \sigma_0 + \sigma_1 v^2 + \sigma_2 v^4 + \cdots = \sum_{i=0}^{\infty} \sigma_i v^{2i}, \tag{3.46}$$

where σ_i are independent of the relative velocity. In principle, σ_0 could be equal to zero, in which case $\langle \sigma_{\text{ann}} v \rangle$ would have a strong velocity dependence. Since the velocities of the dark matter particles were significantly higher at the time of freezeout than they are today, so would, in this case, the thermally averaged cross section. This would imply a much lower annihilation rate for dark matter today than at freezeout, and thus poor prospects for observing dark matter through indirect detection. In order for indirect detection to be a viable approach, the annihilation cross section today must not be significantly smaller than at freezeout.

4 Dark matter candidates

Since the first evidence of dark matter started appearing in the early 1900s, numerous dark matter candidates have been proposed. The candidates range in scale from undiscovered elementary particles to low luminosity galaxies. In this section, we will give an overview of some of the different dark matter candidates that have been proposed. We emphasize that the candidates listed here are only a fraction of the dark matter candidates that are being (or have been) considered.

4.1 Baryonic dark matter

With no knowledge of the cosmological constraints on the energy content of the Universe, baryonic matter would be the obvious place to start the search for dark matter. The dark matter problem is older than the cosmological models of big bang nucleosynthesis and dark matter freezeout, and baryonic matter was for a long time a viable prime candidate. Even though modern cosmological models indicate that most

of the unseen matter in the Universe is non-baryonic, a small fraction of the dark matter should also be of baryonic nature.

Baryonic matter comes in several forms, of which many can be ruled out as dark matter candidates by observation. Large quantities of interstellar dust would, for example, have been observed through the extinction of starlight, while gas clouds would be given away by absorption lines in the spectra of light sources behind the gas. For dark matter within our galaxy, the most likely baryonic dark matter candidates would be Massive Compact Halo Objects (MACHOs). MACHOs can be any massive compact objects with a very low luminosity; objects like dwarf stars, black holes, neutron stars, and Jupiter-like objects. These are objects which either are not massive enough to begin fusion of hydrogen and become stars (brown dwarfs, planets), or remnants of dead stars (black holes, neutron stars, white dwarfs). On galactic scales, some of the missing mass in galaxy clusters could equivalently be contributed by low luminosity galaxies.

Due to the low luminosity of these objects, they are very hard to observe by direct detection. For the MACHO case, it is, however, possible to detect such objects indirectly through gravitational lensing effects. MACHOs have been observed this way, but statistical analysis indicates that at most 19% of the mass of our galaxy can be attributed to such objects [17][31].

4.2 WIMPs

The dark matter candidates that are being considered in this thesis are Weakly Interacting Massive Particles (WIMPs). As the name suggests, WIMPs can only interact with ordinary matter through gravity and through the weak interaction. These hypothetical particles fall in the category of cold dark matter, and can have rest masses in the range from 10 GeV up to tens of TeV (the dark matter abundance from the WMAP data sets a constraint of $m_{DM} < 34\,\text{TeV}$ [13]). WIMPs are especially compelling dark matter candidates due to the WIMP miracle discussed in section 3.6.

There are no WIMP candidates in the standard model, and we therefore have to look to unproven models to find a good WIMP candidate. The extension to the standard model most commonly used in dark matter searches is supersymmetry. As will be discussed in section 7.1, supersymmetric models introduce a large number of new particles, and the lightest particle of such models is often considered as a dark matter candidate.

WIMPs can potentially be detected both directly, through scattering on ordinary matter, and indirectly, through observations of WIMP decay or annihilation products. These detection mechanisms will be discussed in some detail in section 5 and 6.

4.3 Neutrinos

Neutrinos are the only particles in the standard model that only interact weakly and gravitationally. This would in principle make them excellent dark matter candidates. In contrast to other proposed dark matter candidates, neutrinos have also been proven to exist. For some time, a heavy neutrino species was considered as a possible WIMP candidate, but this has since been excluded by experimental neutrino mass limits. The current upper limit on the neutrino mass is $m_\nu < 2.05\,\mathrm{eV}$ (95% C.L.) [13], and neutrinos are currently among the leading hot dark matter (HDM) candidates.

An upper limit on the density parameter for neutrinos can be found by considering the freezeout condition for HDM neutrinos with the current mass limit. This calculation will not be performed here, but yields $\Omega_\nu h^2 \lesssim 0.07$ [13]. Hot dark matter in the early Universe would also contribute to erase small scale anisotropies, and according to [13], an analysis of the CMB anisotropies in combination with large scale structure data suggests an even more stringent limit of $\Omega_\nu h^2 < 0.0067$ on the neutrino density parameter. Both of these limits imply that neutrinos are not the primary component of dark matter.

4.4 Axions

The particles discussed so far are all thermal dark matter candidates; particles that were once in thermal equilibrium. There are, however, dark matter candidates that are non-thermal as well. The axion is one such candidate. The axion was introduced as a possible solution to the CP problem of QCD (why strong interactions do not appear to break the CP-symmetry). Experimental data impose a very low upper limit on the mass of the axion, $m \lesssim 0.01\,\mathrm{eV}$ [13], and they are expected to interact extremely weakly with ordinary matter, thus never having been in thermal equilibrium.

The abundance of this particle depends on assumptions made regarding the production mechanism, but models exist in which the axion has sufficient abundance to be a viable dark matter candidate [13]. If axions do exist, they could potentially be observed through conversion of axions into photons in magnetic fields [31], a mechanism known as the Primakoff effect.

4.5 Superheavy dark matter

While the axion is an extremely light non-thermal dark matter candidate, we find another non-thermal candidate on the other edge of the mass scale: Superheavy dark matter (SHDM), often nicknamed “Wimpzillas”. SHDM particles have masses in the range $m_{DM} > 10^{11}\,\mathrm{GeV}$, and may have been produced gravitationally at the end of inflation. Superheavy dark matter can be motivated by observations of cosmic ray protons with energies above the so-called GZK-cutoff.

The GZK-cutoff occurs at an energy of $\sim 5 \times 10^{19}\,\mathrm{eV}$, where the center-of-mass energy in collisions between protons and CMB photons hits the mass resonance of the Δ-baryon. Interactions between cosmic ray protons and CMB photons above the GZK cutoff lead to pion production, and high energy protons will be suppressed by this mechanism. This means that the Universe will be effectively opaque to high energy protons over distances of $\gtrsim 50\,\mathrm{Mpc}$ [13]. No production mechanisms for ultra-high energy cosmic rays are known to exist within this range, and decaying or annihilating SHDM particles could be a possible solution to this problem.

4.6 Alternative theories

Though dark matter is currently the predominant theory, there are alternative ways to explain observations that are commonly attributed to the presence of dark matter. The strongest alternative to dark matter today is modified gravity. Gravity is the only fundamental force that is yet to be well described by a quantum theory, and it could be that our understanding of gravity for large distances or small accelerations is incorrect. While a fundamental understanding of gravity still seems to be a long way off, theories have been developed that approach the problem by modifying the existing laws of gravity. The simplest of these approaches is Modified Newtonian Dynamics (MOND).

As the name suggests, MOND is merely a modification of Newtonian physics. We will here show how such a modification can be used to explain the rotation curves of galaxies. One way to do this is by modifying the gravitational acceleration as follows:

$$\mu\left(\frac{g}{a_0}\right)\vec{g} = \vec{g_N}, \tag{4.1}$$

where $g = \|\vec{g}\|$, $\vec{g}$ is the original acceleration, $\vec{g_N}$ is the modified acceleration, and a_0 is some natural constant (typically $a_0 \sim 10^{-10}\,\mathrm{m/s^2}$). The function $\mu(x)$ here modifies the acceleration, and has the properties $\mu(x) \to 1$ for $x \to \infty$ and $\mu \to x$ for $x \to 0$.

We note that a more common approach here is not to distinguish between forces, and modify Newton's second law instead:

$$\mu\left(\frac{a}{a_0}\right)m\vec{a} = \vec{F}. \tag{4.2}$$

With a proper choice of a_0 and $\mu(x)$, the gravitational acceleration can be modified to produce flat rotation curves for large r. Consider an object far from the center of the Galaxy, such that $g < a_0$, and thus $g_N = g^2/a_0$. Inserting this in Newton's law of gravity, (1.1), we obtain

$$\frac{GM}{r^2} = \frac{g^2}{a_0}, \tag{4.3}$$

where M is the mass enclosed by the sphere of radius r. Inserting the relation between orbital speed and radial acceleration for circular orbits, (1.2), and solving for v, we obtain

$$v = \sqrt[4]{GMa_0}. \tag{4.4}$$

At this large distance, most of the mass of the Galaxy is contained within the radius r, and M does not increase significantly with increasing r. This implies a roughly constant rotation curve for large r.

Theories of modified gravity can explain many of the phenomena that are usually attributed to the presence of dark matter. In theories of modified gravity, the equations behind the discussion on cosmology would also be modified. The dark matter abundance required by cosmology is therefore not enough reject such theories. Theories of modified gravity do, however, have problems of their own. Cases like the Bullet cluster, discussed in section 2.3, are, for example, difficult to explain without the presence of unseen matter. A certain amount of dark matter is also generally required to explain large scale cosmological structures in these theories as well.

5 Direct detection of dark matter

There is a wide range of possible types of dark matter, and the different types may be detected in different ways. In this thesis, we concentrate on the case of dark matter in the form of unknown particles. When searching for a new particle, the obvious place to start is trying to detect it directly. Since dark matter particles in most models interact with other matter only through gravity and weak interactions, direct detection is a difficult endeavor. The case of purely gravitational interaction is not excluded, but the prospects of proving the existence of dark matter would not be very promising. The dark matter of interest in this thesis is weakly interacting massive particles, and we will in this section discuss direct detection of such particles.

Since observations indicate that the Milky Way contains a large amount of dark matter, our solar system should be passing through such matter at all times. The dark matter halo of the Galaxy is not believed to rotate along with the Galactic disk, and we should thus experience a directionally dependent flux of dark matter. Moreover, this flux should have an annual modulation due to the Earth's movement around the Sun, thus having extrema on June 2 and December 2.

As WIMPs interact through the weak interaction, they can interact with ordinary matter. The cross sections for these interactions are very small, but it could still be possible to detect WIMPs directly through elastic scatterings on ordinary matter in a detector. In contrast to e.g. photons, WIMPs typically scatter off the nucleus of an atom rather than the surrounding electrons. In such a scattering processes, the target nucleus will be recoiled, and the recoil energy may produce a detectable signal, whose nature depends on the detector. Events like these will typically ionize

the detector material, and ionization measurements is a standard way to detect dark matter interactions. One can either detect the ionization directly through the released electrons, or by utilizing scintillating materials, which produce photons in these ionization events. Another, more direct way to detect recoils from dark matter interactions, is through the heat/sound (phonons) generated in the interactions.

The predicted event rate for the case of neutralinos as dark matter candidates (see section 7.1) lies in the range of 10^{-6} to 10 events per day and kilogram of detector material [10]. This, of course, depends greatly on the parameters of the supersymmetric model, and also depends on the detector material being used. With such event rates, it is crucial to be able to distinguish between signals from WIMP scatterings and signals from other sources.

Detectors with both ionization and phonon measurements are especially good at discriminating between WIMP interactions and background sources. As mentioned earlier, WIMPs predominantly interact with the nuclei of the atoms in the target material. Electron recoils are therefore likely be due to background processes. Detectors that measure both ionization and phonons are able to discriminate between electron and nuclear recoils. This is done by finding the ratio between the ionization and the phonon recoil energy in a scattering event, a quantity known as the ionization yield. For a given amount of energy transferred (corresponding to a given phonon energy), electron interactions will produce a higher ionization (and thus ionization yield) than a corresponding nuclear interaction.

There are certain general steps and considerations that may be taken in order to reduce the influence of background signals. For example, in order to avoid influence by cosmic rays of any kind, direct dark matter detectors are generally placed in deep underground locations, such as tunnels or mines. Detectors with good positional (and temporal) resolution are favorable, as they are able to determine if a signal originates near the surface of the detector. WIMP signals would be distributed uniformly in the detector, while external background particles often have short penetration depths, and mainly produce signals near the surface. Signals originating near the surface are, in other words, likely produced by background sources, and may thus be discarded. In addition to the general considerations, one should also identify and reduce the influence of individual background sources. There are several background sources to consider, and we list some of the more important ones [9]:

- Especially for scintillating detectors, one of the most important background sources is gamma rays. The gamma rays that may affect these detectors are produced by radioactive decays in surrounding materials. In addition to the measures mentioned above, further shielding and clever choice of materials can also significantly reduce the background from gamma rays. Gamma rays may also scatter on electrons in the detector, producing electron recoils. Many modern detectors can, however, discriminate between electron and nuclear recoils through the ionization yield.

- Electrons are also an important background source. Electrons, like photons, mostly produce electron recoils, which may be identified through the ionization yield. Electrons may originate from cosmic rays, but in sufficiently shielded facilities, the main source is β-decays in the materials surrounding the detector. External electrons will generally interact near the surface of the detector, and can be discarded by detectors with sufficient positional resolution.

- Fast neutrons is a background source that is difficult to distinguish from WIMP signals. Neutrons, like WIMPs, will generally produce nuclear recoils, and an interaction from a neutron with an energy of a few MeV may produce a signal that is indistinguishable from that of a WIMP. Neutrons do, however, tend to produce multiple interactions, whereas WIMPs only produce single interactions due to their low scattering cross sections. Simultaneous signals are therefore usually discarded as background. Fast neutrons can be produced as end products of cosmic ray interactions or in radioactive decays. Eliminating the neutron background completely is difficult, but shielding may help by slowing the neutrons down.

- Neutrino interactions would be indistinguishable from WIMP interactions on a per-event basis. This background is, however, only expected to be relevant for very large detectors.

The measures taken to reduce background influence in modern detectors are extensive, and the CDMS II collaboration claim to have a misdetection factor of $< 10^{-6}$ for electron recoils [5]. Even so, the event rate of dark matter interactions is extremely low, and the results may still be prone to errors and unforeseen background.

One of the best indicators of an actual WIMP signal was mentioned earlier, namely the observation of an annual modulation of the signal. A signal with such periodicity and a modulation of 8σ has actually been observed by the DAMA experiment. The result has, however, been highly disputed; especially so due to null-results in other detectors, such as CDMS and XENON [44]. The data is also criticized because the observed modulated signal is near 3 keV, an energy range where the detector efficiency drops significantly, and which is close to the 3.2 keV peak expected in the background from ^{40}K decays [9]. It is also worth noting that DAMA lacks the mechanisms mentioned above for identifying electron recoil events, and that the resulting data thus will contain radioactivity background as well as possible WIMP signals [9].

The modulation is what makes the DAMA signal interesting, and many efforts have been made in trying to consistently combine the signal with the non-observations of other experiments. Possible explanations exist, but it will ultimately be up to future experiments to draw a conclusion in this matter.

6 Indirect detection of dark matter

As previously stated, the purely weak and gravitational interactions of dark matter makes direct detection a difficult affair. Assuming that we are dealing with relatively heavy weakly interacting massive particles, a more promising approach could be to look for signs of annihilation or decay of dark matter particles. As will be discussed section 7.1, we will in this thesis be using the lightest MSSM neutralino as dark matter particle. In the R-parity conserving model we are using, this is a completely stable particle. The case of annihilating dark matter particles will therefore be our prime example.

The annihilation of two dark matter particles could produce a range of known detectable particles, but their flux would be relatively low compared to the typical cosmic ray fluxes from other astrophysical processes. The best hope of detecting such events would therefore be to find particle channels or energy ranges that are uncommon among known astrophysical processes. It is, of course, necessary for the chosen signal particle to have a sufficiently long lifetime. Otherwise, the particle would decay before reaching Earth, becoming a secondary source to other particle channels. If suitable particle channels and energy ranges can be found, the flux from these events should appear as an excess in one or more cosmic ray channels, above the expected astrophysical background.

6.1 Ordinary cosmic rays

In this section, the term 'ordinary cosmic rays' refers to cosmic rays of matter or photons, but not antimatter. The case of antimatter will be discussed in section 6.2.

The main constituents of cosmic rays are protons and helium nuclei, constituting almost 90% and 9% [15]. Contributions from electrons and heavier nuclei are both of order 1%. Supernova remnants are likely the main sources of these cosmic rays, and the production mechanism involves acceleration of matter through blast waves [15]. Because ordinary cosmic rays are so common, the prospects of being able to identify a dark matter annihilation signal in any of the ordinary charged particle channels are not too promising. The astrophysical background is simply too strong, and the weak signal from dark matter annihilations would be drowned by the background.

There are, however, two neutral channels which are often considered in the search for dark matter annihilations, namely gamma ray photons and neutrinos. These channels are not rid of background, but have certain advantages that many other channels do not:

- Neutral particles are unaffected by Galactic magnetic fields, and are thus hardly deflected on their path from the source to us. This means that directionally sensitive detectors could be able to identify whence the incoming cosmic rays originate. Gamma rays from dark matter annihilations are expected to be

observable in terms of anisotropies in the cosmic gamma ray background (CGB). The CGB has been found to be isotropic to leading order, but more sensitive experiments with a higher angular resolution, such as the Fermi gamma-ray space telescope, are hoped to detect anisotropies, possibly revealing the occurrence of dark matter annihilations [8].

- Photons and (especially) neutrinos are less prone to scattering and interactions with interstellar matter than other cosmic rays. Very little of the primary signal is therefore lost, and since few other energy loss mechanisms exist for these particles, the signal would also be mostly unchanged.

- With little interaction, inability to decay, and velocities of (roughly) the speed of light, photons and neutrinos have a very long range. This makes it possible to use these particle channels for dark matter searches outside our own galaxy. This may include satellite galaxies, extragalactic space, galaxy clusters, and emissions from the early Universe [53].

Of the two particles, photons are by far the easiest to detect. Since neutrinos interact only through the weak interaction, extremely large detector volumes are needed to detect them. Even with the kilometer size of the newly completed IceCube neutrino observatory, the expected event rate is only in the range of "several" per year. Despite of the low event rate, the neutrino channel is still a viable option for dark matter searches. Monte Carlo calculations show that in at least some dark matter models models, a neutrino signal from dark matter annihilations in the center of the Sun or the Earth should be detectable by existing and upcoming neutrino telescopes. Such signals could also be detectable from annihilations in the Galactic center or halo [37].

In summary, gamma rays and neutrinos are seemingly the only "ordinary" cosmic ray channels with good prospects of detecting a dark matter annihilation signal. For nuclei and other charged particles, there are simply too many ordinary astrophysical background sources. The low degree of deflection of photons and neutrinos during propagation makes directionally dependent detection possible. This way, a signal may be also detected through anisotropies in the cosmic ray flux, and not just through excesses alone. Simulations utilizing this have been made for both gamma rays and neutrinos, and will eventually be tested against data that are being collected by ongoing experiments.

6.2 Antiparticle channels

There is a distinct matter-antimatter asymmetry in the Universe. There is no evidence to suggest that there is any significant amount of antimatter around; on the contrary, the lack of the high intensity gamma ray fluxes that would result from collisions between bodies of matter and antimatter implies that there should be very little antimatter around.

Astrophysical processes producing cosmic rays of antimatter do exist, but they are far less common than those producing ordinary cosmic rays. In contrast to ordinary cosmic rays, which are mainly produced through processes that only involve acceleration of existing matter, cosmic rays of antiparticles must be produced in processes involving pair production. Since antiparticle cosmic rays are so much rarer than ordinary cosmic rays, the astrophysical background for a dark matter annihilation signal to overcome is significantly lower in antiparticle channels than in the corresponding particle channels. In a hypothetical WIMP annihilation processes, the amounts of matter and antimatter produced should be equal, and antiparticle channels should therefore be especially suitable for dark matter searches.

Like ordinary matter, antimatter can exist both in the form of free elementary particles, and in the form of (anti)nuclei. Antinuclei are, however, difficult to produce, and as we shall see, only the lightest antinuclei are realistic candidates for observation. The number of viable antiparticle channels is further be narrowed down by considering lifetimes of the particles. In the end, the antiparticle channels worth considering can be found by looking to the ordinary cosmic ray equivalents. Antiprotons, positrons (anti-electrons), and light antinuclei are the antiparticle channels that are being considered in searches for a dark matter annihilation signal. Background sources exist for all these antiparticle channels, but as mentioned earlier, they are much less significant than those for the corresponding particle channels.

Heavy antinuclei are not known to be produced in ordinary astrophysical processes, but while detection of such nuclei would be a very strong indication of the existence of dark matter, the conditions required to produce them imply that they should be extremely rare. The coalescence model of nucleus formation, which will be introduced in section 8, can be generalized to heavier nuclei, and requires all the constituent nucleons to have a momentum difference smaller than some maximum value, p_0, in order to produce a nucleus. In any astrophysical process (including dark matter annihilations), this condition would be extremely rarely fulfilled for more than a couple of nucleons at a time. Very light nuclei, such as antideuterons, would therefore realistically be the only observable candidates.

The coalescence condition is very strict, and the flux of even the lightest antinuclei would be very low compared to that of antiprotons and positrons. The best place to start would therefore be to look for an excess over the expected astrophysical background in the positron and antiproton channels.

6.2.1 Positrons

Dark matter annihilations would (in most models) be able to produce electron-positron pairs, and a resulting positron signal might be observable. Positrons are known to be produced in collisions of cosmic ray nuclei on interstellar matter (secondary production), and this is believed to be the main production mechanism. The hope is to observe an annihilation signal as an excess from this background in the positron fraction,

$$\frac{\phi(e^+)}{\phi(e^+) + \phi(e^-)}, \tag{6.1}$$

where $\phi(X)$ denotes the flux of a particle X.

Experiments such as HEAT, AMS-01, PAMELA, and Fermi LAT have all observed such an excess [14], something which has created great excitement, and motivated the search to find suitable dark matter models that can describe it. Figure 6.1 shows the positron fraction as measured by the PAMELA satellite. The black line shows the expected astrophysical background from secondary production, while the red data points show the PAMELA data. We notice that the expected background decreases with increasing energies. The reason for this is related to the residence time of cosmic ray particles in the Galaxy, and the fact that the energies of the positrons are related to the energies of the cosmic ray particles that produced them. High energy particles move quickly through the Galaxy with little deflection, and have little time to interact with interstellar matter. This low number of interactions again leads to a correspondingly low positron flux at high energies. Going to lower energies, the cosmic rays are more deflected when moving through the Galaxy, and thus have a higher residence time. This gives them more time to interact with the interstellar matter, and thus a higher probability of producing electron-positron pairs.

The discrepancy in the lower energy range (where the measurements fall below the expected background) can according to [3] be attributed to charge dependent Solar modulation effects. The data that have been causing excitement, is the large excess above $\sim$10 GeV. Somewhat ironically, the size of the excess is actually problematic for the dark matter annihilation scenario. The expected positron flux from the annihilations of a typical thermal WIMP candidate turns out to be a factor of order 50 too small to explain the observed excess [29].

This problem has been attempted solved in several ways. The WIMP annihilation rate may, for example, be increased by fluctuations in the dark matter density that cause the dark matter to clump together. This clumping effect would increase the density, and thus also the annihilation rate of dark matter. Other effects, such as Sommerfeld enhancement and resonances may also contribute to an increased annihilation rate [20]. These effects are commonly accounted for by introducing a boost factor, which, if big enough, could make it possible to explain the excess by WIMP annihilations. A sobering alternative is, of course, that the positron excess has

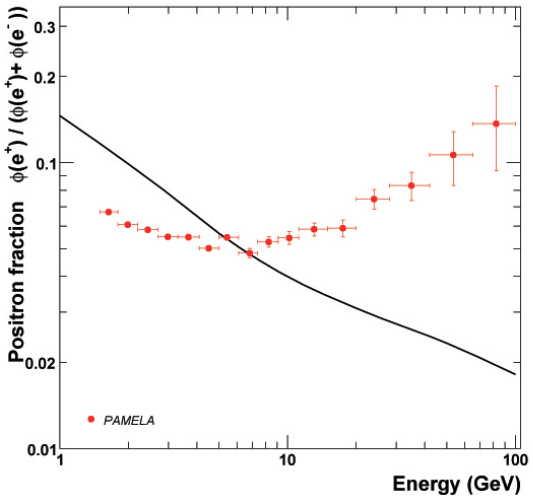

Figure 6.1: Positron fraction, as measured by the PAMELA satellite. The black line shows the expected astrophysical background from secondary production, while the red data points are the PAMELA measurements. Figure from [3].

nothing to do with dark matter at all, but is contributed by an unknown astrophysical source, such as a nearby pulsar. Other alternatives include other dark matter models. For example, [33] claims to succeed quite well in describing the PAMELA excess in a non-thermal WIMP model, without the need for any boost factor. Those results do, however, not succeed in describing the Fermi LAT data.

In summary, the positron excess is a promising observation, but is difficult to explain in terms of dark matter annihilations. Positrons can also be produced in the magnetospheres of pulsars [3], and the presence of nearby pulsars is a strong alternative. In order to correctly interpret the excess, we must be able to distinguish between a signal from dark matter annihilations and signals from other sources. The best way to do so, is to search for dark matter signals in other channels that are consistent with the measured positron excess.

6.2.2 Antiprotons

The antiproton channel is another antiparticle channel where a dark matter annihilation signal could be observable. As with positrons, the main background source of antiprotons is secondary production from collisions of cosmic ray particles on interstellar matter. The most common reaction is cosmic ray protons on interstellar hydrogen. Due to charge and baryon number conservation, a reaction $p + p \to \bar{p} + X$ must at least produce 3 protons in addition to the antiproton. This imposes a lower energy threshold of $E_p = 7m_p$ for the incoming proton in the rest frame of the ISM

proton [12]. The incident proton will, in other words, have a high momentum, and taking momentum conservation into account, this means that the antiproton is less likely to be produced with a low kinetic energy. As in positron case, the expected background flux decreases with increasing energies, but is suppressed below a few GeV due to the production energy threshold.

Such a suppression should not be present for antiprotons from dark matter annihilations, and there was initially hope was to find an excess from dark matter annihilations in the low energy region. Early studies actually suggested that such an excess was present around 1 GeV [15], something which motivated further studies. We now have a better understanding of the secondary antiproton production mechanisms, as well as the propagation through the Galaxy. It has been found that cosmic ray collisions involving heavier nuclei (e.g. helium) can produce antiprotons well below the threshold for $p - p$ collisions. Moreover, tertiary production mechanisms, such as non-annihilating inelastic scattering of the antiprotons on interstellar matter, contribute by shifting high energy antiprotons towards the lower parts of the spectrum. With improved understanding and larger amounts of observational data, the excess suggested by the early data diminished.

While PAMELA and other experiments have given promising measurements in the positron channel, the current situation for the antiproton channel is not quite as promising. Measurements have so far been made for kinetic energies up to 180 GeV, and no excess has yet been found that cannot be explained in terms of secondary production mechanisms [4]. Figure 6.2 shows the data for the antiproton channel measured by PAMELA, and as we can see, the data can be well explained by the models for the astrophysical background flux.

Though annihilations of heavy dark matter likely should produce some amount of antiprotons, the occurrence of such events is not ruled out by the current non-observation of an excess antiproton signal. There are several possible options:

- The dark matter mass could be high enough that the energies of the resulting antiprotons fall above the measured range. The data would in this case impose constraints on the possible masses of dark matter candidates. This case generally requires dark matter with masses in the TeV range.

- Due to high uncertainties in the Galactic propagation models, the lack of a definitive excess does not exclude the possibility that a part of the antiproton flux actually does originate from dark matter annihilations [23]. The signal may simply be a part of what is considered to be the background flux.

- In principle, it is possible that the dark matter could have purely leptonic annihilation channels [20]. This is, however, not supported by most well motivated extensions of the SM, such as the MSSM.

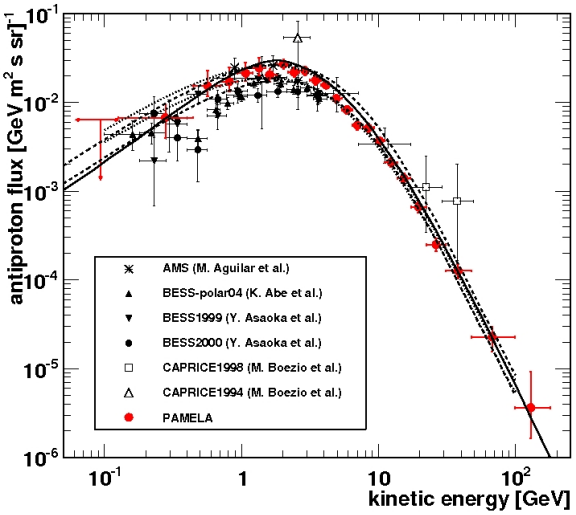

Figure 6.2: PAMELA data for the cosmic ray antiproton flux. The red points are the PAMELA data set, while the other points show the data from other experiments. The lines indicate the expected astrophysical background flux calculated in different models. Figure from [4].

Other explanations are also be possible. More pessimistic perspectives would be that dark matter interacts purely gravitationally, or that it does not annihilate into detectable particles at all. In these cases, the prospects of finding conclusive evidence for dark matter would be bleak. We note that none of the above scenarios require the positron excess to be (fully) explained by dark matter annihilations, and are thus compatible with the likely scenario that the PAMELA positron excess originates from other astrophysical processes.

In the search for a dark matter annihilation signal, the antiproton channel currently seems to be a dead end. Until experiments are launched that can probe higher energy ranges, it is difficult to rule out any of the suggested explanations for the lack of excess in the antiproton spectrum. The data from this channel puts restrictions on the possible dark matter models, but in order to find an observable dark matter annihilation signal, the best choice is to look for other antiparticle channels.

6.2.3 Antideuterons

While more scarce than antiprotons and positrons, light antinuclei may provide channels in which a dark matter annihilation signal can be detected. The Monte Carlo simulations made for this thesis show that the average numbers of antiprotons and antineutrons produced in annihilations of neutralinos with masses in the TeV range are of order 1. Combined with the strict coalescence condition of a momentum

difference less than a maximum value, p_0, between antinucleons in order to produce an antinucleus, it is highly unlikely that these annihilation events would produce any antinuclei heavier than antideuterons. The antideuteron channel is therefore the most promising antinucleus channel.

As with the previous antiparticles, antideuterons can also be produced in cosmic ray collisions on interstellar matter. As in the antiproton case, there is also an energy threshold involved in the production of antideuterons. Both the antiproton and antineutron that will make up the antideuteron need to be produced in the same cosmic ray interaction. For the case of a cosmic ray proton colliding with interstellar hydrogen (a $p - p$ interaction), charge and baryon number conservation requires at least 3 protons and 1 neutron to be produced in addition to the antiproton and the antineutron. This imposes an even higher energy threshold on the cosmic ray proton than in the antiproton case.

As before, momentum conservation implies that the antineutron and antiproton are less likely to be produced with low energies. This, however, means that the coalescence condition of a momentum difference less than p_0 between the antiproton and antineutron only will be fulfilled if the two antinucleons have almost equal and parallel momenta. The number of antideuterons produced in these reactions should thus be low, and further suppressed at low energies due to the suppression of the antinucleon production at low energies. When it comes to dark matter annihilations, however, the antinucleons should be produced mainly in low energy ranges [24]. A resulting antideuteron signal from such processes could therefore be possible to detect in the low energy part of the spectrum.

There is currently no observational data available for the antideuteron channel. Searches for cosmic ray antideuterons were performed by by the BESS balloon-borne experiment from 1997 to 2000, but no antideuteron candidates were found [26]. This imposes an upper limit on the flux in the measured energy range. The antideuteron channel is currently one of the most important candidates in the search for a dark matter annihilation signal, and simulations have been made in several models that predict a possible observable excess. The high activity in simulating antiparticle fluxes from dark matter annihilations has motivated upcoming experiments such as GAPS and AMS-02, which are dedicated to measuring antiparticle cosmic rays. The race is therefore on for astroparticle physicists to make predictions for the spectrum in the antideuteron channel, before results from these experiments become available.

Chapter II

Calculation of the antideuteron spectrum

7 The models and programs

The main goal of this thesis is to study the antideuteron flux from WIMP annihilations within our galaxy. As already mentioned, there are no suitable dark matter candidates in the standard model, so the first thing we need to do, is to select a particle physics model that introduces one or more suitable dark matter candidates. Subsequently, we need Monte Carlo event generators that support the chosen model, and that are capable of calculating the source spectrum of antideuterons from these annihilations. With the source spectrum in place, we then need to calculate the final antideuteron flux near Earth using an appropriate galaxy propagation model. The dark matter model model and the Monte Carlo generators will be introduced in this section, while the models for antideuteron production and propagation are discussed in section 8 and 11, respectively.

7.1 Supersymmetry

Since there are no WIMP candidates in the standard model of particle physics, we need to introduce one by using an extension of the standard model. The standard model is not believed to be a complete model, and a large number of extensions exist, which aim to solve different problems. Supersymmetry (SUSY) is one of these extensions, and is well motivated by particle physics.

7.1.1 Motivations for supersymmetry

One of the problems many supersymmetric models can solve, is the so-called hierarchy problem of particle physics. We will only give a superficial explanation, and refer

to [6] for more details. The hierarchy problem is a fine-tuning problem, and arises when calculating the radiative corrections to the Higgs boson mass. The one-loop correction to the mass is quadratic in the cutoff, Λ:

$$\delta m^2 \propto \lambda \Lambda^2, \tag{7.1}$$

where λ is the Higgs coupling. The one-loop corrected physical mass of the Higgs boson becomes

$$\mu^2_{\text{phys}} \sim \mu^2 - \lambda \Lambda^2. \tag{7.2}$$

Minimizing the Higgs potential using this mass, and inserting the vacuum expectation value $v \approx 246\,\text{GeV}$, we obtain $\mu_{\text{phys}} \approx \sqrt{\lambda}\,123\,\text{GeV}$. The value of the coupling, λ, should be of order unity, while the cutoff, Λ, should correspond to the energy at which some new physics become important. Quantum gravity is believed to become important near the Planck mass, $M_P \simeq 1.2 \times 10^{19}\,\text{GeV}$. Using this as the cutoff scale, we see that in eq. (7.2), a remarkable cancellation must take place between two terms of order $(10^{19}\,\text{GeV})^2$ on the right-hand side, leaving only the left-hand side term of order $(10^2\,\text{GeV})^2$.

Supersymmetric models introduce a fermionic 'superpartner' for all standard model bosons and vice versa. In supersymmetric models, the radiative correction to the Higgs mass will also include loop diagrams of the fermionic superpartner. The fermionic loop diagrams produce terms with opposite signs of those of the corresponding bosonic loops, and thereby cancel the problematic Λ^2 mass correction.

Another trait of supersymmetry is the unification of the gauge couplings at high energies. As seen in figure 7.1, the electromagnetic, weak, and strong couplings do not evolve towards a unified value in the standard model. If supersymmetry is used, however, the couplings converge for energies above the so-called grand unification scale ($\approx 10^{16}$ GeV). Unification of the couplings is the basis for Grand Unification Theories (GUTs), and supersymmetry is an essential ingredient in many of these theories.

7.1.2 The MSSM

Supersymmetry is not a single model, but rather an umbrella term for a range of different supersymmetric models. In this thesis, we have been using the Minimal Supersymmetric Standard Model (MSSM). The MSSM introduces an additional Higgs doublet, as well as superpartners to this and all the fermions and gauge bosons. Even though the MSSM introduces a large amount of new particles, the term 'minimal' refers to the model being minimal in the number of new particles introduced.

When it comes to the naming conventions for the new particles, the superpartners of the fermions are given the name of the original particle with an s-prefix, while the Higgs and gauge boson superpartners are given an -ino suffix. These naming conventions are also applied to the common names of the particles, and names like

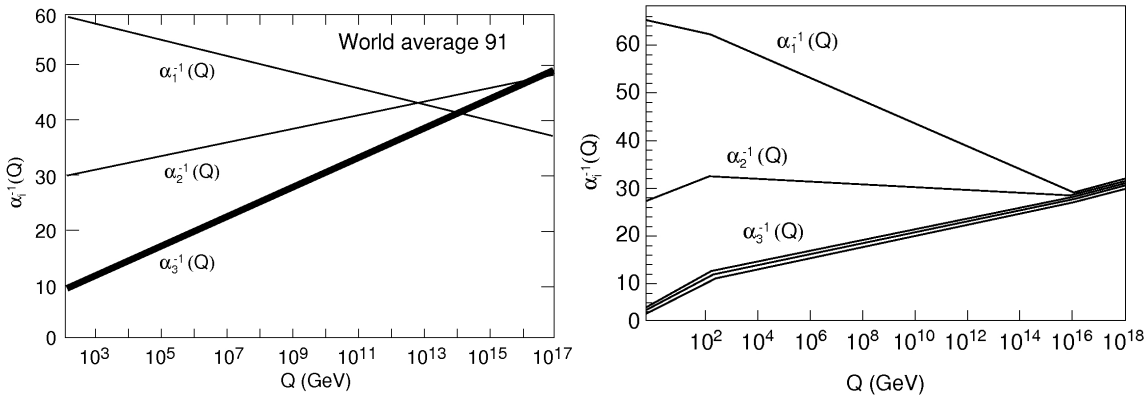

Figure 7.1: The measurements of the gauge coupling strengths at LEP (left) do not evolve towards a unified value in the standard model. If supersymmetry is included (right), however, the couplings converge. Figure borrowed from [13].

'sleptons', 'gauginos', and 'squarks' thus refer to the superpartners of leptons, gauge bosons, and quarks, respectively. A list of the MSSM particles and superpartners is found in table 7.1.

The interaction eigenstates of the MSSM superpartners are not necessarily the same as the mass eigenstates. For the superpartners of the Higgs and gauge bosons, the mass eigenstates are superpositions of the interaction eigenstates. As seen in table 7.1, the superpartners of the charged Higgs and gauge bosons (the charged winos and higgsinos) are mixed to produce mass eigenstates called charginos. Correspondingly, the superpartners of the neutral Higgs and gauge bosons (the bino and the neutral wino and higgsinos) are mixed to produce mass eigenstates called neutralinos.

In the search for dark matter, the lightest supersymmetric particle (LSP) is an attractive dark matter candidate. Which supersymmetric particle is the lightest depends on the parameters of the supersymmetric model. A frequently studied case, which we will be using in this thesis, is the lightest neutralino as LSP. When referring to 'the neutralino' later in this thesis, we refer to the lightest of the four, which in our case is the $\tilde{\chi}_1^0$. We note that the neutralino is a Majorana fermion, and is thus its own antiparticle.

Standard Model particles and fields		Supersymmetric partners			
		Interaction eigenstates		Mass eigenstates	
Symbol	Name	Symbol	Name	Symbol	Name
$q = d, c, b, u, s, t$	quark	$\tilde{q}_L$, $\tilde{q}_R$	squark	$\tilde{q}_1$, $\tilde{q}_2$	squark
$l = e, \mu, \tau$	lepton	$\tilde{l}_L$, $\tilde{l}_R$	slepton	$\tilde{l}_1$, $\tilde{l}_2$	slepton
$\nu = \nu_e, \nu_\mu, \nu_\tau$	neutrino	$\tilde{\nu}$	sneutrino	$\tilde{\nu}$	sneutrino
g	gluon	$\tilde{g}$	gluino	$\tilde{g}$	gluino
$W^\pm$	W-boson	$\tilde{W}^\pm$	wino	$\tilde{\chi}^\pm_{1,2}$	chargino
H^-	Higgs boson	$\tilde{H}_1^-$	higgsino		
H^+	Higgs boson	$\tilde{H}_2^+$	higgsino		
B	B-field	$\tilde{B}$	bino	$\tilde{\chi}^0_{1,2,3,4}$	neutralino
W^3	W^3-field	$\tilde{W}^3$	wino		
H_1^0	Higgs boson	$\tilde{H}_1^0$	higgsino		
H_2^0	Higgs boson	$\tilde{H}_2^0$	higgsino		
H_3^0	Higgs boson				

Table 7.1: Standard Model particles and their superpartners in the MSSM. Table borrowed from [13].

7.1.3 R-parity

The MSSM allows interaction terms that violate lepton and baryon number (B and L) conservation. This is problematic, as such terms would allow the proton to decay, a process which has never been observed. Since these quantum numbers are not absolutely conserved quantities, imposing conservation of these numbers is not a good solution to this problem. Instead, a new, multiplicatively conserved quantum number is introduced: The R-parity. The R-parity is defined by

$$R = (-1)^{3B+L+2s}, \tag{7.3}$$

where s is the spin of the particle in question. All standard model particles have an R-parity of +1, while their superpartners ('sparticles') have R-parity -1. Since this quantum number is multiplicatively conserved, any decaying sparticle must decay into an odd number of sparticles. This implies that the LSP in R-parity conserving supersymmetric models (such as the one used in this thesis) is absolutely stable. If the LSP is neutral, (e.g. the neutralino as LSP) it would serve as an excellent dark matter candidate.

7.1.4 Parameterizations and practical considerations

In this thesis, we want to perform calculations for various neutralino mass scenarios. Since the mass spectra of the supersymmetric particles are not independent, we cannot freely change the neutralino mass. The neutralino mass depends on the mixings and

masses of the higgsinos and gauginos, which again depend on the parameters of the supersymmetric model. Not only the mass, but also the interactions of the neutralino depends on these parameters. The higgsinos and gauginos interact differently, and the annihilation cross sections into various channels will thus vary according to the mixing matrix for the neutralino.

The MSSM has more than 100 free parameters, and in order to be able to put it to practical use, the number of free parameters must be reduced. By making well motivated assumptions, parameterizations of the model have been made which have less than 10 free parameters. In order to be able to calculate cross sections and generate events for neutralino annihilations, we have to choose a suitable parametrization of the MSSM, and adjust the parameters in such a way that we obtain the wanted neutralino masses. Several parameterizations exist, and calculators are available for the mSUGRA, NUHM, and AMSB parameterizations at the CERN website [2]. We used the calculator for the mSUGRA parameterization, and obtained the wanted neutralino masses by adjusting the m_0 and $m_{1/2}$ parameters. The spectra can be generated using three different codes (Softsusy, SPheno and Suspect), and we used the spectra generated by the SPheno code in our calculations.

We note that MSSM calculations for high masses rely on precise cancellations between terms that depend on the mass spectra and mixing matrices from the spectrum generators. Unfortunately, the results from the spectrum generators become inaccurate for high masses, and calculations for neutralino masses above a few TeV are therefore unreliable. Supersymmetry scenarios typically operate with neutralino masses in the 100 GeV range, and the spectrum generators simply were not made to handle scenarios with a neutralino mass in the TeV range. To avoid any complications, we therefore perform calculations mainly for neutralino masses below 1 TeV.

7.2 The Monte Carlo generators

After choosing a dark matter model, we need suitable Monte Carlo generators for calculating the antideuteron flux from annihilations of our dark matter particles. The MSSM has already been implemented in certain Monte Carlo event generators, such as MadGraph.

MadGraph can generate events and calculate matrix elements and cross sections for processes with up to 9 external particles. Since MadGraph can only handle 9 external particles, and does not handle hadronization (binding of final state quarks into hadrons), this program is not suited for calculating the nucleon (or antideuteron) production in dark matter annihilation processes. The common approach for such calculations, is to use MadGraph to generate events for tree level annihilation processes like

$$\tilde{\chi}_1^0 \tilde{\chi}_1^0 \longrightarrow W^+ W^- \tag{7.4}$$

and

$$\tilde{\chi}_1^0 \tilde{\chi}_1^0 \longrightarrow q\bar{q}, \tag{7.5}$$

and pass these events on to a different Monte Carlo generator that can handle showering (cascade into lighter particles) of these particles, as well as hadronization of final state quarks. For the MadGraph calculations, we requested 10^5 events. MadGraph may not always be able to produce the requested number of events, but did so for the above tree level diagrams.

After generating the tree level events using MadGraph, we go on by passing these events on to a different Monte Carlo event generator: Herwig++. Herwig++ handles the showering of these particles, as well as hadronization. Herwig++ uses the input events from MadGraph to generate a phase space for the input particles. It can then generate an arbitrary number of events from this phase space, which may also be higher than the number of input events. A higher number of input events will, of course, give a more accurate phase space. With Herwig++, we generally ran calculations for 10^7 events; a factor 100 higher than the number of input events.

While Herwig++ handles hadronization, it does, however, not handle the formation of atoms or nuclei. In order to find the resulting antideuteron flux, we must implement a model for this formation ourselves. For this we use the coalescence model, as one of the aims of this thesis is to investigate how the implementation of this model affects the antideuteron source spectra. In order to perform coalescence, we also specifically set the antineutrons not to decay. This should be physically unproblematic, as neutrons have a long lifetime (885.7s), and would not decay during the time in which nuclei are produced.

In the procedure described above, we calculate the antideuteron spectra from the different annihilation channels separately. The total antideuteron spectrum can afterwards be found by weighting the spectra according to the branching ratios for the different channels. Even if we could calculate the total antideuteron spectrum from all possible annihilation channels simultaneously, there is one good reason not to: Generality. While the branching ratios between the different annihilation channels depend heavily on the nature of the dark matter particle, the antideuteron spectra from the different channels do not. The antideuteron spectrum from two neutralinos annihilating into W^+W^- should not differ significantly from that of a different dark matter candidate (of the same mass) annihilating into W^+W^-. Therefore, by calculating the antideuteron spectra for the different annihilation channels separately, we can obtain the total antideuteron spectrum from a different dark matter candidate of the same mass by applying the appropriate branching ratios.

8 Coalescence

For the fusion of (anti)protons and (anti)neutrons into (anti)deuterons, it is common to use the so-called coalescence model. The coalescence model is based on the simple idea that any nucleons with a momentum difference $\Delta p < p_0$ for some given p_0 will merge with each other to create a nucleus. For collisions with energies as high as the TeV range, one can expect relativistic final state particles. Special relativity must therefore be taken into account. The appropriate reference frame for applying the coalescence prescription would be the center-of-momentum (also called center-of-mass) (COM) frame of the respective antiproton-antineutron pairs.

For a Monte Carlo simulation, the coalescence model can easily be implemented by comparing the momenta of the final state particles from each individual event. The coalescence model was, however, developed before the onset of computational physics, so a coalescence model for individual events was not very useful. Instead, expressions have been developed that apply to particle densities dN/dk^3 in momentum space. After some assumptions, expressions can then be made which apply to the particle energy spectra, dN/dT, as will be shown in section 8.2. Particle energy spectra are found by measuring the final state nucleon energies in a large number of events, and can also be found experimentally.

Even though it is possible to do coalescence per-event in Monte Carlo simulations, it is common to use the traditional approach which applies to the nucleon energy spectra from the Monte Carlo instead. This was, for example, done by Bräuninger et al. in [14]. In this thesis, we will discuss and compare the two different approaches, and we will also examine validity of the assumptions needed to perform coalescence with energy spectra.

Some equations from special relativity are used in the derivations in this section, and are listed and explained in the appendix.

8.1 Per-event coalescence

Per-event coalescence within the Monte Carlo is fairly straightforward, as the coalescence condition only involves finding the momentum difference between the antiproton and antineutron in their center-of-momentum frame. In Herwig++, all quantities are given in the lab frame, and some calculations are needed in order find the corresponding COM frame values. One way to do so, is by making use of the Lorentz invariant Mandelstam variable s (A.14), which can be written out as

$$s = (\mathbf{p}_1 + \mathbf{p}_2)^2 = \mathbf{p}_1^2 + \mathbf{p}_2^2 + 2\mathbf{p}_1\mathbf{p}_2. \tag{8.1}$$

Inserting for $\mathbf{p}_1$ and $\mathbf{p}_2$ yields

$$s = E_1^2 + E_2^2 + 2E_1E_2 - \vec{p_1}^2 - \vec{p_2}^2 - 2\vec{p_1} \cdot \vec{p_2}, \tag{8.2}$$

or, using (A.4),

$$s = m_1^2 + m_2^2 + 2E_1E_2 - 2\vec{p}_1 \cdot \vec{p}_2. \tag{8.3}$$

E and $\vec{p}$ for the various particles are available in Herwig++, and s can thus be calculated using eq. (8.3).

Now, let $\vec{p}_{i,CM}$ be the momentum of particle i in the COM frame, and let $E_{i,CM}$ be the corresponding energy. The COM frame is characterized by

$$\vec{p}_{1,CM} = -\vec{p}_{2,CM} \equiv \vec{p}_{CM}. \tag{8.4}$$

Using (8.4), (8.2) becomes

$$s = E_{1,CM}^2 + E_{2,CM}^2 + 2E_{1,CM}E_{2,CM} = (E_{1,CM} + E_{2,CM})^2. \tag{8.5}$$

Inserting $E_{2,CM}^2 = m_2^2 + E_{1,CM}^2 - m_1^2$ and rewriting gives

$$\frac{s + m_1^2 - m_2^2}{2} = E_{1,CM}(E_{1,CM} + E_{2,CM}). \tag{8.6}$$

Using (8.5), we identify the bracket on the right hand side to be $\sqrt{s}$, giving

$$E_{1,CM} = \frac{s + m_1^2 - m_2^2}{2\sqrt{s}}. \tag{8.7}$$

This expression is Lorentz invariant, and we can thus find $E_{1,CM}$ by inserting s, as calculated using (8.3) in the lab frame. With $E_{1,CM}$ known, the momentum difference for the coalescence can now be calculated using

$$\Delta p = \|\vec{p}_{1,CM} - \vec{p}_{2,CM}\| = 2\|\vec{p}_{CM}\| = 2\sqrt{E_{1,CM}^2 - m_1^2}. \tag{8.8}$$

Any antiproton-antineutron pair with $\Delta p < p_0$ is accepted, and creates an antideuteron with energy $E_{\bar{d}} = E_{\bar{n}} + E_{\bar{p}}$. Pairs that do not fulfill this condition are rejected. The probability that a given antiproton/antineutron fulfills the coalescence condition with more than one antineutron/antiproton is negligible, but measures should in general be taken to avoid double counting.

8.2 Coalescence with energy spectra

8.2.1 Number densities

In order to find an expression for energy spectra, we begin by first deriving the standard expression for coalescence of number densities of the particles in momentum space. There are several ways to approach this problem, but aside from some numerical constant, the resulting equation is generally the same.

The condition for coalescence of an antiproton and an antineutron, is for the particles have a momentum difference, Δk, less than some maximum value, p_0. As stated before, this condition should be evaluated in the COM frame of the two particles. We want to find a relation that connects the particle densities (in momentum space) of the different species, and a COM frame will in this case not be well defined. The closest we can get is the COM frame of the average antiproton and antineutron momenta. Let us therefore begin by choosing a point in momentum space around which we search for antideuterons, and then find the average COM frame of the antinucleons that create these antideuterons. Let this point in momentum space be denoted $\vec{k}_{\bar{d}}$ in the lab frame.

In the lab frame, the coalescence should be strongly peaked around $\Delta\vec{k} = \vec{k}_{\bar{p}} - \vec{k}_{\bar{n}} \approx 0$, where $\vec{k}_{\bar{p}}$ and $\vec{k}_{\bar{n}}$ are the antiproton and antineutron momenta, respectively. Imposing momentum conservation, this gives

$$\vec{k}_{\bar{p}} \approx \vec{k}_{\bar{n}} \approx \frac{\vec{k}_{\bar{d}}}{2}. \tag{8.9}$$

Assuming that the distributions of antineutrons and antiprotons do not vary too much around $\vec{k}_{\bar{d}}/2$, this point should denote the average antiproton and antineutron momenta. Our "near COM" frame will thus be the frame where $\vec{k}_{\bar{p}} \approx \vec{k}_{\bar{n}} \approx 0$. The velocity of this frame can be found using eq. (A.5) with a mass $m \approx m_{\bar{p}} \approx m_{\bar{n}}$ and a momentum $p = k_{\bar{d}}/2$. Conveniently, using this velocity, along with $m_d \approx 2m_p \approx 2m_n$ and eq. (8.9) in (A.10), we find that the antideuteron momentum, $\vec{k}_{\bar{d}}$, is also approximately zero in this frame.

The condition $\Delta k < p_0$ can in this frame roughly be expressed as a condition that both particles are found within a sphere of radius p_0 around the origin[1]. The resulting antideuteron should then have a momentum equal to the sum of the antiproton and antineutron momenta, and thus be found within a sphere of radius $2p_0$. Let us now express this in terms of probabilities:

$$P(\bar{d} \text{ within } 2p_0) = P(\bar{p} \text{ within } p_0) \cdot P(\bar{n} \text{ within } p_0 \mid \bar{p} \text{ within } p_0). \tag{8.10}$$

We assume that the densities, and thus also the probabilities of finding an antiproton and an antineutron within the sphere, are uncorrelated. This gives us

$$P(\bar{d} \text{ within } 2p_0) = P(\bar{p} \text{ within } p_0) \cdot P(\bar{n} \text{ within } p_0). \tag{8.11}$$

Let us now evaluate these probabilities. The probability of finding a particle within the sphere should be equal to the integral of the particle density within the sphere:

$$P(\text{ particle } i \text{ within } p_0) = \left(\int d^3k \, \frac{dN_i}{d^3k} \, \Theta(p_0 - k) \right). \tag{8.12}$$

[1]It should optimally be a condition to find one particle within such a sphere around the other particle, but with the assumption that the particle densities do not vary too much in the area, it should be a good approximation

$\Theta(x)$ is here the Heaviside step function, and dN_i/d^3k is the number density of particle i in momentum space. It is here common to make the approximation that dN_i/d^3k is roughly constant within the sphere, so that (8.12) becomes

$$P(\text{ particle } i \text{ within } p_0) = \frac{4\pi p_0^3}{3}\left(\frac{dN_i}{d^3k}\right)_{\vec{k}=0}, \tag{8.13}$$

where the subscript denotes that the density is to be evaluated at the point $\vec{k}=0$ in this frame. Inserting this into (8.11), we then get

$$\left(\frac{dN_{\bar{d}}}{d^3k}\right)_{\vec{k}=0} = \frac{1}{8}\frac{4\pi p_0^3}{3}\left(\frac{dN_{\bar{p}}}{d^3k}\right)_{\vec{k}=0}\left(\frac{dN_{\bar{n}}}{d^3k}\right)_{\vec{k}=0}. \tag{8.14}$$

The factor 1/8 comes from the radius of the antideuteron sphere being $2p_0$. The above expression relates the particle densities in our "near COM"-frame. In order to be useful, however, it needs to relate the densities in the lab frame. In eq. (8.14), p_0 is just a constant, so all we need to do is to express the particle densities in this frame in terms of the corresponding particle densities in the lab frame.

In order to find the connections to the lab frame densities, it is necessary to look at how the derivative of a momentum transforms between different Lorentz frames. Using (A.10), we find

$$dk' = \frac{dk + v\ dE}{\sqrt{1-v^2}} = \frac{1}{\sqrt{1-v^2}}\left(1+\frac{vk}{E}\right)dk = \frac{1}{\sqrt{1-v^2}}\left(1+vw\right)dk, \tag{8.15}$$

where w is the velocity of a given particle measured in the current frame. Using the requirement that $k < p_0$ for our antinuclei and $k < 2p_0$ for the antideuteron, we see that w can at most reach a value of $w = p_0/(p_0^2+m_p^2)^{1/2} \sim 1/6$. $m_d \approx 2m_p \approx 2m_n$ can here be used to see that it holds for the case of the antideuteron. v is the relative velocity between our frame and the lab frame, and can have values from 0, up to close to 1. This means that the term vw in (8.15) has a maximal value of order 1/6, and one would expect the mean value to be a fair bit lower - possibly of order 1/10. If we neglect this term, we arrive at the simple expression

$$dk' = \gamma dk, \tag{8.16}$$

where γ, as usual, is defined by (A.6).

Let us now try applying a Lorentz transformation to a number density, $(dN/d^3k)_{\vec{p}=0}$, of a particle of mass m. For simplicity, we choose the coordinate system such that the transformation will be along the x-axis. The transformation will then only affect one of the components of the volume element d^3k, while the two others remain unchanged. The Lorentz transformation will also change the point $(\vec{p}=0)$ at which the density

is to be evaluated. Since $\vec{p} = 0$ in the original frame, (A.10) states that in the new frame,

$$\vec{p'} = (\gamma m v, 0, 0). \tag{8.17}$$

Using this and (8.15), we then get

$$\left(\frac{dN}{d^3k'}\right)_{\vec{p'}} = \frac{1}{\gamma}\left(\frac{dN}{d^3k}\right)_{\vec{p}=0}. \tag{8.18}$$

We can now use this to make the substitution

$$\left(\frac{dN}{d^3k}\right)_{\vec{k}=0} = \gamma\left(\frac{dN}{d^3k'}\right)_{\vec{p'}} \tag{8.19}$$

in (8.14). $\vec{p'}$ equals $\vec{k}_{\bar{p}}$, $\vec{k}_{\bar{n}}$, and $\vec{k}_{\bar{d}}$ for the antiproton, antineutron, and antideuteron, respectively. Dropping the prime in d^3k', we then arrive at the lab frame expression

$$\left(\frac{dN_{\bar{d}}}{d^3k}\right)_{\vec{k}_{\bar{d}}} = \frac{1}{8}\frac{4\pi p_0^3}{3}\gamma\left(\frac{dN_{\bar{p}}}{d^3k}\right)_{\vec{k}_{\bar{p}}=\vec{k}_{\bar{d}}/2}\left(\frac{dN_{\bar{n}}}{d^3k}\right)_{\vec{k}_{\bar{n}}=\vec{k}_{\bar{d}}/2}, \tag{8.20}$$

where, of course, all densities (dN_i/d^3k) and momenta $\vec{k}_i$ are measured in the lab frame.

Equation (8.20) tends to vary by some constant numerical factor in different articles, depending on how it was derived. Such a factor can, however, be absorbed by re-defining p_0. Many articles, such as the one by Bräuninger et. al [14] do not have the factor 1/8, which means that p_0 should be divided by a factor 2 when comparing to these articles.

8.2.2 Energy spectra

Now that we have an expression in terms of number densities, we can can find the coalescence expression for energy spectra. In order to find this expression, it is necessary to assume that the number densities are isotropic, such that

$$\left(\frac{dN}{d^3k}\right)_{\vec{k}} = \frac{1}{4\pi k^2}\left(\frac{dN}{dk}\right)_{k\equiv\|\vec{k}\|}. \tag{8.21}$$

Taking the derivative of (A.8) gives us $dT = dE$, and using $k \equiv |\vec{p}|$ in (A.4) gives $EdE = kdk$, thus

$$\left(\frac{dN}{d^3k}\right)_{\vec{k}} = \frac{1}{4\pi kE}\left(\frac{dN}{dT}\right)_{T=\sqrt{m^2+\vec{k}^2}-m}, \tag{8.22}$$

where T is the kinetic energy of the particles, as defined by (A.8). Inserting the above into (8.20) gives

$$\left(\frac{dN_{\bar{d}}}{dT}\right)_{T_{\bar{d}}} = \frac{1}{8}\frac{4\pi p_0^3}{3}\frac{4\pi k_{\bar{d}}E_{\bar{d}}}{(4\pi)^2 k_{\bar{n}}k_{\bar{p}}E_{\bar{n}}E_{\bar{p}}}\gamma\left(\frac{dN_{\bar{n}}}{dT}\right)_{T_{\bar{n}}=T_{\bar{d}}/2}\left(\frac{dN_{\bar{p}}}{dT}\right)_{T_{\bar{p}}=T_{\bar{d}}/2}. \tag{8.23}$$

The approximations we have made so far, $m_{\bar{p}} \approx m_{\bar{n}} \approx m_{\bar{d}}/2$ and (8.9), imply that $T_{\bar{n}} = T_{\bar{p}} = T_{\bar{d}}/2$. Using this, and replacing the γ-factor using (A.7), we get the expression for coalescence with energy spectra,

$$\begin{aligned}\left(\frac{dN_{\bar{d}}}{dT}\right)_{T_{\bar{d}}} &= \frac{p_0^3}{6}\frac{m_{\bar{d}}}{m_{\bar{n}}m_{\bar{p}}}\frac{1}{k_{\bar{d}}}\left(\frac{dN_{\bar{n}}}{dT}\right)_{T_{\bar{n}}=\frac{T_{\bar{d}}}{2}}\left(\frac{dN_{\bar{p}}}{dT}\right)_{T_{\bar{p}}=\frac{T_{\bar{d}}}{2}} \\ &= \frac{p_0^3}{6}\frac{m_{\bar{d}}}{m_{\bar{n}}m_{\bar{p}}}\frac{1}{\sqrt{T_{\bar{d}}^2 + 2m_{\bar{d}}T_{\bar{d}}}}\left(\frac{dN_{\bar{n}}}{dT}\right)_{T_{\bar{n}}=\frac{T_{\bar{d}}}{2}}\left(\frac{dN_{\bar{p}}}{dT}\right)_{T_{\bar{p}}=\frac{T_{\bar{d}}}{2}}.\end{aligned} \tag{8.24}$$

8.3 Finding p_0

The momentum difference p_0 must in both approaches be found by running simulations on processes for which we have experimental data, and adjusting p_0 such that the computational result matches the experiment. p_0 values for the energy spectrum approach can be extracted from a number of articles, but since many assumptions and approximations were made in the derivation of eq. (8.24), it is not given that the p_0 value for coalescence within the Monte Carlo should be the same. Coalescence within the Monte Carlo is still an uncommon approach, and no values of p_0 were available for this approach when this work was conducted. We therefore had to find this value ourselves through calibration against experimental data.

There is little data available that can be used for calibrating p_0. One of the few data sets that can be used, is the result for antideuteron production in e^+e^--collisions from the ALEPH data [48]. At the Z-resonance, each event should give rise to $(5.9 \pm 1.8 \pm 0.5) \times 10^{-6}$ antideuterons in the momentum range $0.62\,\text{GeV} < k_{\bar{d}}$, $k_{\bar{d}} < 1.03\,\text{GeV}$. The detector had an angular acceptance range $|\cos\theta| < 0.95$, something which was also taken into account. We want to compare the antideuteron spectra from the two different approaches, and in order to do so consistently, the p_0 value for both approaches should be calibrated against the same data. Instead of relying on the p_0 value used in other papers for the energy spectrum approach, we therefore calibrated this p_0 value against the ALEPH data as well.

Our calculations yielded a value of $p_0 = 110\,\text{MeV}$ for the case where coalescence was performed within the Monte Carlo, and $p_0 = 126\,\text{MeV}$ for coalescence applied to antiproton and antineutron spectra. We will be comparing our results to those of Bräuninger et. al [14], and have to keep in mind that the definition of p_0 varies between different papers. We obtain the definition by Bräuninger et. al by absorbing a factor 1/8 in p_0^3; in other words by multiplying our p_0 by a factor 1/2. Our calibrated p_0 value for the energy spectrum approach thus corresponds to $p_0 = 63\,\text{MeV}$ in their definition.

Bräuninger et. al use a p_0 value of 79 MeV (in their definition of p_0). We note that there is a significant uncertainty in what is the "correct" value of p_0. A wide

range of possible values has been proposed; [22] suggests a window between 66 MeV and 105 MeV (in the definition of Bräuninger et. al), and mentions that values as low as 58 MeV have been proposed by earlier papers. For us, it is most important to have p_0 values that are consistently calibrated for the two approaches. The result for a different value of p_0 can be obtained by multiplying our result by a factor $(p_0'/p_0)^3$, where p_0' is the new value. For coalescence within the Monte Carlo, this is only an approximation, while for coalescence of energy spectra, this is an exact relation.

9 Computational results: Source spectra

The results presented in this section were generated using 10^7 events, and most results are presented in terms of the scaled kinetic energy $x \equiv T/M_{DM}$, where M_{DM} is the dark matter mass. In order to generate antiproton, antineutron, and antideuteron spectra, these particles were binned in 100 logarithmic bins in the kinetic energy range $x = 10^{-10} - 10^0$ (10 bins per order of magnitude).

For simplicity, we will from now on mostly refer to results from calculations where coalescence was applied per-event within the Monte Carlo as 'Monte Carlo' results, and results from calculations where coalescence was applied to the average antiproton and antineutron energy spectra (using (8.24)) as 'isotropic' results (due to the assumption of isotropy required in the derivation of (8.24)). We correspondingly refer to the two approaches as the Monte Carlo approach and the isotropic approach.

9.1 The antideuteron source spectra

The primary goal of this thesis is to investigate the significant difference in magnitude between the antideuteron source spectra from the $b\bar{b}$ and W^+W^- channels presented by Bräuninger et. al [14]. By source spectra, we here refer to the energy spectra of the particles immediately after production; in other words: The spectra before propagation through the Galaxy. The antideuteron source spectra from the calculations by Bräuninger et. al are shown in figure 9.1. We note that Bräuninger et. al used the minimal dark matter (MDM) model, rather than the MSSM in their calculations. The MDM model is a simple extension of the standard model, whose sole purpose is to introduce a dark matter particle candidate. This model does not have the problems with precise cancellation of terms at high dark matter masses, and Bräuninger et. al were therefore able to generate antideuteron spectra for dark matter masses of several TeV.

We begin by comparing our results for the isotropic case to those of Bräuninger et. al. The antideuteron source spectra calculated by Bräuninger et. al are shown in figure 9.1, while our corresponding isotropic result at 1 TeV is plotted in figure 9.2. Since our calculations are restricted to dark matter masses below a couple of TeV, the only mass we can compare for (and thus the only case plotted in figure 9.2) is 1 TeV.

We immediately notice that there appears to be an approximate factor 20 discrepancy between our and their results[2]. Assuming that our antiproton and antineutron spectra are the same, a factor 2 can be accounted for by our lower p_0 value, but the spectra still differ by a factor 10. We also note that the shape of the spectra differ somewhat for low energies, especially in the $b\bar{b}$ case. Some differences in shape and magnitude can be expected since Bräuninger et. al used PYTHIA rather than Herwig++ as event generator, but a factor 10 difference should not come from this.

Bräuninger et. al claim that their antiproton source spectra (before coalescence) agree with those from an earlier study by Donato et. al [23] (aside from a factor 2 due to setting the antineutron not to decay). A good test would therefore be to compare our antiproton spectra to those by Donato et. al as well. We note that Donato et. al do not provide an antiproton spectrum for the W^+W^- channel, but according to [14], the antiproton spectrum from the ZZ channel should be similar to that from W^+W^- (this can e.g. be seen in the plots in [19]). Similarly, the spectrum from any quark channel should also be similar to that from $b\bar{b}$. We will therefore compare the spectrum from the W^+W^- channel to that from the ZZ channel by Donato et. al.

We note that the spectra of antiprotons and antineutrons are approximately equal. We do not include a plot of the antineutron spectrum here, but the total number of antineutrons and antiprotons per event are plotted in figure 9.10. Antineutrons would under normal circumstances decay into antiprotons, but since we specifically set the antineutron not to decay, our antiproton spectrum will be a factor 2 too small. Like for Bräuninger et. al, our antiproton spectra should therefore be multiplied by a factor 2 for this comparison.

The antiproton spectra from Donato et. al [23] are shown in figure 9.3, while the spectra from our calculations, with and without the factor 2, are shown in figure 9.4. We see that our spectra agree fairly well with those by Donato et. al after taking the decay of antineutrons into account. We note minor differences in the shapes, but this can be expected due to different Monte Carlo generators. Some differences may also be expected when comparing the spectrum from W^+W^- to a spectrum from ZZ.

If the antiproton source spectra of Bräuninger et. al truly agree with those by Donato et. al [23], they should consequently agree with ours too. Given that this is the case, the factor 10 difference must be due to an error in either their or our calculations of the antideuteron spectra. We checked for such an error in our calculations by manually reading out the data for the antiproton and antineutron spectra, and calculating the corresponding antideuteron spectrum by hand using eq. (8.24) for several data points. The points did in all cases agree with the antideuteron spectra plotted in figure 9.2, and the likely explanation to the discrepancy is therefore that the spectra of Bräuninger et. al are off by a factor 10.

[2]For the W^+W^- case, the discrepancy is approximately a factor 20 for the entire plotted energy range, while in $b\bar{b}$ case, the discrepancy is approximately a factor 20 for high energies, and somewhat higher for lower energies.

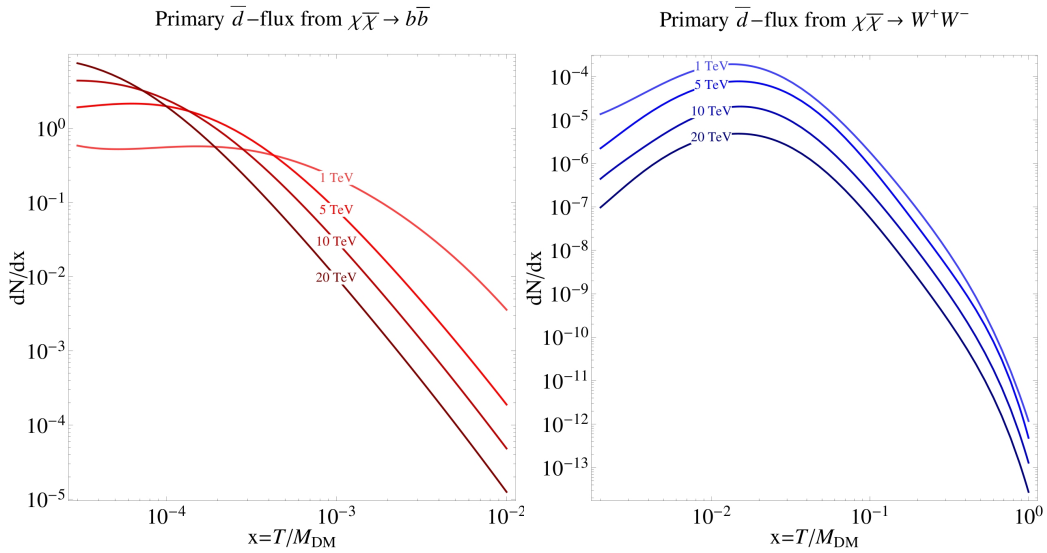

Figure 9.1: Antideuteron source spectra per event for dark matter annihilations into $b\bar{b}$ (left) and W^+W^- (right), as calculated by Bräuninger et. al [14].

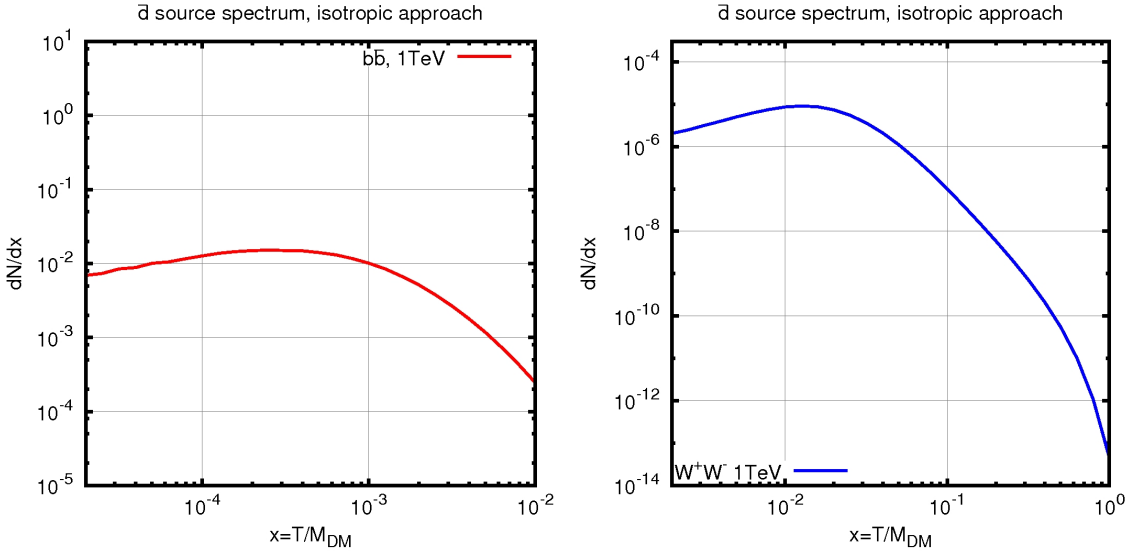

Figure 9.2: Antideuteron source spectra per event for dark matter annihilations into $b\bar{b}$ (left) and W^+W^- (right) from our calculations.

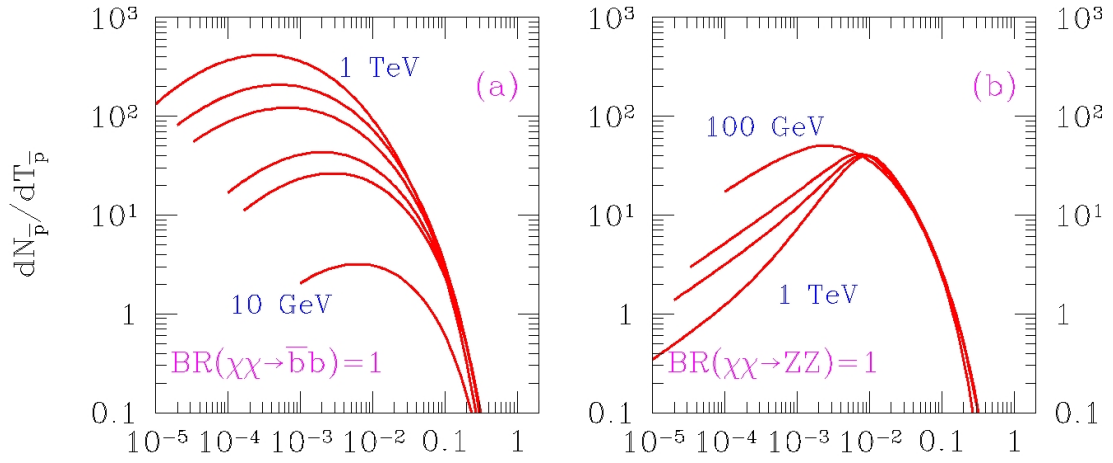

Figure 9.3: Antiproton spectra per event for dark matter annihilations into $b\bar{b}$ (left) and ZZ (right), as calculated by Donato et. al [23]. Note that the quantity on the vertical axes is (likely) supposed to be dN/dx rather than dN/dT.

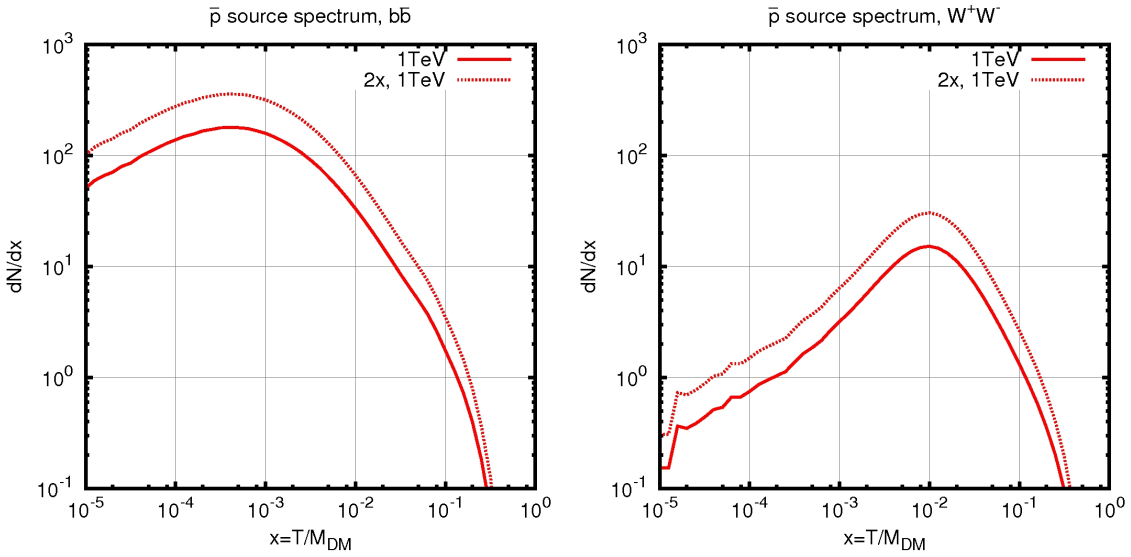

Figure 9.4: Antiproton spectra per event for dark matter annihilations into $b\bar{b}$ (left) and W^+W^- (right) from our calculations. Solid lines show the results from the calculations, while dotted lines show the spectrum multiplied by a factor 2, in order to account for antineutron decays. The fluctuations for low energies in the spectrum from W^+W^- are due to insufficient data (too few particles in the energy bins).

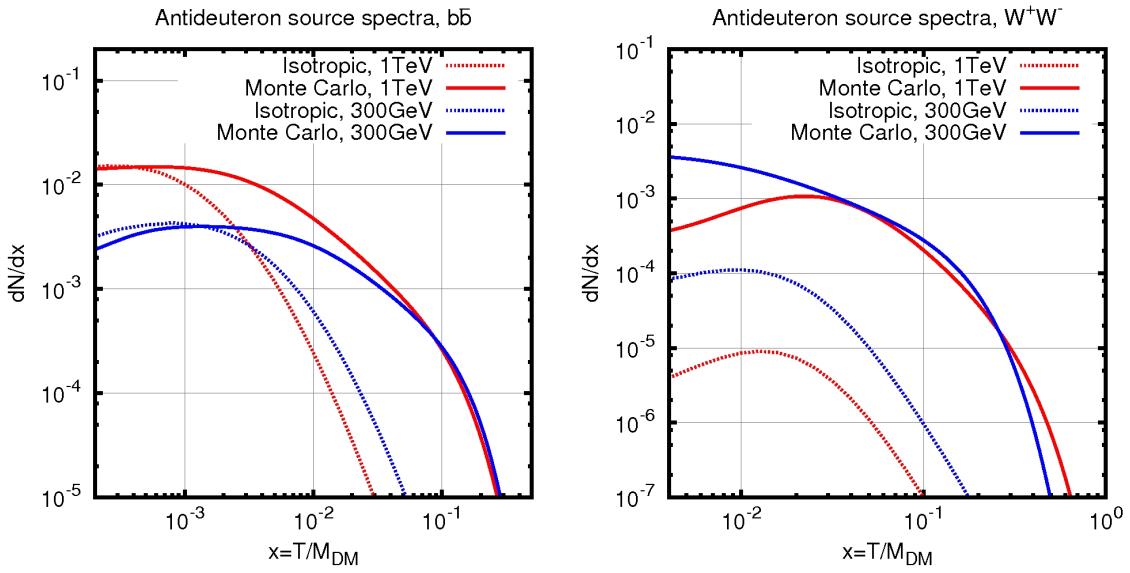

Figure 9.5: Antideuteron source spectra per event for dark matter annihilations into $b\bar{b}$ (left) and W^+W^- (right). The solid lines show the spectra for per-event coalescence within the Monte Carlo, while the dotted lines show the spectra for coalescence of the average antiproton and antineutron spectra. Red lines show the result for a dark matter mass of 1 TeV, while blue lines show the result at 300 GeV.

While the results differ by an overall factor, we see that our results agree with those by Bräuninger et. al in that there is a significant difference in the magnitude of the antideuteron spectra from $b\bar{b}$ and W^+W^-. The difference appears to be slightly lower in our calculations (due to the different shape of the spectrum in the $b\bar{b}$ case), but the ratio between the peaks are still of order 10^3. What we want to investigate in this thesis, is whether or not this difference is affected by how coalescence is performed; i.e. if the isotropic or the Monte Carlo approach is used.

The antideuteron fluxes from the isotropic and Monte Carlo approaches are plotted for dark matter masses of 300GeV and 1TeV in figure 9.5. We see that in the $b\bar{b}$ case, the magnitude of the spectrum seems to be roughly the same for the two approaches. The spectra are, however, shifted towards higher energies, and there are some differences in the shapes of the spectra. For the W^+W^- case, there is a significant difference in the magnitude of the antideuteron spectrum between the two approaches. For 1 TeV, the difference is of order 10^2, while it appears to be a factor ~ 3 smaller for 300 GeV. The shapes of the spectra also differ somewhat between the two approaches, in particular for the 300 GeV case.

It is clear that when using the more correct Monte Carlo approach, the difference in magnitude between the $b\bar{b}$ and W^+W^- antideuteron spectra becomes much smaller

than in the isotropic approach. Another interesting feature is that this difference appears to depend on the dark matter mass. Both of these results will be investigated in more detail in section 9.2.

During the time in which this work was conducted, the difference in antideuteron spectra between the Monte Carlo and isotropic approaches was independently found by Kadastik et. al [32]. Before proceeding in analyzing the data, we will compare our results to their findings. We note that Kadastik et. al (like Bräuninger et. al) used the MDM model to introduce a dark matter candidate, and used PYTHIA rather than Herwig++ as event generator. They have the same definition of p_0 as us, and use a value of $p_0 = 160\,\text{MeV}$ for both the isotropic and Monte Carlo approach. Their p_0 value for the Monte Carlo approach is supposedly calibrated against the ALPEPH data, while the value for the isotropic approach has not been separately calibrated. We can only speculate why their p_0 value is higher than ours, but it can likely be attributed to the use of different Monte Carlo event generators.

The source spectra from the calculations by Kadastik et. al are plotted in figure 9.7. They plot their spectra in terms of $x\,dN/dx$, and our spectra are plotted similarly in figure 9.6. We note that figure 9.7 shows the result for annihilations into light quarks (labeled $q\bar{q}$) rather than $b\bar{b}$. As discussed earlier (and as can be seen in the other plots in their article), the spectrum from $b\bar{b}$ is similar to the spectra from other quarks. We also note that while we plot results for both approaches, Kadastik et. al only plot the source spectra from the Monte Carlo approach.

Comparing the results, we see that our spectra agree quite well for the W^+W^- case, while there seems to be a factor ~ 3 discrepancy in the $b\bar{b}$ case. Our curves are in the Monte Carlo case fitted to the data points with a factor ~ 1.5 uncertainty. This uncertainty may account for some of the discrepancy, as well as for some of the differences in the shapes of the curves. We also keep in mind that Kadastik et. al use a significantly higher value of p_0, something which alone could account for such discrepancy. The difference in discrepancy between the W^+W^- and the quark case could either be due to differences in the Monte Carlo generators, or possibly due to differences in the p_0-dependence of the different annihilation channels. Since we used the same program for calculating the spectra for both the W^+W^- and $b\bar{b}$ case, it is highly unlikely that this difference is due to an error on our side.

9.2 Analysis of the spectra

We found that there is a significant discrepancy in magnitude between the spectra from the Monte Carlo and isotropic approaches. We also found that this discrepancy appears to depend on the dark matter mass in the W^+W^- case. In order to investigate the dependence of the antideuteron spectra on the dark matter mass, we plotted the total number of antideuterons produced against the dark matter mass for the two approaches, as seen in figure 9.8. The corresponding plot by Kadastik et. al can

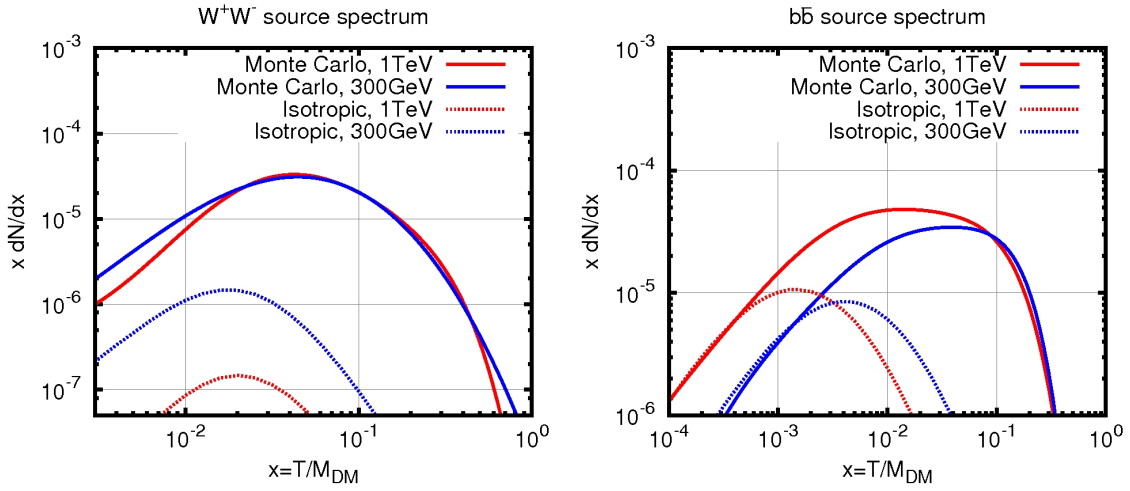

Figure 9.6: Antideuteron source spectra per event for dark matter annihilations into W^+W^- (left) and $b\bar{b}$ (right) from our calculations. The solid lines show the spectra for per-event coalescence within the Monte Carlo, while the dotted lines show the spectra for coalescence of the average antiproton and antineutron spectra. Red lines show the result for a dark matter mass of 1 TeV, while blue lines show the result at 300 GeV.

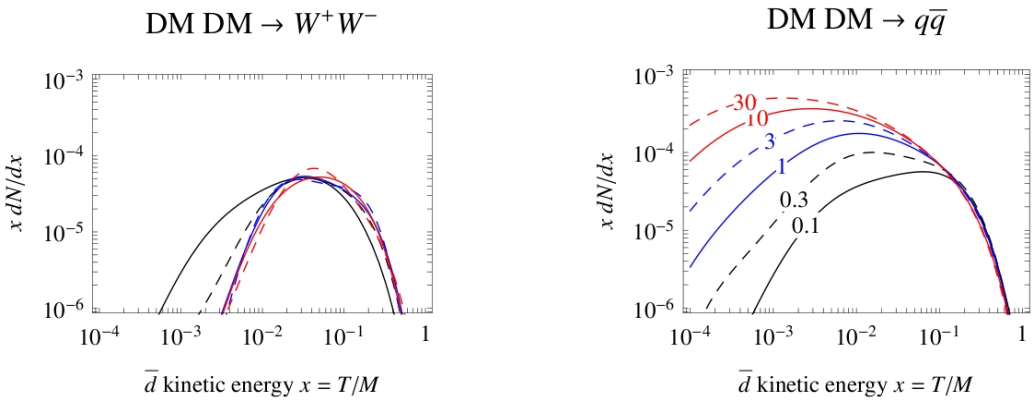

Figure 9.7: Antideuteron source spectra per event for dark matter annihilations into W^+W^- (left) and $q\bar{q}$ (right), as calculated by Kadastik et. al [32]. All results are from the Monte Carlo approach. Results are shown for dark matter masses of 0.1, 1, 10 TeV (black, blue, red solid lines) and 0.3, 3, 30 TeV (black, blue, red dashed lines).

be seen in figure 9.9. Comparing the figures, we find that the shapes of the graphs agree very well. We note some differences in the overall magnitudes of order $\lesssim 2$. We see that the factor ~ 3 difference we had in the spectrum from the $b\bar{b}$ channel is not reflected in the total number of antideuterons produced (though some difference is still present). This suggests that our calculation produced a wider spectrum (and thus a lower peak) than that of Kadastik et. al. This again points to the use of different event generators as the source of the discrepancies.

Analyzing the results, we again see a significant discrepancy in the overall antideuteron yield between the Monte Carlo and isotropic approaches, and we also see that there is a clear difference in the dark matter mass dependence of the antideuteron yield between the two approaches. For the W^+W^- case, the difference in mass dependence is very large; the ratio of the number of antideuterons produced in the two approaches changes by a factor 10^2 when increasing the dark matter mass from 100 GeV to 1 TeV. There is also some difference in the mass dependence for the $b\bar{b}$ case, but it is far less significant. Two major questions arise from these observations:

- Why the overall difference in antideuteron yield between the two approaches?
- Why is there a significant difference in the mass dependence in the W^+W^- case, while only a minor difference in the $b\bar{b}$ case?

9.2.1 The differences in mass dependence

The two questions are interrelated, and we begin by investigating the difference in the DM mass dependence between the annihilation channels. Equation (8.24) can be expressed in terms of the scaled kinetic energy, x:

$$\left(\frac{dN_{\bar{d}}}{dx}\right)_{x_{\bar{d}}} = \frac{p_0^3}{6}\frac{m_{\bar{d}}}{M_{DM}^2 m_{\bar{n}} m_{\bar{p}}}\frac{1}{\sqrt{x_{\bar{d}}^2 + 2m_{\bar{d}}x_{\bar{d}}/M_{DM}}}\left(\frac{dN_{\bar{n}}}{dx}\right)_{x_{\bar{n}}=\frac{x_{\bar{d}}}{2}}\left(\frac{dN_{\bar{p}}}{dx}\right)_{x_{\bar{p}}=\frac{x_{\bar{d}}}{2}}. \quad (9.1)$$

For large dark matter masses, M_{DM}, we would therefore expect the total number of antideuterons produced to be suppressed as $1/M_{DM}^2$. From figure 9.8 we see that this is the case for W^+W^-, but that it does not hold for $b\bar{b}$. The $1/M_{DM}^2$ suppression can only be expected if the number of antiprotons and antineutrons produced does not depend on the dark matter mass. We investigate this by plotting the average total numbers of antiprotons and antineutrons produced per event, as seen in figure 9.10. We see that the antinucleon yields are indeed constant in the W^+W^- case, but that they increase fast enough in the $b\bar{b}$ case to overcome the $1/M_{DM}^2$ suppression in eq. (9.1).

The difference between the two cases here is not entirely physical. The quarks and the gauge bosons are actually treated differently by Herwig++. When Herwig++ reads the input from MadGraph, it treats the gauge bosons as on-shell particles; it

does not know that they are merely intermediate states in a larger process. Quarks, on the other hand, cannot exist as free particles, and when given as input, they must always be virtual, intermediate particles. Treating the gauge bosons as on-shell is a good approximation at low energies, but is problematic at high energies. The problem when going to high energies, is that the gauge bosons are simply Lorentz boosted, and decay into the same number of final state particles as they would at low energies. An on-shell particle must always decay into particles where the total mass does not exceed the mass of the initial particle. Virtual particles, on the other hand, can decay into a group of particles with a higher total mass than the initial particle. This is exactly what we see in figure 9.10: Quarks, which are being treated as virtual particles, produce more final state particles at high energies, while the gauge bosons, which are being treated as on-shell particles, always produce the same number of final state particles.

9.2.2 The overall antideuteron yield

We continue our discussion by investigating the difference in the overall antideuteron yield between the two approaches. The source of this discrepancy is suggested in our naming of one of the coalescence approaches: Isotropy. In deriving equation (8.24), we had to assume that the momentum distributions of antiprotons and antineutrons were uncorrelated and isotropic. This, however, is not the case. Rather than being isotropically distributed, the final state particles from the neutralino annihilation events come out in confined jets. The momenta of the final state particles within each jet are more closely aligned than they would be in an isotropic distribution, and the probability of finding an antiproton-antineutron pair with a momentum difference less than p_0 is thus significantly higher than in the isotropic case.

To illustrate this effect, figure 9.11 shows the distribution of the angles between the momenta of the final state antiprotons and antineutrons. These distributions are of the internal angles for all possible antiproton-antineutron pairs, and should not be mistaken for the angles from the beam axis, i.e. the movement axis of the incident dark matter particles. We see that the distributions are peaked for angles near 0 and π, which indicates that the antiprotons and antineutrons are produced in back-to-back jets. We also see that the jet effect is much stronger in the W^+W^- case than for $b\bar{b}$, and that the jet effect for W^+W^- is considerably stronger for a dark matter mass of 1 TeV than for 300 GeV. There are two effects at play here. One of them is a QCD jet effect, while the other is related to special relativity, and comes back to the on-shell treatment of the gauge bosons.

For the $b\bar{b}$ case, only the QCD effect is of importance. The details of how these jets are formed is an advanced topic of QCD, and will not be discussed in detail here. The physical principle behind the jets is an angular ordering mechanism. The two particles produced in the tree level annihilation process move out back-to-back, and

decay in QCD cascades. For each step (each decay or particle emission) in a QCD cascade, the angles between the momenta of the produced particles decrease. This effect accumulates through the cascade, giving rise to confined particle jets. The jet effect is in this case somewhat suppressed by the fact that the quarks carry color, and particles from the two different jets will therefore have to combine in order to produce colorless final states.

For the W^+W^- case, the two particles do not carry color, and only particles within each jet will have to combine in order to produce colorless final states. This is, however, not the main mechanism behind the strong jet confinement in the W^+W^- case. The explanation for this strong confinement brings us back to the on-shell treatment of the gauge bosons. As already mentioned, an increase in dark matter mass will in the W^+W^- case correspond to a Lorentz boost of the final state particles[3]. This Lorentz boost will in itself produce a jet effect.

Consider an annihilation event that produces a W^+W^- pair, where the two gauge bosons move back-to-back along the x-axis with a velocity V. Consider now a final state particle being created with a velocity $v = \sqrt{v_x^2 + v_y^2}$ in the rest frame of the W-boson moving in the positive x-direction (unprimed coordinates). v_x and v_y are here the velocity components along the x and y axes. The angle between the x-axis and the movement direction of the particle is in this frame given by

$$\cos(\theta) = \frac{v_x}{\sqrt{v_x^2 + v_y^2}}. \tag{9.2}$$

The Lorentz transformations to the lab frame (primed coordinates) of the velocity components of are given by eq. (A.11) and (A.12). We can now calculate the angle between the movement direction of the particle and the x-axis in the lab frame:

$$\cos(\theta') = \frac{v'_x}{\sqrt{v'^2_x + v'^2_y}} = \frac{v_x + V}{\sqrt{(v_x + V)^2 + v_y^2(1 - V^2)}}. \tag{9.3}$$

If $V = 0$, the angles are the same in both frames. We see, however, that for $V \to c = 1$, $\cos(\theta') \to 1$, or $\theta' \to 0$. In other words: As the velocities of the gauge bosons increase, the angular distribution of the decay products (in the lab frame) becomes narrower. This effect is the source of the extra strong jet confinement seen for the W^+W^- case in figure 9.11, and explains why the confinement is significantly stronger at 1 TeV than it is at 300 GeV. We note that the stronger angular confinement from special relativity does not affect coalescence, as the coalescence prescription is applied in the center-of-momentum frame of the antiproton and antineutron. If it did affect coalescence, we should have seen an increase in the number antideuterons produced with higher dark matter masses, but as seen in figure 9.8, the number remains roughly constant.

[3]Some change in this behaviour can, however, be expected in the regime where energies are low enough for particles from different jets to interact with each other.

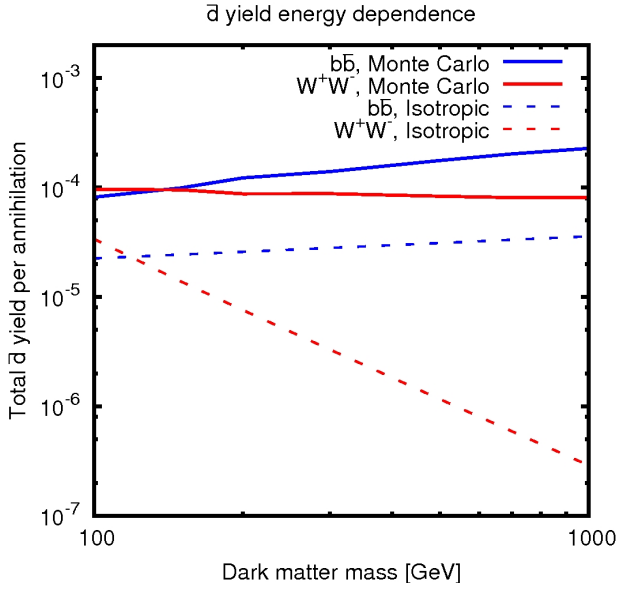

Figure 9.8: Average total antideuteron yield per annihilation event as function of the dark matter mass. The solid lines show the results from calculations where the coalescence was performed within the Monte Carlo simulation, whereas the dashed lines show the results where the coalescence prescription was applied to the average antiproton and antineutron energy spectra.

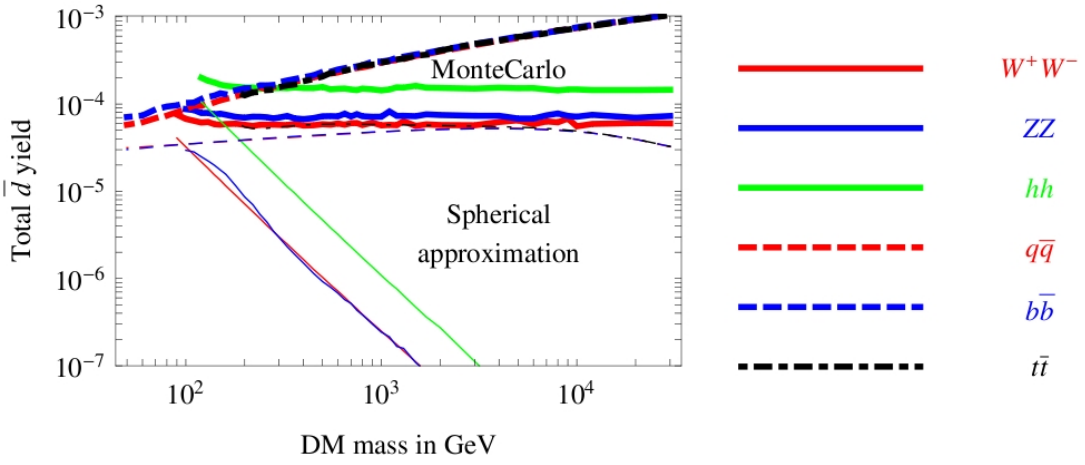

Figure 9.9: Average total antideuteron yield per annihilation event as function of the dark matter mass, as calculated by Kadastik et. al [32]. The annihilation channels are listed on the right. The thin lines correspond to the isotropic approach (labeled 'Spherical approximation'), while the thicker lines correspond to the Monte Carlo approach.

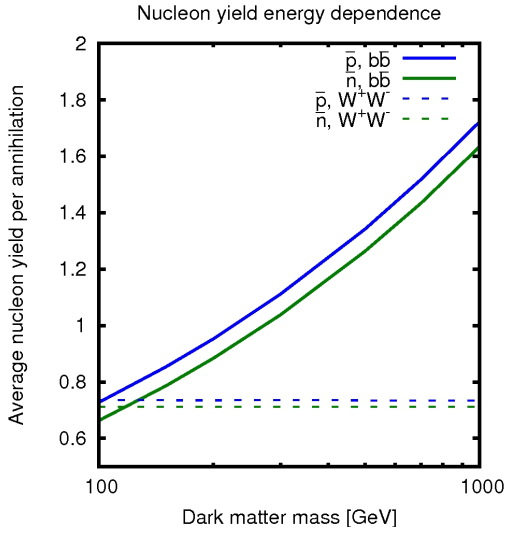

Figure 9.10: Average total antiproton and antineutron yields per annihilation event as function of the dark matter mass. Green indicates antineutrons, while blue indicates antiprotons. The solid lines show the results for the $b\bar{b}$ case, while the dashed lines show the results for the W^+W^- case.

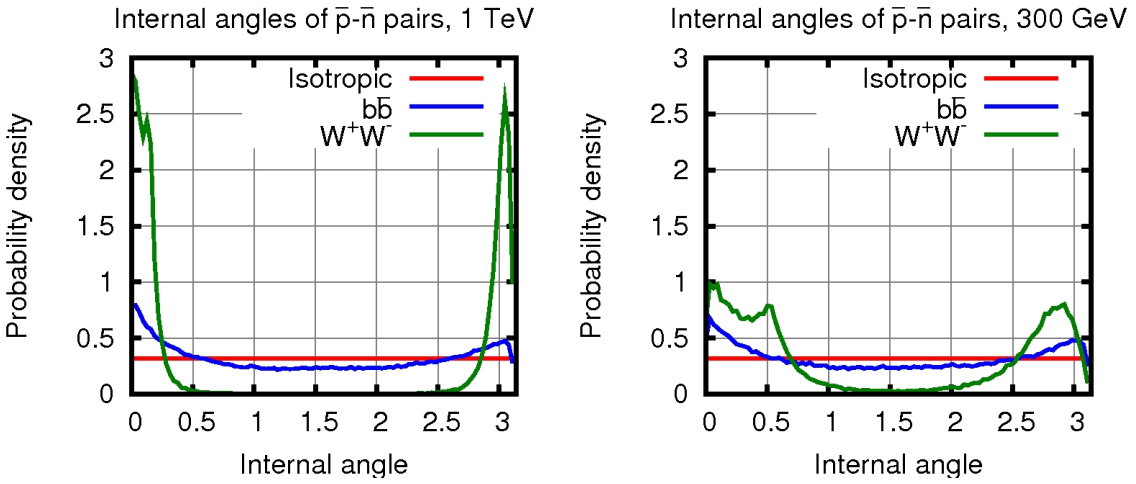

Figure 9.11: Distribution of the angles between the momenta of antiprotons and antineutrons. For each possible antiproton-antineutron pair, the angle between the momenta was calculated in the lab frame. These angles were averaged over all pairs, over 10^5 events. The blue and green lines show the actual Monte Carlo result for $b\bar{b}$ and W^+W^-, while the red lines show the expected result for the case of isotropic distributions.

10 Higher order processes

Since the difference between the coalescence implementations was investigated by Kadastik et. al during the work on this thesis, we decided to also look for other factors that may influence the antideuteron spectrum. Earlier papers on the subject have only considered tree level processes, and we therefore decided to investigate the corrections from higher order processes.

We are here more interested in the branching ratios between the processes than in the antideuteron spectra from the individual processes. As mentioned in section 7.2, the branching ratios between different annihilation channels are very much model dependent, while the antideuteron spectra from the different channels are not. The results in this section are therefore specifically related to the MSSM.

We calculated the low velocity annihilation cross sections (corresponding to kinetic energies $T \sim$ few GeV $\ll M_{DM}$) for $\tilde{\chi}_1^0\tilde{\chi}_1^0 \to W^+W^-$, and for the higher level processes in which one and two extra Z-bosons are emitted. MadGraph was unable to calculate cross sections for processes with a higher number of gauge bosons in the final state. The calculations were performed for several different neutralino masses in the range 100 GeV to 2 TeV [4]. Using these cross sections, we calculated the branching ratios with the W^+W^- cross section as benchmark. The branching ratios are, in other words, normalized such that W^+W^- has a constant branching ratio of 1. The results from these calculations are plotted in figure 10.1.

We note that we are not looking to give a complete view of the different annihilation channels, but rather to get a phenomenological indication on the influence of higher order processes. We therefore do not consider the branching ratios between quarks and gauge bosons, or calculate the cross sections for other processes of the same orders.

From figure 10.1, we see that the contribution from higher order processes is negligible for low neutralino masses. The contributions do, however, increase rapidly with increasing masses. For 2 TeV, the branching ratio for W^+W^-Z is roughly 10% of that for the tree level process. We see that the process involving 2 Z-bosons is more strongly suppressed for low neutralino masses than the single-Z-boson process, but that the contribution appears to increase faster with increasing masses than for W^+W^-Z. Due to the unreliability of the spectrum generators for high masses, we do not calculate results for neutralino masses above 2 TeV. Note that the bump in the graphs at roughly 1100 GeV is not due to statistical uncertainty, but more likely due to the MSSM calculation becoming unreliable for high masses.

Extrapolating our results, we would expect the contribution from higher order processes to become significant for a neutralino mass in the mid-TeV range. The emission of additional Z-bosons are, of course, not the only possible higher order processes, and when performing calculations in the TeV range, the contributions from

[4] Annihilations into W^+W^-Z and W^+W^-ZZ are only possible when the combined mass of the two neutralinos is higher than combined the mass of the 3 and 4 gauge bosons.

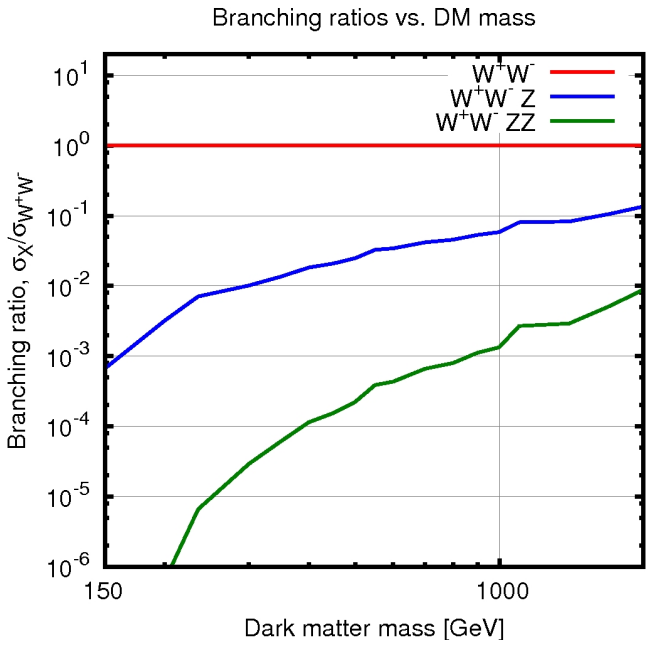

Figure 10.1: Branching ratios for various annihilation channels as function of the dark matter (neutralino) mass. The red line shows the benchmark branching ratio for the tree level process $\tilde{\chi}_1^0\tilde{\chi}_1^0 \to W^+W^-$. The blue and green lines show the branching ratios for the higher order processes $\tilde{\chi}_1^0\tilde{\chi}_1^0 \to W^+W^-Z$ and $\tilde{\chi}_1^0\tilde{\chi}_1^0 \to W^+W^-ZZ$, respectively.

a number of processes should be considered. In calculations for neutralino masses below 1 TeV, however, the contributions from higher order processes can be neglected. Since the contribution from the higher order processes is so low in the mass range available to our calculations, we do not calculate the antideuteron spectra from these processes.

We emphasize again that this result is specific to the MSSM. Similar results may be expected in other models, but the mass range in which the higher order corrections become important will likely vary. For papers like those of Bräuninger et. al and Kadastik et. al, where annihilation spectra are being calculated for dark matter masses up to 30 TeV, the contributions from higher order processes should certainly be investigated and taken into account.

11 Propagation through the Galaxy

Using Monte Carlo simulations, we obtained the average particle energy spectra from dark matter annihilation events. In order to detect dark matter indirectly, however, we need to calculate the fluxes and energy spectra we would expect to measure in chosen particle channels near Earth.

Measurable signals from dark matter annihilations would be expected to originate mainly from annihilations within our own galaxy. In section 1.2, we presented some common models for dark matter distributions in galaxies. Using these profiles, along with the data from the Monte Carlo simulations, we can find the resulting spectrum and production rate of antideuterons at any given point in the Galaxy. What we now need to know, is how these particles propagate in the Galaxy, from the point where the annihilation took place, to Earth, where the total flux can be measured.

There are several physical phenomena in the Galaxy that will influence the propagation of cosmic ray particles. Since we are dealing with charged particles (antideuterons), magnetic fields are of particular importance. We will discuss this in more detail below, and introduce one of the most commonly used propagation models. Before doing so, however, we have a closer look at what we know about the Galaxy.

11.1 The Milky Way

The Milky Way is a spiral galaxy, and our solar system is located approximately 8 kpc from the Galactic center, close to the arm structure known as the Orion-Cygnus arm. The Galaxy consists of several different regions, of varying importance to cosmic ray propagation. We will briefly discuss some of these regions below. Most of the numerical values in this section are taken from [17].

The Galactic disk: This is arguably the most important important structure in the Galaxy, and contains many of the stars, as well as most of the gas and dust of the Galaxy. It has a radius of approximately 25 kpc and a thickness of about 350 pc (for the region referred to as the thin disk). As already mentioned, the Milky Way is a spiral galaxy, which implies that the Galactic disk has a spiral arm structure. The exact spiral structure is not fully known, but a four-arm logarithmic spiral model is a likely candidate [25].

For the discussion of cosmic ray propagation, there are a number of processes taking place in the disk that could influence the cosmic ray spectra. Examples of such processes are annihilations on interstellar matter, energy loss processes related to scattering on interstellar matter, and reacceleration due to plasma shock waves or magnetic irregularities [5]. Moreover, as briefly discussed in [39], an outflow of matter

[5]These reacceleration processes are known as first and second order Fermi acceleration. See for example [46] for more information.

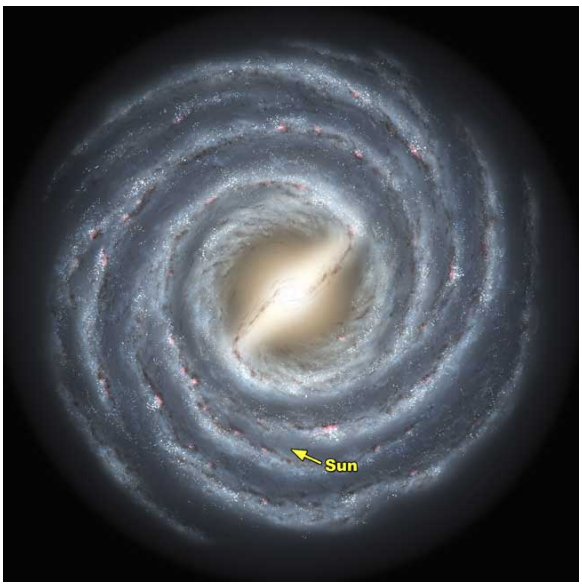

Figure 11.1: Illustration of the Milky Way. The arrow shows the position of the Sun. Credit: NASA JPL.

from the Galactic disk (a galactic wind) is necessary for the disk to be stable. Such winds have been observed in other galaxies, and will contribute to push low energy particles away from the Galactic disk.

Stellar halo: The stellar halo is a spherically symmetric distribution of old stars around the Galactic center. The halo does not rotate around the Galactic center like the disk, and the stars in the halo generally have high velocities compared to those in the disk. Many of these halo stars are also gravitationally bound together in globular clusters. The radius of the halo is not very well defined, but a value of about 50 kpc seems appropriate. The stellar halo is not of significant importance for cosmic ray propagation.

Galactic bulge: In the center of the Galaxy, we find the Galactic bulge, which is a region with a higher vertical extension than the Galactic disk. It has a half-light radius (radius of a sphere from which half of the light is emitted) of about 0.7 kpc. The bulge contains a large number of stars, whose motions can be described as an intermediate between a purely rotating system (like the Galactic disk) and a system that is supported by its velocity dispersion (like the stellar halo) [41]. The bulge was originally thought to be fully spheroidal, but more recent studies strongly indicate that it contains an elongated bar structure with a radius (half-length) of approximately 4.4 kpc (illustrated in figure 11.1) [17].

In terms of cosmic ray propagation, the bulge is often disregarded, and treated the same way as the Galactic disk.

Dark matter halo: As already discussed, there is significant evidence that the Galaxy might have a spherically symmetric halo of dark matter. The distribution of dark matter is crucial for finding the dark matter annihilation rates in different parts of the Galaxy, and possible distribution models were discussed in section 1.2. Since (WIMP) dark matter interacts very weakly with ordinary matter, the dark matter halo has no influence on the propagation of cosmic rays after their production.

Galactic magnetic field: It is well established that the Galaxy has a magnetic field. In the disk, this field can be observed in several ways, for example through Faraday rotation[6]. Outside the disk, there are fewer means to observe this field, but observations such as synchrotron radiation from far above the disk indicate that the magnetic field stretches far beyond the disk [18]. One often refers to this extended magnetic field region as the magnetic halo of the Galaxy.

The magnetic field is often divided into two main components: One "regular" component which follows the spiral structure of the disk, and one component which is inhomogeneous and highly turbulent. The inhomogeneous component is of particular importance to cosmic ray propagation, as it effectively leads to a random walk behaviour for low energy particles. Cosmic rays from WIMP annihilations within the Galaxy are considered low energy particles in this respect. The random walk of the particles in this magnetic field can be described by a diffusion equation. Unfortunately, the details of the magnetic field are poorly known, so one has to resort to simple models for the diffusion coefficient [40].

The region where this diffusion takes place is often modeled as a cylinder with a radius equal to that of the disk. The height of the region is still a matter of discussion, but a half-height of $\sim 4\,\mathrm{kpc}$ is, according to many measurements, a reasonable value [40].

[6]Faraday rotation is a rotation of the polarization of light due to a magnetic field in the interstellar medium. The rotation depends on the wavelength of the light, so for a pulsar, which emits light with the same polarization on different wavelengths, comparing the observed polarization at different wavelengths can give us information on the magnetic field along the line of sight. See for example [16] for more information.

11.2 The two-zone propagation model

For the propagation of charged cosmic rays, the magnetic field of the Galaxy is by far the most important factor. As mentioned above, the details of this field gives rise to a random walk behaviour for charged cosmic rays, and it is therefore common to describe the propagation in the Galaxy using diffusion models. We will mainly follow [19], and use the so-called two-zone propagation model for the Galaxy. The model in [19] is applied to antiprotons, but there is no phenomenological difference between the cases of antiprotons and antideuterons, and the model can be applied to antideuterons with only minor adjustments.

11.2.1 The model

The two-zone propagation model is a simple cylindrical diffusion model, and is, as the name suggests, divided into two zones: A thin gaseous disk and a magnetic halo. In this model, the disk and the halo have the same radius, $R = 20\,\mathrm{kpc}$. The half-height of the disk is usually chosen to be $h = 100\,\mathrm{pc}$, while the half-height, L, of the magnetic halo is a free parameter (see table 11.1).

Only dark matter annihilations taking place within the cylinder(s) are considered in this model, and it is assumed that the number density of antideuterons goes to zero at $z = \pm L$ and $r = R$. The dark matter halo is described by one of the density profiles from section 1.2, and goes beyond the cylinder of this model. A portion of the flux, corresponding to annihilations outside the cylinder, is thereby lost. A three-zone diffusion model, taking the extended size of the dark matter halo into account, was investigated in [43]. It was, however, found that the correction from including this region is smaller than the uncertainty related to the parameters describing the two-zone model.

We will consider 3 sets of parameters for the diffusion model, labeled 'max', 'min', and 'med'. The parameters in these sets are explained at different points in this section, and values are listed in table 11.1. The sets of parameters can be found by comparing the cosmic ray Boron/Carbon ratios from diffusion simulations with different parameters to observational results [14]. While all the sets are compatible with observed B/C ratios, the 'max' and 'min' models are physically extreme, and are not likely to correspond to the actual conditions in the Galaxy. They can, however, be considered upper and lower limits.

As mentioned in the discussion on the Galactic disk, there is a galactic wind flowing outwards from the disk. This outflow of diffusive material leads to convection, and we refer to it as a convective wind. In this model, it is common to use a constant convective wind, V_c, which is perpendicular to the Galactic disk, and is effective in the entire cylinder. V_c is another free parameter, whose value can be found in table 11.1.

Energy redistribution effects, such as reacceleration and energy losses due to interactions with interstellar matter will be neglected in this calculation. This approx-

Model	L in kpc	δ	K_0 in $\mathrm{kpc^2\,Myr^{-1}}$	V_c in $\mathrm{km\,s^{-1}}$
max	15	0.46	0.0765	5
med	4	0.7	0.0112	12
min	1	0.85	0.0016	13.5

Table 11.1: Propagation parameters for the max, med and min models. Data extracted from [14].

imation is commonly made in these kind of calculations, as the processes in question mainly take place in the rather thin Galactic disk. Since the dark matter annihilations take place in the vast dark matter halo, the antideuterons will generally spend very little time in the disk [14].

There is, however, one kind of process in the disk that should be considered, namely annihilations on interstellar matter. Annihilations will remove particles from the flux, rather than simply redistributing their energies, and can therefore have a much more profound effect on a possible dark matter annihilation signal.

11.2.2 The diffusion equation

Assuming steady state conditions (no time dependence in the antideuteron flux), the diffusion equation describing this model is given by

$$\underbrace{-K(T)\nabla^2 f}_{\text{(Spatial) diffusion}} + \underbrace{\frac{\partial}{\partial z}(\,\mathrm{sign}(z) f V_c)}_{\text{Convection}} = \underbrace{Q}_{\text{Source}} - \underbrace{2h\delta(z)\Gamma_{\,\mathrm{ann}}(T) f}_{\text{Annihilation}}, \tag{11.1}$$

where $f(\vec{x}, T) = dN_{\bar{d}}/dT$ is the number density of antideuterons per unit (kinetic) energy, $K(T)$ is the diffusion coefficient, and $\Gamma_{\,\mathrm{ann}}(T)$ describes annihilation of the antideuterons on interstellar matter.

The diffusion coefficient is related to the power spectrum of the inhomogeneities in the Galactic magnetic field. The reason for this is related to the energy dependence of the deflection of charged particles in magnetic fields. High energy particles are less deflected by a magnetic field than lower energy particles, and have to move for larger distances in the field in order to obtain the same deflection. This implies that higher energy particles are more susceptible to larger (and less susceptible to lower) scale inhomogeneities in the field than lower energy particles. The power spectrum is, unfortunately, poorly known. The best we can do to find an expression for the diffusion coefficient, is therefore to find a suitable analytical model. Following [19], we choose the following expression for the diffusion coefficient:

$$K(T) = K_0 \beta \mathcal{R}^{\delta}. \tag{11.2}$$

K_0 and δ are free parameters, and can be found from B/C ratio studies, as mentioned earlier. Values are found in table 11.1. β is the antideuteron velocity in units of c,

while the quantity $\mathcal{R}$ is called the rigidity, and is defined as

$$\mathcal{R} \equiv \frac{pc}{Ze} \cdot (\,\mathrm{GV})^{-1} \underset{Z=1}{=} \left(\frac{pc}{\mathrm{GeV}}\right), \tag{11.3}$$

where p is the antiproton momentum, e is the elementary charge, and $Z = 1$ is the atomic number of (anti)deuterons. For antideuterons, the rigidity is (in natural units) just the momentum in units of GeV.

Antideuterons can annihilate on interstellar matter in the Galactic disk. In this model, it is assumed that the interstellar matter in question is hydrogen and helium. The annihilation term, $\Gamma_{\,\mathrm{ann}}(T)$, in equation (11.1) is then defined as

$$\Gamma_{ann}(T) = (n_{\,\mathrm{H}} + 4^{\frac{2}{3}} n_{\,\mathrm{He}}) v\, \sigma_{\bar{d}p}^{\mathrm{ann}}(T). \tag{11.4}$$

$n_{\,\mathrm{H}}$ and $n_{\,\mathrm{He}}$ are here the number densities of hydrogen and helium in the disk, and we adopt the values of $n_{\,\mathrm{H}} \approx 1\,\mathrm{cm}^{-3}$ and $n_{\,\mathrm{He}} \approx 0.07 n_{\,\mathrm{H}}$ from [19]. The factor $4^{\frac{2}{3}}$ corrects for different cross sections for H and He interactions. v is the velocity of the antideuteron, while $\sigma_{\bar{d}p}^{\mathrm{ann}}(T)$ is the cross section of a $\bar{d}p$-collision where the antideuteron is destroyed. This is an inelastic interaction, and for finding the cross section, $\sigma_{\bar{d}p}^{\mathrm{ann}}$, we will follow [14].

We begin by expressing this cross section as

$$\sigma_{\bar{d}p}^{\mathrm{ann}} \equiv \sigma_{\mathrm{inel}}^{\mathrm{ann}} = \sigma_{\,\mathrm{inel}} - \sigma_{\mathrm{inel}}^{\mathrm{non-ann}} = \sigma_{\,\mathrm{tot}} - \sigma_{\,\mathrm{el}} - \sigma_{\mathrm{inel}}^{\mathrm{non-ann}}. \tag{11.5}$$

All these cross sections are, of course for a $\bar{d}p$ interaction. Experimental data for the total cross section, $\sigma_{\,\mathrm{tot}}$, is not available for this reaction, so we use data for the charge conjugate reaction, $\bar{p}d$, thus assuming

$$\sigma_{\,\mathrm{tot}}^{\bar{d}p} \approx \sigma_{\,\mathrm{tot}}^{\bar{p}d}. \tag{11.6}$$

For the elastic cross section, $\sigma_{\,\mathrm{el}}$, we have no experimental data for neither the reaction nor its charge conjugate. This is also the case for the total cross section data at high energies. For the elastic cross section, as well as the total cross section above $10^3\,\mathrm{GeV}$, we must therefore make the assumption

$$\sigma_{\,\mathrm{el}}^{\bar{d}p} \approx 2\sigma_{\,\mathrm{el}}^{\bar{p}p}. \tag{11.7}$$

The term $\sigma_{\mathrm{inel}}^{\mathrm{non-ann}}$ corresponds to an inelastic interaction where the antideuteron survives. Again, no data is available, and we approximate it by using the charge conjugate reaction, summing up the available $\bar{p}d \to Xd$ cross sections, which are basically $\bar{p}d \to (N\pi)\bar{p}d$, where N indicates the number of pions.

The total and elastic cross section data for $\bar{p}d$ and $\bar{p}p$ can be obtained from the Particle Data Group [7], while the data for $\bar{p}d \to (N\pi)\bar{p}d$ can be obtained from [50]. These data are plotted in figure 11.2. We note that very little data is available for the non-annihilating inelastic cross section, and our fit to these data is somewhat different to that in [14]. However, since this cross section is so small compared to the two others, the uncertainty in this cross section is of little importance.

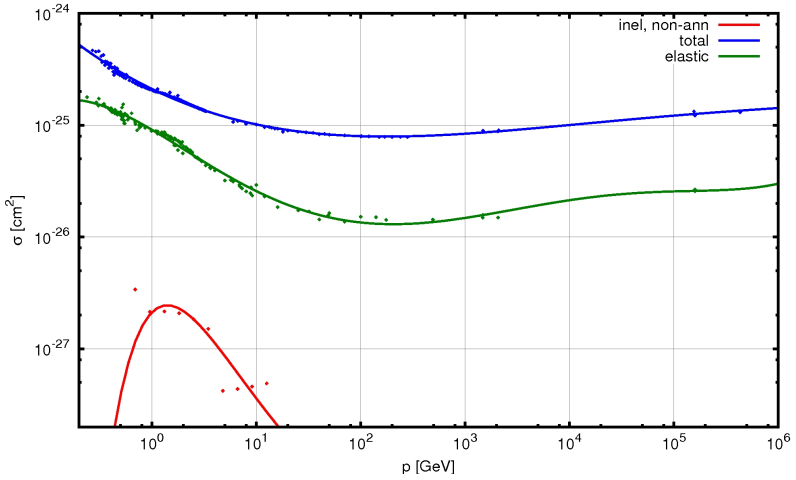

Figure 11.2: Cross section data for antideuterons on interstellar protons as a function of the antideuteron momentum. The points indicate experimental data, while the lines show the fits to the data which were used in our calculations.

11.2.3 The flux near Earth

The diffusion equation, (11.1), (with the boundary condition of zero antideuteron density at $z = L$ and $r = R$) can be solved analytically (see for example [23] or [39]), leading to an expression for the total flux, $\Phi_{\bar{d}}$, at the position of the Earth:

$$\frac{d\Phi_{\bar{d}}}{dT}(T, \vec{r}_{\odot}) = B \frac{v_{\bar{d}}}{4\pi} \left(\frac{\rho_{\odot}}{M_{DM}} \right)^2 R(T) \sum_k \frac{1}{2} \langle \sigma v \rangle_k \left(\frac{dN_{\bar{d}}}{dT} \right)_k . \tag{11.8}$$

Here, B is the boost factor discussed in section 6.2.1, which is needed if one wants to reproduce the PAMELA positron excess. $v_{\bar{d}}$ is the antideuteron velocity, $\rho_{\odot}$ is the dark matter density at the position of the Earth, M_{DM} is the dark matter particle mass, $\langle \sigma v \rangle_k$ is the annihilation cross section for process k ($k = \mathrm{W^+W^-}$, $\mathrm{b\bar{b}}$ etc.), and $(dN_{\bar{d}}/dT)_k$ is the corresponding antideuteron source spectrum. For our case, we will not sum over the different annihilation channels within the calculation, but rather calculate the contribution to the final flux from each channel separately.

The astrophysical data is encoded in the function $R(T)$, which does not depend on the source spectra or the dark matter mass. We therefore only need to calculate the function $R(T)$ once for different propagation parameters and dark matter distributions. $R(T)$ is a somewhat nasty function, and is given by

$$R(T) = \sum_{n=1}^{\infty} J_0 \left(\zeta_n \frac{r_{\odot}}{R} \right) \exp \left[-\frac{V_c L}{2K} \right] \frac{y_n(L)}{A_n \sinh(S_n L/2)}, \tag{11.9}$$

where $J_0(x)$ is the cylindrical Bessel function of 0th order, and ζ_n is the nth zero of this function. $r_{\odot}$ is the radial distance of the Earth from the Galactic center, and

R is the radius of the Galaxy in our model. Note that we drop the dependencies of some of the variables from our notation (e.g. we write K rather than $K(T)$). $y(Z)$, A_n, and S_n are all functions, and are defined by

$$y_n(Z) = \frac{4}{J_1^2(\zeta_n)R^2}\int_0^R dr\; rJ_0(\zeta_n r/R)\int_0^Z dz \exp\left[\frac{V_c(Z-z)}{2K}\right]\sinh(S_n(Z-z)/2)\left(\frac{\rho(r,z)}{\rho_\odot}\right)^2, \tag{11.10}$$

$$A_n = 2h\Gamma_{\text{ann}} + V_c + KS_n\coth(S_nL/2), \tag{11.11}$$

and

$$S_n = \sqrt{\frac{V_c^2}{K^2} + 4\frac{\zeta_n^2}{R^2}}. \tag{11.12}$$

$J_1(x)$ is here the cylindrical Bessel function of 1st order. The other variables have already been introduced earlier in the discussion. We note that the notation $\rho(r,z)$ corresponds to $\rho(r')$ with $r' = \sqrt{r^2+z^2}$. Numerical results for $R(T)$ are presented in section 11.2.4.

After calculating $R(T)$, we can find the flux at the position of the Earth using equation (11.8). There is, however, a local effect that is not accounted for in this equation, namely Solar modulation: The Sun emits a stream of charged particles through the Solar System, called the Solar wind. This solar wind contributes to decrease the kinetic energy of charged cosmic rays, making up the effect referred to as solar modulation. Without going into further detail, we follow [19], and adopt the following simple approximation to account for the solar modulation effect:

$$\frac{d\Phi_{\text{Earth}}}{dT_{\text{Earth}}} = \frac{p_{\text{Earth}}^2}{p^2}\frac{d\Phi}{dT}, \tag{11.13}$$

where the variables labeled 'Earth' are after Solar modulation, and the unlabeled ones are the variables before Solar modulation. The momentum p_{Earth} is given by

$$p_{\text{Earth}}^2 = 2m_{\bar{d}}T_{\text{Earth}} + T_{\text{Earth}}^2, \tag{11.14}$$

where

$$T_{\text{Earth}} = T - |Ze|\phi_{\text{Fisk}}. \tag{11.15}$$

ϕ_{Fisk} is here some effective potential called the Fisk potential. This potential characterizes the energy loss due to the Solar wind, and varies with the cyclic Solar activity. We here adopt the value of $\phi_{\text{Fisk}} = 0.5\,\text{GV}$ from [19].

11.2.4 Numerical results for R(T)

We calculated the astrophysical function $R(T)$ numerically for different dark matter distributions in all the three sets of propagation parameters. For calculating terms related to Bessel functions, we used the GSL library [1], and for integration we used an unnamed open integration formula of order $1/N^4$ (eq. 4.1.18 in Numerical Recipes [45]). We used 300 integration steps for the z integral, and 500 for the r integral.

Performing this computation was, however, not entirely straightforward. The reason for this is the convergence of the infinite sum in eq. (11.9). How fast the sum converges depends on the antideuteron energy, the set of propagation parameters, and the dark matter density profile. For a given parameter set, the sum converges faster for higher energies. For a given energy, the sum converges far faster in the 'max' parameter set than it does with the 'med' and 'min' parameters[7]. A large number of summation steps is required in the 'min' model to achieve sufficient accuracy.

The problem here is that as the number of steps increases, so does the size of the (largest) Bessel function zeros ζ_n. S_n is a function of ζ_n, and is involved in several hyperbolic terms. When ζ_n becomes large, so does S_n, and at some point, the $\sinh(aS_n)$ terms become too large to be represented by a double precision variable. When this happens, the computation breaks down, and we end up with 'inf' or 'NaN' results. For the NFW profile with 'min' propagation parameters, this happens slightly above 4000 steps. For the other propagation sets, this happens after even fewer steps, but in these cases the sum converges much faster. What this basically means, is that there is an upper limit to the accuracy we can achieve. If the accuracy condition is too strong, the computation will break down.

Instead of using a fixed number of steps for this calculation, we used only the number of steps required to reach our accuracy condition. We used a two-part condition:

- We require the fractional change in the sum, $\left|\frac{\sum_n - \sum_{n-1}}{\sum_n}\right|$, to have been less than 1% for the last 10 steps.
- A negative sum is unphysical, but when $R(T)$ is small, the sum may take on negative values before having converged sufficiently. In order to avoid negative values, we require the 50 last steps in the sum to have been positive. 50 is perhaps unnecessarily strict for this purpose, but it also serves as a minimum number of summation steps.

These conditions may not sound very strict, but for the lowest energies with the NFW or Einasto density profiles and the 'min' model, the conditions are only fulfilled after some 3800 steps (while the computation breaks down slightly above 4000). Any stricter conditions would not be possible to fulfill before the computation breaks down.

[7]The convergence rate goes down with max→med→min.

The results from the calculations are plotted in figure 11.3. We see that there is a significant difference between the different sets of propagation parameters, implying a significant uncertainty in the observable flux on Earth. There is also some difference between the different the density profiles, but this is far less significant. Note that the discrepancy between the dark matter profiles for low T in the 'min' model likely is due to insufficient convergence of the sums, rather than a physical difference.

This calculation was also performed by Kadastik et. al [32], and their result is shown in figure 11.4. We see that our result agrees very well with theirs, but note that the labels for the Einasto and Moore profiles appear to have been exchanged in their figure. We performed the calculation for the Moore profile in the 'max' and 'med' propagation models to confirm this, and the result agreed with the graph labeled 'Einasto' in their figure. The figure of Kadastik et. al shows no difference between the dark matter profiles for low energies in the 'min' model, something which supports our suspicion that the variation for these energies in our results is due to insufficient convergence of the sums.

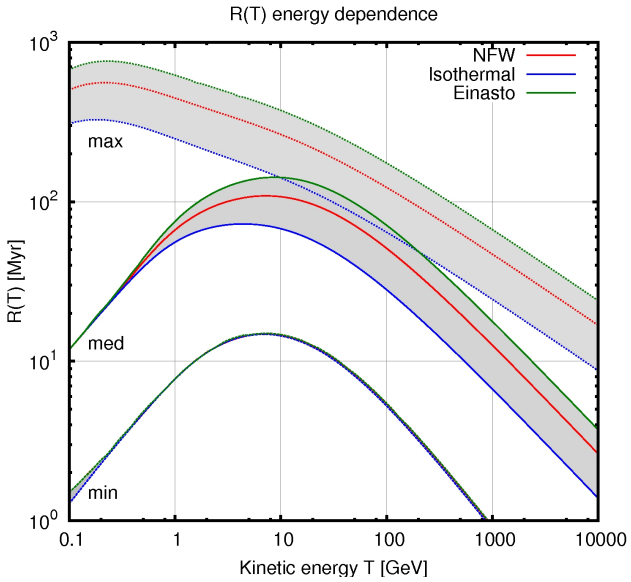

Figure 11.3: The function $R(T)$, plotted for different dark matter profiles and propagation settings. The filled grey areas show the differences in $R(T)$ between the density profiles for a given propagation model. The upper lines correspond to the 'max' model, the middle lines correspond to the 'med' model, and the lower lines correspond to the 'min' model.

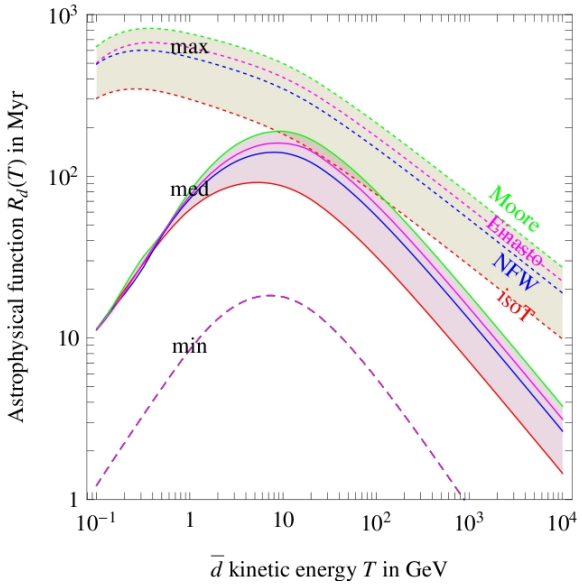

Figure 11.4: The function $R(T)$ for different dark matter profiles and propagation settings, as calculated by Kadastik et. al [32].

12 The final antideuteron spectra

With the source spectra and propagation model in place, we can finally calculate the resulting antideuteron flux near Earth. In order to compare our results to those of Kadastik et. al [32], we adopt their value for the thermally averaged cross section $\langle \sigma v \rangle = 3 \times 10^{-26}\,\mathrm{cm}^3/\mathrm{s}$ for all annihilation channels. This is the expected total annihilation cross section predicted by cosmology, and the result for each annihilation channel will thus correspond to a situation where the branching ratio of the given channel is 100%. In order to obtain the true antideuteron flux from annihilations of a given dark matter candidate, the results from the different annihilation channels should be weighted according to the corresponding branching ratios. This will, however, not be done in this thesis.

For comparison with the results of Kadastik et. al, we calculate results using the NFW density profile and the 'med' propagation setting. The 'med' propagation setting is physically the most realistic of the three, and as we saw in figure 11.3, the difference between different density profiles is comparatively small. As discussed in section 6.2.1, a boost factor, B, is required in equation (11.8) in order to explain the PAMELA excess through WIMP annihilations. In our calculations, this factor was set to 1. If enhancement mechanisms such as clumping of dark matter or Sommerfeld enhancement are in effect, the correct final spectra can be found by multiplying our results with the correct boost factor.

The results from our calculations are plotted in figure 12.1, while the corresponding results by Kadastik et. al are plotted in figure 12.2. Our plots are cut for high energies in the 100 GeV graphs, and for low energies in the 1 TeV W^+W^- case due to insufficient data in these energy ranges. Analyzing the graphs, we see that there is a significant enhancement in the peaks of the spectra when going from the isotropic to the more correct Monte Carlo approach. This enhancement is most significant for the 1 TeV W^+W^- case, where the new peak is 2 magnitudes higher than it was in the isotropic approach. In figure 12.3, we show the antideuteron fluxes from the Monte Carlo approach using the best and worst case scenario propagation settings. From the figure, we see that the uncertainty in the propagation model leads to an uncertainty in the final antideuteron spectrum of ~ 1.5 orders of magnitude.

Comparing our result to that of Kadastik et. al, we find that that our overall results agree fairly well. Again we note that the plot of Kadastik et. al shows the result for annihilation into light quarks rather than $b\bar{b}$. The spectra from these two cases should be similar, but not necessarily identical. We see that there are no order-of-magnitude differences between our results, but that there is some discrepancy in the shapes of the graphs; especially for the 1 TeV case. As before, there is a factor ~ 1.5 uncertainty in our plots for the Monte Carlo approach. The curves shown are 5th to 8th degree polynomials fitted to the data points, and some of the differences in the shapes of the curves are related to this curve fitting. Other sources of discrepancy

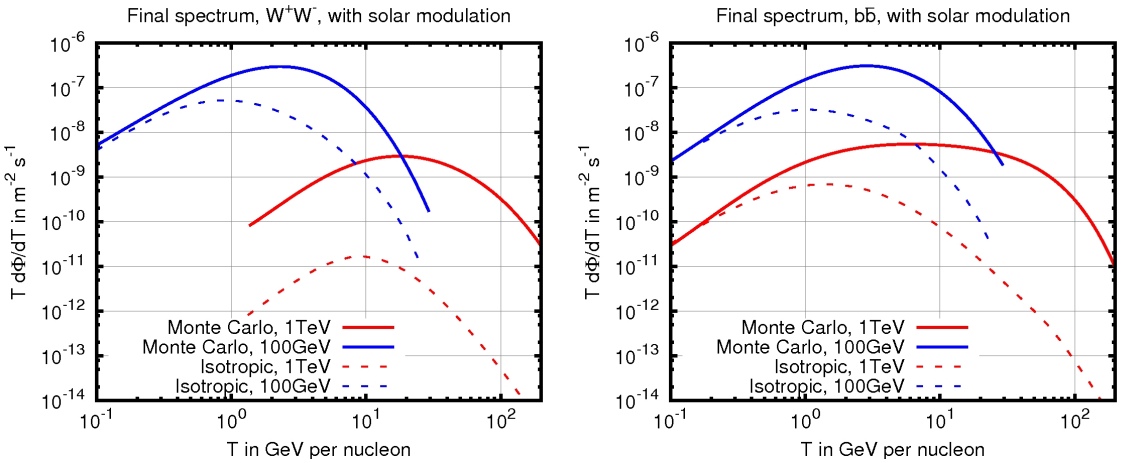

Figure 12.1: Final antideuteron spectra near Earth after propagation and Solar modulation. Calculations are done for dark matter masses of 1 TeV and 100 GeV, using the NFW density profile and the 'med' propagation parameters. In both plots, we assumed a thermally averaged cross section of $\langle \sigma v \rangle = 3 \times 10^{-26}\,\mathrm{cm}^3/\mathrm{s}$. Continuous lines show the result for the Monte Carlo approach, while dashed lines show the result from the isotropic approach.

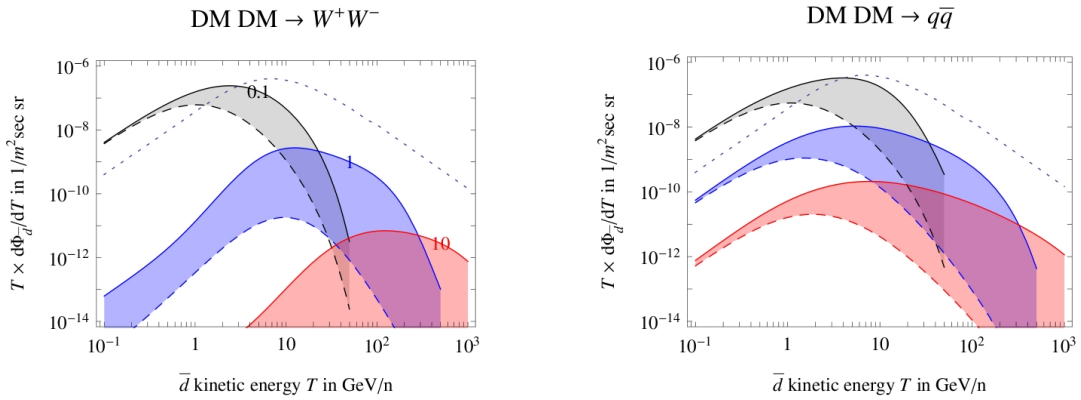

Figure 12.2: Final antideuteron spectra near Earth, as calculated by Kadastik et. al [32]. The plots show results calculated using the NFW profile, 'med' propagation settings, and thermally averaged cross sections of $\langle \sigma v \rangle = 3 \times 10^{-26}\,\mathrm{cm}^3/\mathrm{s}$. The results are plotted for $M_{DM} = \{0.1, 1, 10\}$ TeV in the corresponding colors grey, blue and red. Continuous lines show the Monte Carlo results, while dashed lines show the isotropic results. The black dotted lines show the expected astrophysical background.

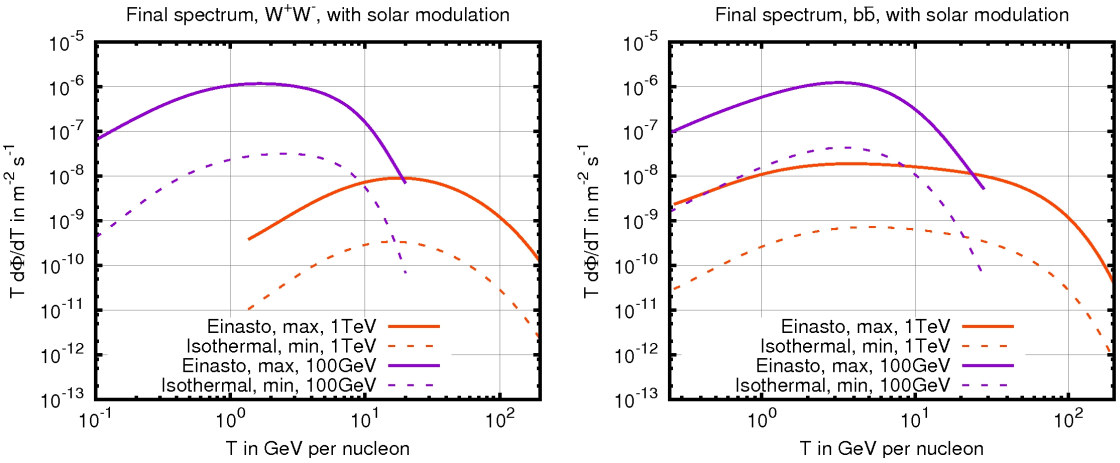

Figure 12.3: Final antideuteron spectra near Earth after propagation and Solar modulation for different propagation settings. Calculations are done for dark matter masses of 1 TeV and 100 GeV for the density profiles and propagation parameters that produce the highest and lowest fluxes (solid and dashed lines, respectively). All calculations were made using the Monte Carlo approach. In both plots, we assumed a thermally averaged cross section of $\langle \sigma v \rangle = 3 \times 10^{-26}\,\mathrm{cm}^3/\mathrm{s}$.

are, as discussed in section 9, differences between the Monte Carlo generators, as well as the use of different p_0 values.

The black dotted line in the plots by Kadastik et. al shows the expected astrophysical background from the secondary production mechanisms discussed in section 6.2.3. We see that without the presence of a boost factor, there is only hope of detecting light WIMPs through indirect detection in the antideuteron channel. For higher dark matter masses, the antideuteron spectra become orders of magnitude smaller than the expected background flux, and thus hard or impossible to detect. For the case of a dark matter with a mass of 1 TeV, we would have to rely on a boost factor $B \sim 50$ in order to be able to detect an annihilation signal in the antideuteron channel. As we can see from the plot by Kadastik et. al, even higher boost factors will be necessary for higher dark matter masses. Whether or not such a large factor is realistic is not a subject that will be discussed in this thesis.

We note that if such a boost factor should be present, a heavy WIMP candidate could produce an excess in the high energy range of the antiproton spectrum. In the isotropic coalescence approach, this does not appear to be the case, as the antideuteron spectrum drops off quickly for high kinetic energies. With the Monte Carlo approach, however, we see that the antideuteron spectrum does not drop off as quickly, and with a sufficient boost factor, a signal could be detectable at high kinetic energies.

Chapter III

Summary and conclusions

13 Summary

In this thesis, we have studied the expected antideuteron spectrum from annihilations of WIMP dark matter. We have presented some of the evidence for dark matter in galaxies and clusters of galaxies, and seen how modern cosmological models depict a universe consisting of 73% dark energy, 23% dark matter, and only 4% ordinary baryonic matter. We have also shown how calculations on freezeout of dark matter automaticly suggest WIMPs as dark matter candidates. We have briefly presented some of the proposed dark matter candidates, and we have discussed the means of direct and indirect WIMP detection.

The abundance of antimatter in the Universe today is extremely low, and since WIMPs should annihilate into equal parts matter and antimatter, antimatter cosmic ray channels may therefore offer the best prospects of observing a signal from WIMP annihilations. A significant excess above the expected astrophysical background has been found in the positron channel, while the measured spectrum of antiprotons can be explained entirely by known astrophysical sources. The excess in the positron channel is much larger than the signal one would expect from WIMP annihilations, and physical effects leading to a boost factor for the annihilation cross section would be required to explain the excess in terms of dark matter annihilations. The results from these two channels can be interpreted in several ways, and other channels are being investigated, in hope of being able to distinguish between the options.

The antideuteron channel is the most promising of the other antiparticle channels, and aside from upper limits on the flux, no observational data currently exist for this channel. Upcoming experiments such as GAPS and AMS-02 are expected to provide such data, and there is much activity in producing the expected antideuteron fluxes from various dark matter models before the data come in.

To describe the production mechanism of antideuterons, it is common to use the coalescence model. The coalescence model is based on the simple principle that

any (anti)nucleons with a momentum difference less than a threshold value, p_0, in their center-of-momentum frame will coalesce to produce a(n) (anti)nucleus. This prescription can be applied directly within a Monte Carlo simulation, but since the model was developed before the onset of Monte Carlo simulations, an approximate model was developed which applies the prescription to nucleon energy spectra. We went through one of the many possible derivations of the energy spectrum version of the model, and showed how an assumption of uncorrelated and isotropic (anti)nucleon momenta was required in this derivation.

For our calculations, we used the lightest MSSM neutralino as WIMP candidate, and theoretical motivations, as well as practical considerations around this choice have been discussed. With our WIMP candidate in place, we calculated the antideuteron source spectra from quark and gauge boson annihilation channels using both of the coalescence implementations. The primary goal of this thesis was to investigate if the large difference in magnitude of the antideuteron spectra from quark and gauge boson annihilation channels found by Bräuninger et. al in [14] was related to the approximations in the energy spectrum application of the coalescence model. Our calculations using the energy spectrum approach produced a similar difference between the two channels, while only a small difference in magnitude was found using the direct implementation of the model.

Investigating these results, we found the differences between the two models to depend on the dark matter mass, and that the gauge boson channel has a radically different behaviour in the energy spectrum approach. We found that main reason for the special behaviour of the gauge bosons is related to that the Monte Carlo generator treats quarks as virtual particles, while the gauge bosons are (incorrectly) being treated as on-shell particles. An overall difference in the number of antideuterons produced between the two versions of the coalescence model is related to the assumption of isotropy. The final state particles from dark matter annihilations come out in confined jets, and the probability of finding an antiproton-antineutron pair that satisfies the coalescence condition is therefore higher than if the momenta were isotropically distributed. In the gauge boson case, the jet confinement is stronger due to relativistic effects, but this does not affect coalescence, as the coalescence prescription is applied in the center-of-momentum frame of the particles.

During course of this work, the difference between the two implementations of the coalescence model was independently discovered by Kadastik et. al [32]. Their results appear to be in general agreement with ours, with exception of minor differences in the spectra, which are likely related to the use of different Monte Carlo generators and differences in the calibration. Since the primary goal of this thesis was investigated by Kadastik et. al, we decided to also consider the contributions from higher order annihilation processes. Our calculations showed that for the lightest MSSM neutralino, higher order processes will likely become important for neutralino masses in the TeV range. For the 100 GeV range, which we considered, corrections from higher order

processes can be neglected. These results depend heavily on the model used to introduce the WIMP candidate, but similar results can be expected for different mass ranges in other theories as well.

We finally investigated the commonly used two-zone propagation model for propagation of antideuterons in the Galaxy. Using this model, we calculated the expected observable antideuteron spectra near Earth from the different annihilation channels. We found our results to be in fair agreement with those calculated of Kadastik et. al. From these results, we found that using the direct implementation of the coalescence model leads to an order of magnitude enhancement of the antideuteron spectrum compared to the energy spectrum approach. Even so, only WIMPs with masses in the low 100 GeV range are likely to produce antideuteron fluxes higher than the expected astrophysical background without the presence of a boost factor.

14 Conclusions and future outlook

The primary goal of this thesis was to investigate the difference in the magnitude of the antideuteron spectra between the quark and gauge boson channels found by Bräuninger et. al [14]. In our analysis of the source spectra in section 9.2, we found that this difference mainly is due to the gauge bosons incorrectly being treated as on-shell particles by the Monte Carlo generators[1]. Being treated as on-shell, the gauge bosons decay to produce the same number of final state particles for all dark matter masses. The quarks, on the other hand, are being treated as virtual particles, and decay into a higher number of final state particles with increasing dark matter masses. Equation (9.1), which governs coalescence with energy spectra, contains a factor $1/M_{\mathrm{DM}}^2$. Since the gauge bosons incorrectly produce a constant average number of final state particles, the number of antideuterons produced is accordingly suppressed as $1/M_{\mathrm{DM}}^2$. In the quark case, the number of final state particles increases with increasing dark matter masses, something which to some degree compensates for the $1/M_{\mathrm{DM}}^2$ suppression.

From our studies, we have, in other words, found that difference between the quark and gauge boson cases in the article by Bräuninger et. al was not mainly due to the assumption of uncorrelated and isotropic nucleon momenta, but rather due to how the particles are treated by the Monte Carlo generators. The incorrect treatment of the gauge bosons does not only affect the isotropic coalescence approach. If the bosons had been treated as virtual particles, the number of available nucleons for coalescence would have increased for increasing dark matter masses. This would have affected the number of antideuterons produced in the direct coalescence approach as well. Not only that; the error in the number of final state particles produced affects the contribution from this annihilation channel to all other cosmic ray channels as

[1]Treating the gauge bosons as on-shell is, however, a good approximation at low energies.

well. Future studies of dark matter annihilations should therefore find a way for the Monte Carlo generators to correctly treat the gauge bosons as virtual particles.

While the difference between the antideuteron spectra from the different annihilation channels was not directly related to the isotropic assumption, we found that the assumption does have a profound effect on the shapes and overall magnitudes of the spectra. The final state particles from dark matter annihilations emerge in confined jets, rather than being isotropically distributed. This leads to a higher probability of finding an antiproton-antineutron pair that fulfills the coalescence condition of a momentum difference less than p_0. In the coalescence approach that applies to energy spectra, this jet effect is missed, and the produced antideuteron spectrum is consequently lower. The shapes of the spectra also differ between the two approaches. For the final antideuteron spectrum near the Earth, these differences lead to spectra that are about a magnitude lower in the isotropic approach for a dark matter mass of 1 TeV. From our results in figure 12.1, as well as those of Kadastik et. al in figure 12.2, we find that the difference in magnitude between the approaches does not seem to depend much on the dark matter mass. Instead, the antideuteron spectrum appears to broaden as the dark matter mass increases.

The direct implementation of the coalescence model is not much more cumbersome to implement than the energy spectrum approach, and since it yields more physically correct results, future studies of the antideuteron flux from dark matter annihilations should use the direct implementation rather than the traditional energy spectrum approach. For studies that fail to get the Monte Carlo to treat the gauge bosons correctly, using the direct implementation of the coalescence approach will, as we have seen, also have a dramatic effect on the antideuteron spectrum from gauge boson annihilation channels.

From the final antideuteron spectra near Earth, we found that even in the direct implementation, only WIMP candidates with masses in the low 100 GeV range will produce antideuteron fluxes that are higher than the expected astrophysical background without a significant boost factor. Such a boost factor has already been motivated by the large excess in the positron spectrum, and could arise from phenomena such as clumping of dark matter or Sommerfeld enhancement. We are not going to discuss any of these effects, nor are we going to investigate how large boost factors could be expected from these effects. If a large boost factor should be present, however, our results indicate that heavy dark matter particles could be detected through an excess in the high energy range of the antideuteron spectrum. Due to the quick falloff in the spectrum generated by the isotropic approach, such an excess is only predicted by the direct implementation of the coalescence model.

In addition to calculating the antideuteron spectra from tree level processes, we investigated how big the influence of higher order processes can be expected to be. These calculations depend heavily on the model used to introduce the WIMP candidate, and only apply directly to the MSSM. The contribution to the antideuteron spectrum

from the various annihilation channels depend on the branching ratios between the channels. Our calculations were not meant to give a full picture of all the annihilation channels, but rather give an indication on the influence of higher order processes. We therefore only calculated the branching ratios between the W^+W^- channel and the processes in which one and two extra Z-bosons are emitted. Our results showed that corrections from higher order processes are negligible for neutralino masses below 1 TeV, but that the higher order processes are likely to become important for masses in the multi-TeV range. The contribution from the two-Z-process increases faster with increasing neutralino mass than that from the one-Z-process. This indicates that for increasing neutralino masses, corrections from an increasing number of processes must be considered.

We only considered neutralino masses below 1 TeV, and did not have to take higher order processes into account. In studies where multi-TeV neutralinos are considered, however, corrections to the spectra from higher order processes should be taken into account. While our result only applies directly to the MSSM, similar results may be expected for different mass ranges in other models as well. For articles like those of Bräuninger et. al and Kadastik et. al, where dark matter masses up to tens of TeV are considered, corrections from higher order processes should definitely be investigated.

The reason why we could not consider neutralinos in the TeV range, is that the SUSY spectrum generators become too inaccurate for these masses. Studies considering high mass neutralinos should therefore either calculate the exact mass spectra and mixing matrices by hand, or develop improved spectrum generators, which can provide sufficient accuracy in this mass range.

The ultimate test of our results will be comparison against observational data. As mentioned earlier, no observational data is yet available for the antideuteron channel, but upcoming experiments such as GAPS and AMS-02 are expected to shed new light on the energy spectrum of the antideuteron channel. There is currently large activity in finding the expected antideuteron fluxes for different dark matter scenarios, but only when the observational results become available will we be able to distinguish between them.

Appendix

Special Relativity

Some equations from special relativity are needed in the derivation of the equations for the coalescence model. These equations are listed and explained here, but not derived.

We use the following definition of the Minkowski metric as our metric tensor:

$$\eta_{\mu\nu} = \begin{pmatrix} 1 & 0 & 0 & 0 \\ 0 & -1 & 0 & 0 \\ 0 & 0 & -1 & 0 \\ 0 & 0 & 0 & -1 \end{pmatrix}. \tag{A.1}$$

The inner product of two four-vectors, **a** and **b**, is thus given by

$$a^\mu b_\mu = \eta_{\mu\nu} a^\mu b^\nu = a^0 b^0 - a^1 b^1 - a^2 b^2 - a^3 b^3. \tag{A.2}$$

We note again are using natural units, $c = \hbar = k_B = 1$, and generally do not explicitly write these quantities in our equations. Factors of c are, in other words left out in many of the equations in this section.

Energies and momenta

The four-momentum of a particle of mass m is defined as

$$\mathbf{p} = (\frac{E}{c}, p_x, p_y, p_z), \tag{A.3}$$

where p_i is the momentum component in the i-direction, and

$$E = \sqrt{m^2 + \vec{p}^2}, \tag{A.4}$$

is the energy. The relativistic momentum, $p \equiv \|\vec{p}\|$, is given by

$$p = \gamma m v. \tag{A.5}$$

γ is the Lorentz factor, and is given by

$$\gamma = \frac{1}{\sqrt{1-\beta^2}}, \tag{A.6}$$

where $\beta = v/c$. The energy of a particle moving at a velocity v can also be expressed in terms of the Lorentz factor:

$$E = \gamma m. \tag{A.7}$$

The relativistic kinetic energy of a particle is defined as

$$T \equiv E - m. \tag{A.8}$$

Lorentz transformations

The Lorentz transformation from a frame S to frame S', which is moving with velocity $-v$ along the x-axis with respect to S, is governed by

$$\Lambda^{\mu}{}_{\nu} = \begin{pmatrix} \gamma & \beta\gamma & 0 & 0 \\ \beta\gamma & \gamma & 0 & 0 \\ 0 & 0 & 1 & 0 \\ 0 & 0 & 0 & 1 \end{pmatrix}. \tag{A.9}$$

Assume that a particle is moving along the x-axis with momentum p (corresponding to a four-momentum $\mathbf{p} = (E, p, 0, 0)$) in the S-frame. Applying (A.9) to (A.3) gives us the momentum p' in the frame S', which is moving at a velocity $-v$ along the x-axis:

$$p' \equiv p'^1 = \Lambda^1{}_{\nu} p^{\nu} = \frac{p + vE}{\sqrt{1-v^2}}. \tag{A.10}$$

$E' = \sqrt{m^2 + p'^2}$ is there the energy of the particle in the S'-frame.

Lorentz transformations can also be applied to velocities. We will not go through the calculation here, only list the result. Consider a particle that is moving in the xy-plane in frame S with velocity components v_x in the x-direction and v_y in the y-direction. The corresponding velocity components in frame S', which is moving with a velocity $-V$ along the x-axis with respect S, are given by

$$v'_x = \frac{v_x + V}{1 + V v_x} \tag{A.11}$$

$$v'_y = \frac{v_y}{\gamma(1 + V v_x)}. \tag{A.12}$$

Lorentz invariant quantities

Rather than Lorentz transforming quantities between frames, it is often more convenient to work with quantities that are the same in all frames, i.e. Lorentz invariant quantities. The four-momentum squared is one such quantity:

$$\mathbf{p}^2 \equiv p_\mu p^\mu = E^2 - \vec{p}^2 = E^2 - (E^2 - m^2) = m^2. \tag{A.13}$$

In two-body scattering events, it is common to introduce the Lorentz invariant quantities known as Mandelstam variables. Let $\mathbf{p_i}$ denote the 4-momentum of particle i, where particle 1 and 2 are the incoming particles, and 3 and 4 are the outgoing ones. The Mandelstam variables are then given by:

$$s = (\mathbf{p}_1 + \mathbf{p}_2)^2 = (\mathbf{p}_3 + \mathbf{p}_4)^2 \tag{A.14}$$

$$t = (\mathbf{p}_1 - \mathbf{p}_3)^2 = (\mathbf{p}_2 - \mathbf{p}_4)^2 \tag{A.15}$$

$$u = (\mathbf{p}_1 - \mathbf{p}_4)^2 = (\mathbf{p}_2 - \mathbf{p}_3)^2. \tag{A.16}$$

The Mandelstam variables are Lorentz scalars, and thus have the same value in any reference frame. This makes them a valuable tool for connecting quantities in different frames.

Bibliography

[1] GSL - GNU Scientific Library, http://www.gnu.org/software/gsl/.

[2] SUSY spectrum generators, http://kraml.web.cern.ch/kraml/comparison/.

[3] O. Adriani et al. An anomalous positron abundance in cosmic rays with energies 1.5-100 GeV. *Nature*, 458:607–609, 2009, arXiv:0810.4995.

[4] O. Adriani et al. PAMELA results on the cosmic-ray antiproton flux from 60 MeV to 180 GeV in kinetic energy. *Phys. Rev. Lett.*, 105:121101, 2010, arXiv:1007.0821.

[5] Z. Ahmed et al. Dark matter search results from the CDMS II experiment. *Science (New York, N.Y.)*, 327(5973):1619–21, Mar. 2010.

[6] I. Aitchison. *Supersymmetry in Particle Physics: An Elementary Introduction*. Cambridge University Press, 2007.

[7] C. Amsler et al. Review of particle physics. *Physics Letters B*, 667(1-5):1 – 6, 2008. Review of Particle Physics.

[8] S. Ando. Cosmic gamma-ray background from dark matter annihilation. *Journal of Physics Conference Series*, 60:247–250, Mar. 2007.

[9] E. Armengaud. Gif Lectures on direct detection of Dark Matter. 2010, arXiv:1003.2380.

[10] L. Baudis. Direct Detection of Cold Dark Matter. 2007, arXiv:0711.3788.

[11] C. L. Bennett et al. First Year Wilkinson Microwave Anisotropy Probe (WMAP) Observations: Preliminary Maps and Basic Results. *Astrophys. J. Suppl.*, 148:1, 2003, arXiv:astro-ph/0302207.

[12] L. Bergstrom, J. Edsjo, and P. Ullio. Cosmic antiprotons as a probe for supersymmetric dark matter? *Astrophys. J.*, 526:215–235, 1999, arXiv:astro-ph/9902012.

[13] G. Bertone, D. Hooper, and J. Silk. Particle dark matter: Evidence, candidates and constraints. *Phys. Rept.*, 405:279–390, 2005, arXiv:hep-ph/0404175.

[14] C. B. Brauninger and M. Cirelli. Anti-deuterons from heavy Dark Matter. *Phys. Lett.*, B678:20–31, 2009, arXiv:0904.1165.

[15] T. Bringmann and P. Salati. Galactic antiproton spectrum at high energies: Background expectation versus exotic contributions. *Phys. Rev. D*, 75(8):083006, Apr 2007.

[16] B. F. Burke and S. F. Graham-Smith. *An introduction to radio astronomy.* Cambridge University Press, 2010.

[17] B. W. Carroll and D. A. Ostlie. *An Introduction to Modern Astrophysics: International Edition.* Pearson Education, 2006.

[18] P. Chardonnet, J. Orloff, and P. Salati. The production of anti-matter in our galaxy. *Phys. Lett.*, B409:313–320, 1997, arXiv:astro-ph/9705110.

[19] M. Cirelli, R. Franceschini, and A. Strumia. Minimal Dark Matter predictions for galactic positrons, anti-protons, photons. *Nucl. Phys.*, B800:204–220, 2008, arXiv:0802.3378.

[20] M. Cirelli, M. Kadastik, M. Raidal, and A. Strumia. Model-independent implications of the e+, e-, anti-proton cosmic ray spectra on properties of Dark Matter. *Nucl. Phys.*, B813:1–21, 2009, arXiv:0809.2409.

[21] A. Coc, E. Vangioni-Flam, P. Descouvemont, A. Adahchour, and C. Angulo. Updated Big Bang Nucleosynthesis confronted to WMAP observations and to the Abundance of Light Elements. *Astrophys. J.*, 600:544–552, 2004, arXiv:astro-ph/0309480.

[22] F. Donato, N. Fornengo, and D. Maurin. Antideuteron fluxes from dark matter annihilation in diffusion models. *Phys. Rev.*, D78:043506, 2008, arXiv:0803.2640.

[23] F. Donato, N. Fornengo, D. Maurin, and P. Salati. Antiprotons in cosmic rays from neutralino annihilation. *Phys. Rev.*, D69:063501, 2004, arXiv:astro-ph/0306207.

[24] F. Donato, N. Fornengo, and P. Salati. Antideuterons as a signature of supersymmetric dark matter. *Phys. Rev.*, D62:043003, 2000, arXiv:hep-ph/9904481.

[25] Y. N. Efremov. On the Spiral Structure of the Milky Way Galaxy. 2010, arXiv:1011.4576.

[26] H. Fuke et al. Search for Cosmic-Ray Antideuterons. *Phys. Rev. Lett.*, 95:081101, 2005, arXiv:astro-ph/0504361.

[27] G. Gelmini and P. Gondolo. DM production mechanisms. 2010, arXiv:1009.3690.

[28] J. B. Hartle. *Gravity: An Introduction to Einstein's General Relativity.* Addison Wesley, 2002.

[29] D. Hooper. Indirect Searches For Dark Matter: Signals, Hints and Otherwise. 2007, arXiv:0710.2062.

[30] N. Jarosik et al. Seven-Year Wilkinson Microwave Anisotropy Probe (WMAP) Observations: Sky Maps, Systematic Errors, and Basic Results. *Astrophys. J. Suppl.*, 192:14, 2011, arXiv:1001.4744.

[31] G. Jungman, M. Kamionkowski, and K. Griest. Supersymmetric dark matter. *Phys. Rept.*, 267:195–373, 1996, arXiv:hep-ph/9506380.

[32] M. Kadastik, M. Raidal, and A. Strumia. Enhanced anti-deuteron Dark Matter signal and the implications of PAMELA. *Phys. Lett.*, B683:248–254, 2010, arXiv:0908.1578.

[33] G. Kane, R. Lu, and S. Watson. PAMELA Satellite Data as a Signal of Non-Thermal Wino LSP Dark Matter. *Phys. Lett.*, B681:151–160, 2009, arXiv:0906.4765.

[34] A. Klypin, H. Zhao, and R. S. Somerville. LCDM-based models for the Milky Way and M31 I: Dynamical Models. *Astrophys. J.*, 573:597–613, 2002, arXiv:astro-ph/0110390.

[35] J. M. Kubo et al. The Mass Of The Coma Cluster From Weak Lensing In The Sloan Digital Sky Survey. *Astrophys. J.*, 671:1466–1470, 2007, arXiv:0709.0506.

[36] M. L. Kutner. *Astronomy: A Physical Perspective.* Cambridge University Press, 2003.

[37] J. Liu, P.-f. Yin, and S.-h. Zhu. Prospects for Detecting Neutrino Signals from Annihilating/Decaying Dark Matter to Account for the PAMELA and ATIC results. *Phys. Rev.*, D79:063522, 2009, arXiv:0812.0964.

[38] J. C. Mather, D. J. Fixsen, R. A. Shafer, C. Mosier, and D. T. Wilkinson. Calibrator Design for the COBE Far Infrared Absolute Spectrophotometer (FIRAS). *Astrophys. J.*, 512:511–520, 1999, arXiv:astro-ph/9810373.

[39] D. Maurin, F. Donato, R. Taillet, and P. Salati. Cosmic Rays below Z=30 in a diffusion model: new constraints on propagation parameters. *Astrophys. J.*, 555:585–596, 2001, arXiv:astro-ph/0101231.

[40] D. Maurin et al. Galactic cosmic ray nuclei as a tool for astroparticle physics. 2002, arXiv:astro-ph/0212111.

[41] D. Minniti and M. Zoccali. The Galactic Bulge: A Review. 2007, arXiv:0710.3104.

[42] J. F. Navarro, C. S. Frenk, and S. D. M. White. The Structure of Cold Dark Matter Halos. *Astrophys. J.*, 462:563–575, 1996, arXiv:astro-ph/9508025.

[43] M. Perelstein and B. Shakya. Antiprotons from Dark Matter: Effects of a Position-Dependent Diffusion Coefficient. 2010, arXiv:1012.3772.

[44] F. Petriello and K. M. Zurek. DAMA and WIMP dark matter. *JHEP*, 09:047, 2008, arXiv:0806.3989.

[45] W. H. Press, S. A. Teukolsky, W. T. Vetterling, and B. P. Flannery. *Numerical Recipes 3rd Edition: The Art of Scientific Computing*. Cambridge University Press, 2007.

[46] F. M. Rieger, V. Bosch-Ramon, and P. Duffy. Fermi acceleration in astrophysical jets. *Astrophys. Space Sci.*, 309:119–125, 2007, arXiv:astro-ph/0610141.

[47] B. Ryden. *Introduction to Cosmology*. Benjamin Cummings, 2002.

[48] S. Schael et al. Deuteron and anti-deuteron production in e+ e- collisions at the Z resonance. *Phys. Lett.*, B639:192–201, 2006, arXiv:hep-ex/0604023.

[49] P. Schneider, C. S. Kochanek, and J. Wambsganss. *Gravitational lensing: strong, weak and micro*. Springer, 2006.

[50] H. Schopper, editor. *Nuclei - Total Cross-Sections for Reactions of High Energy Particles - Subvolume B*, volume 12b of *Landolt-Börnstein - Group I Elementary Particles, Nuclei and Atoms*. Springer-Verlag, Berlin/Heidelberg, 1988.

[51] D. N. Spergel et al. Wilkinson Microwave Anisotropy Probe (WMAP) three year results: Implications for cosmology. *Astrophys. J. Suppl.*, 170:377, 2007, arXiv:astro-ph/0603449.

[52] M. Turner and E. Kolb. *The Early Universe (Frontiers in Physics)*. Addison Wesley, 1990.

[53] Q. Yuan, P.-F. Yin, X.-J. Bi, X.-M. Zhang, and S.-H. Zhu. Gamma rays and neutrinos from dark matter annihilation in galaxy clusters. *Phys. Rev.*, D82:023506, 2010, arXiv:1002.0197.